Department of Electrical and Computer Engineering

Extended Kalman Filters and Piece-wise Linear Segmentation for the Processing of Drilling Data

Amirali Soroush

This thesis is presented for the Degree of
Doctor of Philosophy
of
Curtin University

October 2012

Declaration

To the best of my knowledge and belief this thesis contains no material previously published by any other person except where due acknowledgment has been made.

This thesis contains no material which has been accepted for the award of any other degree or diploma in any university.

Signature: _____

Date: _____

Abstract

This research is oriented to the development and implementation of signal processing techniques for the analysis of drilling data with a focus on adaptive filters and segmentation schemes.

The thesis is divided into two distinct parts; the first part deals with the use of extended Kalman filters to estimate in, real-time, the instantaneous angular velocity of the drilling bit using downhole measurements. The method accounts for process and measurement noises as well as sensor bias error with the competitive ability to capture events of backward rotation particularly detrimental to the bit life. The model is validated against field data and the results are compared to estimate derived from magnetometer measurements.

The second part of this research is devoted to a novel method for the segmentation of piece-wise linear signals corrupted with noise. The research has led to the development of a novel technique for piece-wise linear segmentation, with a particular interest for noise (possibly non-stationary) contaminated piece-wise continuous signal. The method relies on the geometrical properties of the signal of residuals (difference between the original signal and the current fit). For this, a mechanical- mathematical tool dubbed "BBQ Tong" is introduced that is used to identify in the signal of residuals, the sharpest or most triangular peaks which correspond to the break-points in the original signal. This intuitive method proves to be quite efficient, the "BBQ Tong" operates as a transform operator acting as a low-pass filter with appropriate selection of the tool properties. A theoretical study of the tool supported by several examples is also presented. Numerical results are compared with other segmentation techniques available in the literature.

To my mother, for her endless love and support.

Acknowledgements

The process of preparing this dissertation could not have been accomplished without the ongoing support of many people. First, I would like to sincerely thank my supervisor, Professor Sven Nordholm form Curtin University for his contribution, expert guidance and support throughout my study.

I owe my deepest gratitude to my associate supervisor, Dr Thomas Richard from CSIRO Earth Science and Resource Engineering, who made me believe in myself and guided me through the whole process of my study and dissertation writing. I am sure that this research would not have been completed without his mentorship, support, understanding, and encouragement.

I would like to offer my special thank to Dr Vincent Denoël from University of Liège for his invaluable advice, inspiration, and support, during my three months stay in Belgium.

I wish to thank Epslog Engineering for their permission to use the concept of segmentation algorithm, "BBQ Tong" and also Diamant Drilling Services for arranging my visit of their facility in Charleroi, Belgium and providing the drilling data.

Finally I would like to acknowledge Curtin University and CSIRO Earth Science and Resource Engineering for providing my Postgraduate Research Scholarship (CIPRS).

Abbreviations

BHA	bottom hole assembly
BIC	Bayesian information criterion
BT	BBQ Tong
CDF	cumulative distribution function
CSP	candidate segmenting point
DP	dynamic programming
EKF	extended Kalman filters
FSW	feasible span window
PDF	probability density function
PMF	probability mass function
ROP	rate of penetration
RV	random variable
SNR	signal to noise ratio
SSE	sum of squared error
SW	sliding window
TOB	torque on bit
WOB	weight on bit

Symbols and Operators

$[\cdot]^T$	transpose of a matrix
$[\cdot]^{-1}$	inverse of a matrix
$[\cdot]^\dagger$	pseudoinverse of a matrix
$E[\cdot]$	expected value
$\mathbf{I}_N$	the $N \times N$ identity matrix
$\exp(\cdot)$	the exponential function
π	pi constant
$\partial(\cdot)$	partial derivative
$\Sigma(\cdot)$	summation operator
$\int(\cdot)$	integration operator
$\Pi(\cdot)$	multiplication operator
$f(\cdot)$	the probability density function
$F(\cdot)$	the cumulative distribution function
$\sim \mathcal{N}(0, \sigma^2)$	a normal distribution with zero mean and variance σ^2

Contents

List of Figures

List of Tables

Preamble

Introduction

The interpretation of drilling data has raised increasing attention in the drilling community due to the high costs of today's drilling operations such as deep extended reach or deep water wells. It is commonly recognized that robust interpretation methods are the cornerstones of efficient drilling optimization schemes. Along with the progress in instrumentation and automation on the rig floor, the fast rate development of downhole measurement while drilling emphasizes, however, the need for fast and efficient processing of large volume of data, a prerequisite to any interpretation methods.

The research presented in this thesis is oriented to the development and implementation of signal processing techniques for the analysis of drilling data with a focus on adaptive filters and segmentation schemes. The thesis is divided into two distinct parts; the first part deals with the use of extended Kalman filters to estimate in real-time, the instantaneous angular velocity of the drill bit using downhole measurements, while the second part is devoted to a novel method for the segmentation of piece-wise linear signals corrupted with noise.

Summary of Major Contribution

Part I

Because of the intrinsic properties of the drillstring (slenderness and resulting very high compliance) and intrinsic nature of the bit-rock interface (cutting, friction), the susceptibility of a drilling assembly to vibrations is very acute. They are prone to undergo self-excited axial, lateral and torsional vibrations whose worst extents (bouncing, whirl and stick-slip) can lead to dramatic equipment failures and/or drastic drop in

performance.

Over the past years, the drilling industry has made significant progress in introducing new instrumentation to record accelerations undergone by the drilling assembly downhole with high level of precision. But there is still a need for fast, robust and reliable interpretation algorithms to detect the occurrence and characterise the nature and severity of the vibrations.

This part of the research focuses on estimating the instantaneous angular velocity of the bit using accelerometer measurements and extended Kalman filters. The method accounts for process and measurement noises as well as sensor bias error with the competitive ability to capture events of backward rotation particularly detrimental to the bit life. The model is validated against field data and the results are compared to estimate derived from magnetometer measurements. Equations for the more general case of in plane kinematics accounting for lateral vibrations (or whirl) are also derived and the solutions for some particular cases discussed.

Part II

Segmentation methods play an important role in lowering the volume of data generated while drilling for data management purposes. But also, the underlying trend, or the homogeneous, stationary responses are quite often sought for their intrinsic simplicity specifically for parameters identification or model fitting.

The research has led to the development of a novel technique for piece-wise linear segmentation, with a particular interest for noise (possibly non-stationary) contaminated piece-wise continuous signal. The method relies on the geometrical properties of the signal of residuals (difference between the original signal and the current fit). The idea of splitting the signal at the point of maximum deviation is not novel, however, we consider here the maximum angular deviation from the overall fit or in other words, the sharpest peak in the signal of residuals. For this, we introduce a mechanical-mathematical tool dubbed "BBQ Tong" that is used to identify in the signal of residuals, the sharpest or most triangular peaks which correspond to the break-points in the original signal. This intuitive method proves to be quite efficient, the "BBQ Tong" operates as a transform operator acting as a low-pass filter with appropriate selection of the tool properties. A theoretical study of the tool supported by several examples is presented. Numerical results are compared with other techniques available in the

literature for segmentation.

List of Publications (2008-2012)

A. Soroush, T. Richard, and S. Nordholm, "Estimation of the drill bit angular velocity using accelerometer measurements and extended Kalman filters" in *7 th International Symposium on Image and Signal Processing and Analysis (ISPA 2011)*, (Dubrovnik, Croatia), pp. 6871, September 2011.

A.Soroush, V. Denoël, T. Richard, S. Nordholm, "Piecewise Linear Segmentation Using "BBQ Tong" Algorithm, Part I: Non-zero Stiffness" submitted to the international journal of *Information Sciences*.

A.Soroush, V. Denoël, T. Richard, S. Nordholm, "Piecewise Linear Segmentation Using "BBQ Tong" Algorithm, Part II: Zero Stiffness" to be submitted to the international journal of *Information Sciences*.

Part I

Determination of the In-plane Kinematics of a Rotating Shaft from Accelerometer Measurements

Chapter 1

Introduction

1.1 Background

Rotary drilling systems are commonly used in the drilling industry to create deep wells for the exploration of oil and gas. A schematic rotary drilling system with its components is illustrated in Fig. 1.1, the process of cutting the rock is performed by the drill bit that is connected to the surface through a chain of pipes called drillstring. The drillstring, up to several kilometres long, transmits the torque generated on surface to rotate the drill bit.

The lower part of the drillstring commonly referred to as the"Bottom Hole Assembly" (BHA) consists of up to several hundreds of meters of heavy-weight drill pipes or drill collars and is designed to provide enough axial force (weight on bit) to penetrate the rock formation. Other components such as stabilizers, reamers, hole-openers and measurement subs are also mounted within the BHA. Drilling rods or pipes come in length of about 30 m and an outer diameter of the order of 50 to 200 mm. Also, nowadays, numerous boreholes are drilled in complex 3D trajectories with tight geometrical constraints.

Because of the intrinsic properties of the drillstring (slenderness and resulting very high compliance) and the intrinsic nature of the bit-rock interface (cutting, friction), the susceptibility of a drilling assembly to vibrations is very acute. They are prone to undergo self-excited axial, lateral and torsional vibrations whose worst extents (bouncing, whirl and stick-slip) can lead to dramatic failures of drilling equipment and/or drastic drop in performance. Therefore, an extensive amount of research was dedicated

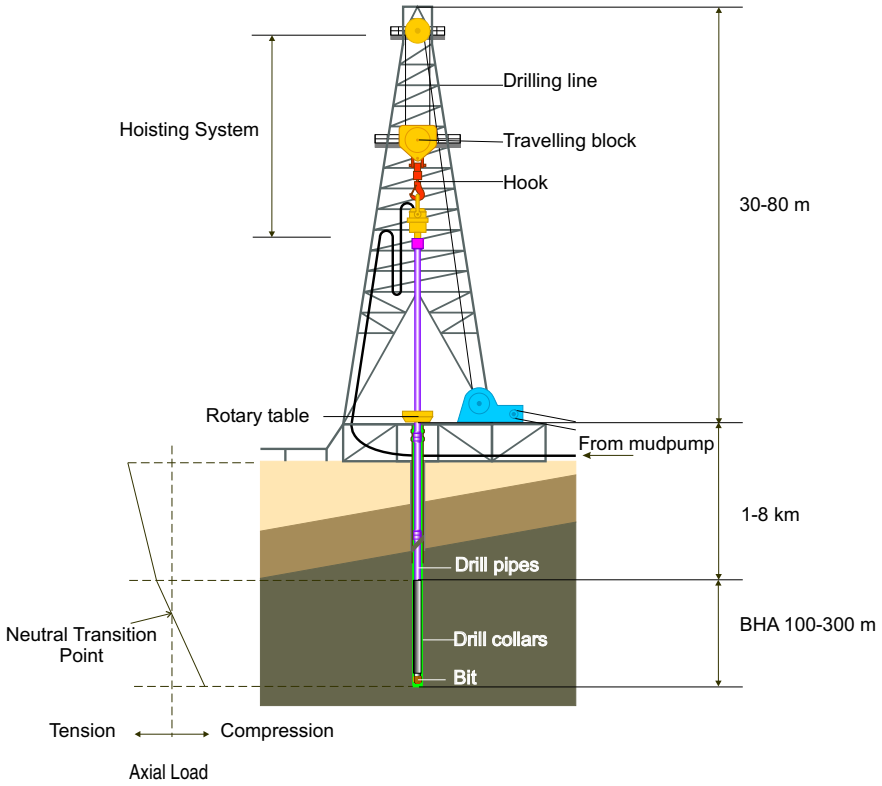

FIGURE 1.1: Schematic rotary drilling rig system and its components [1].

to the modelling and monitoring of drillstring vibrations, in order to (i) gain a better understanding of the root mechanism governing each vibration mode, and estimate their effects on the drilling assembly and drilling performance, (ii) and eventually propose methods to detect or mitigate their occurrence and reduce their associated damage (Wolf and Zacksenhouse, 1985 [2]; Aarrestad and Tonnesen, 1986 [3]; Aarrestad and Kyllingstad, 1988 [4]; Jansen ,1991 [5]; Brett, 1992 [6]; Aldred and Sheppard, 1992 [7]; Chen and Geradin, 1993 [8]; Van Der Heijden, 1993 [9]; Jansen and Van Den Steen, 1995 [10, 11]; Leine and Van Campen, 1998 [12, 13]; Kriesels and Keultjes, 1999 [14]; Santos and Placido, 1999 [15]; Spanos and Chevallier, 2002 [16]; Elsayed and Raymond, 2002 [17]; Bakenov and Gabler, 2003 [18]; Khulief and Al-Naser, 2005 [19, 20]; Hoffmann, 2006 [21]).

Fig. 1.2 illustrates the three different modes of drillstring vibrations: axial, torsional and lateral.

Torsional vibrations are characterised by periodic oscillations of the bit angular velocity, with the dominant frequency often very close to the first natural frequency of

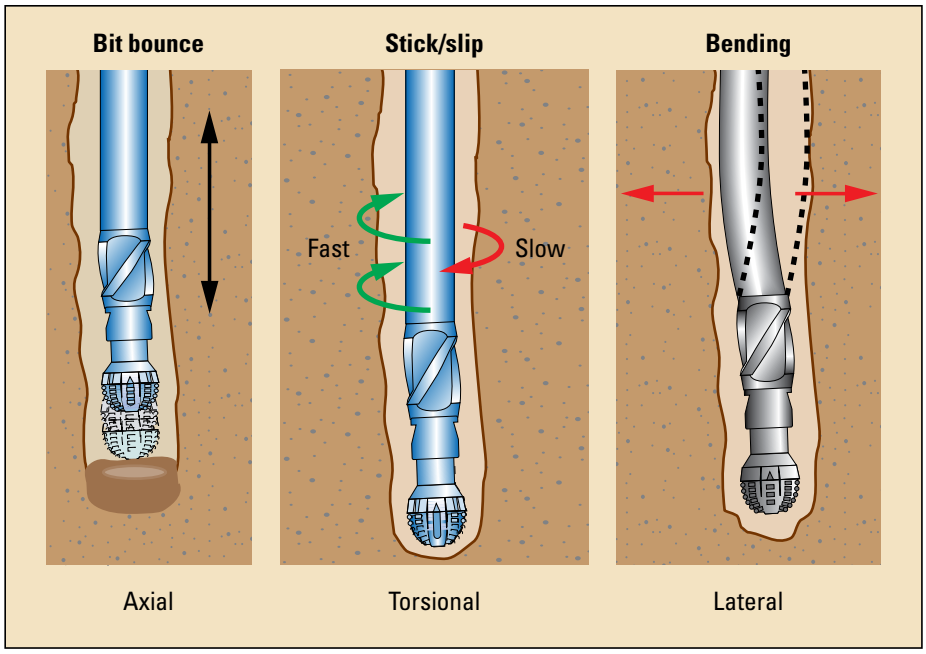

FIGURE 1.2: Schematic of the three different modes of drillstring vibrations.

the assembly. In their worst extent, they can lead to stick-slip oscillation characterised by periodic succession of events of complete halt and phases where the bit angular velocity increases up to 2-3 folds the surface velocity before decreasing all the way back to the next stick phase. During the stick phase, torsional energy is being accumulated in the drillstring as rotation is still imposed on surface, until the applied torque is sufficient for the bit to resume drilling. Events of backward rotations have been reported during severe stick - slip vibrations (Robnett and Hood, 1999 [22]) often leading to mechanical failure of the cutting structure. Typical field measurements of stick-slip oscillations are displayed in Fig. 1.3. Several torsional vibrations can last for many hours and lead to dramatic bit or drillstring failure. It is commonly accepted that the bit-rock interaction is the root cause to torsional vibrations (Brett, 1992 [6]; Richard et. al., 2006 [23])

Axial vibrations are quite common with a certain type of drill bits (roller cone) and can lead to full bit bouncing with the loss of contact between the bit and rock formation. These vibrations are triggered mainly due to bit-rock interaction but can also be caused by fluctuation in the hydraulic circulation system.

Lateral vibrations are often viewed as the most detrimental type of vibrations with associated accelerations of up to several tens of g's; they are often limited to the lower part of the BHA and thus not rarely detectable from surface measurements. They

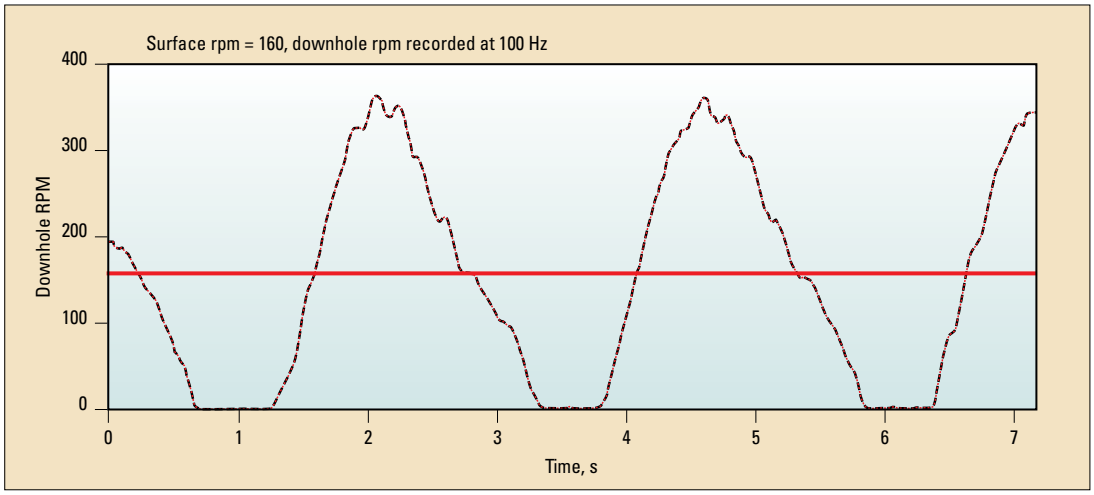

FIGURE 1.3: Surface and downhole angular velocity during stick-slip oscillation.

can be chaotic lateral motion of the BHA centre line (Chen and Geradin, 1995 [24]; Chen and Blackwood, 2002 [25,26]) or limit cycles with periodic precession of the BHA centre line around the borehole centre line (Brett and Warren, 1989 [27]), often referred as whirl (forward and backward whirl), see schematic in Fig. 1.4. Lateral vibrations can be caused by some eccentricity or mass imbalance in the drill collars which results in centripetal forces while the drillstring is rotating (Brett and Warren, 1989 [27]; Wu and Paez, 2010 [28]; Minett-Smith and Stroud, 2011 [29]). These forces move the bit instantaneous center of rotation away from its geometric center and push the BHA against the borehole walls causing additional frictional forces and eventually large shocks on the BHA. There are also some evidence that the three modes of vibrations can be coupled often through the bit-rock interface (Richard et. al., 2006 [30]).

Despite the existence of various mathematical models, there are only limited works dedicated to the real-time detection of the onset of vibrations. Over the past years, the drilling industry has made significant progress in introducing new technologies such as computer-based instrumentation to record drilling parameters downhole with high level of precision (Desmette and Will, 2005 [31]; Neubert, M. and Heisig, 2005 [32]; Ledgerwood and Hoffmann, 2010 [33]; Craig and Goodship, 2010 [34]). But there is still a need for fast, robust and reliable interpretation schemes and algorithms to explore the massive amount of data, eventually in real-time. Most commonly, downhole data are reduced to peak values or root mean square or power spectrum, which in turn activate simple alarm levels.

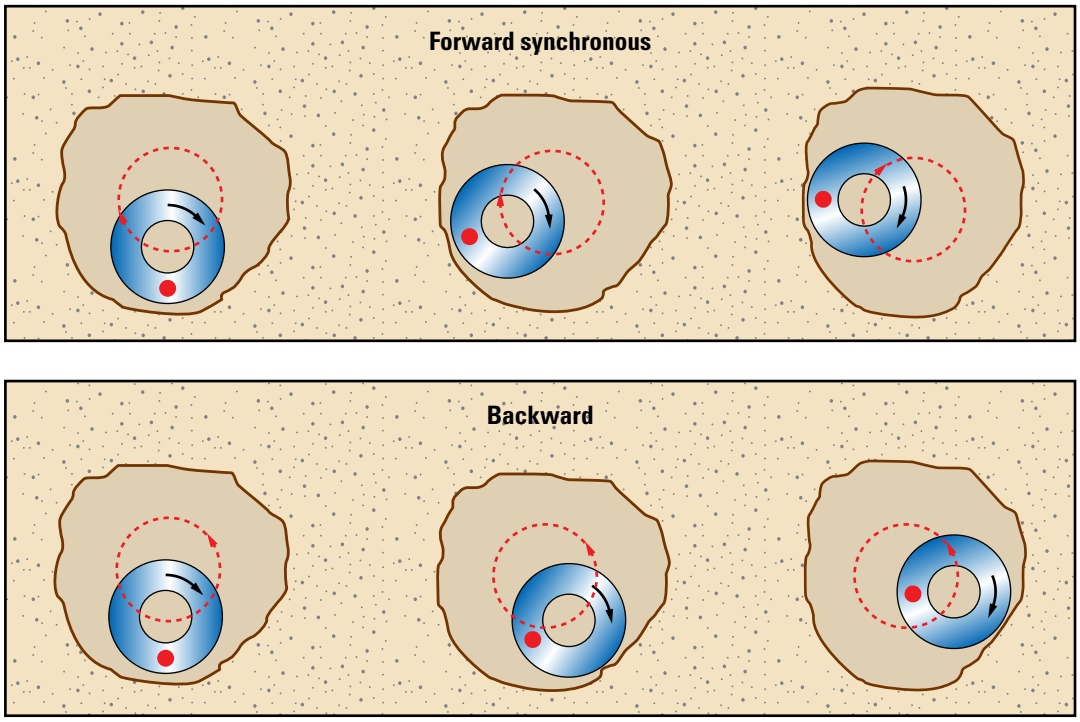

FIGURE 1.4: Schematic of forward and backward whirl.

1.2 Scope of Part I

The overarching goal of the work presented in Part I of this thesis is to eventually build algorithms to monitor and detect the onset of torsional (stick-slip) and lateral (whirl) vibrations. The first section is devoted to the estimation of the bit instantaneous angular velocity from accelerometer measurements using adaptive filters such as Kalman filters. The use of estimators like Kalman filters to derive the kinematic of a rigid body has attracted the attention of several researchers in different fields of studies such as robotics, vehicle guidance, control and automative industry (Belanger and Dobrovolny 1998 [35]; Negenborn, 2003 [36]; Han and He, 2007 [37]; Cardou and Angeles, 2009 [38, 39]). However, the data pertaining to drilling operations raise some uncommon challenges: the measurements are not only affected by the gravity (as the borehole can be inclined with respect to the vertical axis), but also bias error and noise whose properties drift with the borehole depth (often because of temperature). In addition, bit angular velocity and acceleration can reach values comparable to the noise level and be actually nil (stick phase). There are only limited works related to the use of Kalman filters on drilling data measurements and most related to different topic, for instance,

the work on rate of penetration (ROP) estimation using surface measurements (Booer, 1996 [40]) or surveying of wellbore trajectory while drilling (ElGizawy and Noureldin, 2010 [41]).

1.3 Outline of Part I

The problem is first formulated mathematically in chapter 2, the accelerometers measurements are expressed as a function of the bit kinematics considering any in plane motion. In chapter 3, an extended Kalman filter model is introduced to estimate the bit instantaneous angular velocity. The model is then implemented on field data and results are compared with numerical results obtained from an alternative (magnetometer) measurement. In the conclusions, the issues associated with the use of accelerometers measurement to infer attributes of the out of centre kinematics (such as precession or whirl) and outline some possible methods for particular cases are discussed. In addition, recommendations on further study on this topic are presented.

Chapter 2

Problem Formulation

2.1 Introduction

We consider a measurement tool whose centre line is inclined by an angle γ with respect to the gravity field. Four accelerometers are mounted on its cross-section; they are regularly spaced by an angle $\frac{\pi}{2}$ and the locus of measurement is located at a distance r from the tool centre line ($O^{'}M_i = r$). All four accelerometers have a measurement axis whose orientation is "radial',' i.e. aligned with the tool centre $O^{'}$, and the measurement locus (or aligned with the segment $O^{'}M_i$). One of the accelerometers has a second axis of measurement whose orientation is "tangent", i.e. normal to the radial direction. Orientations and sign conventions are shown in Fig. 2.1, where the directions of a positive measure of acceleration are given by the unit vectors $\mathbf{n}_i$. We then introduce two reference frames, one fixed (XY) and one (xy) rotating around the tool centre line. The positions of the measurement points M_i are then defined by vectors $\mathbf{R}_i$ and $\mathbf{r}_i$ in the fixed and rotating frames, respectively; and the position of the tool centre point in the fixed frame is described by vector $\mathbf{R}$.

2.2 Governing Equations

The planar acceleration ($\ddot{\mathbf{R}}_i$) of the point M_i with respect to the fixed reference (XY) can be written as [42]

$$\begin{aligned} \ddot{\mathbf{R}}_i &= \ddot{\mathbf{R}} + \ddot{\mathbf{r}}_i \\ &= \ddot{\mathbf{R}} - \omega^2 \mathbf{r}_i + \dot{\omega} \times \mathbf{r}_i \,, \qquad i = 1, ..., 5, \end{aligned} \tag{2.1}$$

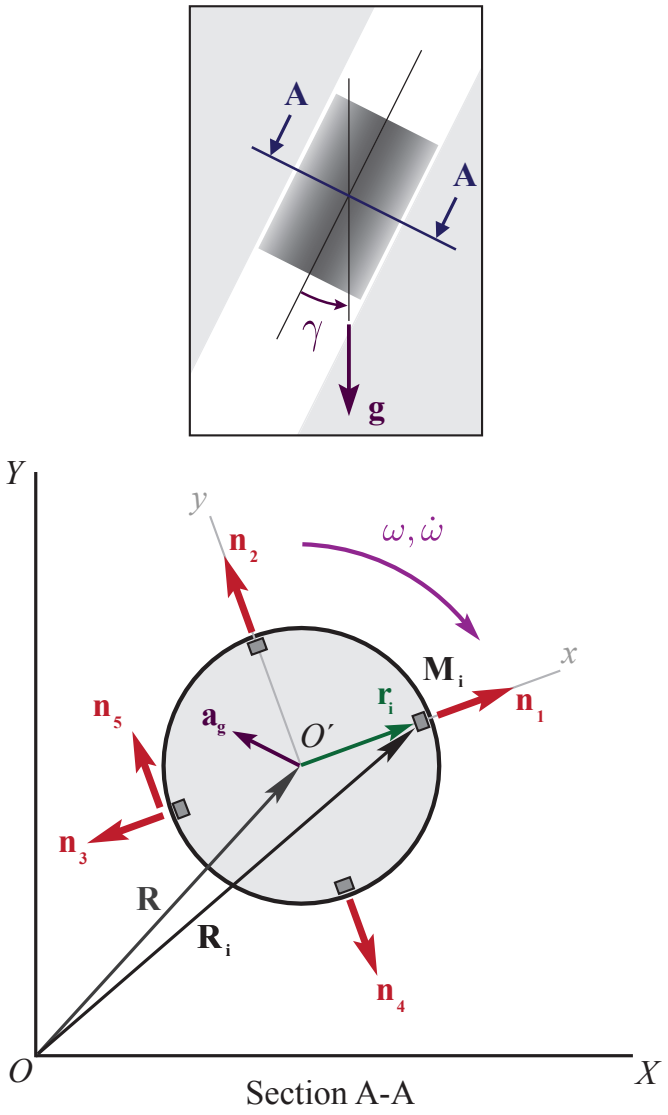

FIGURE 2.1: Top: sketch of vertical cross section of a tool in a borehole. Bottom: Locations of the accelerometers on the tool cross section and measurement axes.

where $\ddot{\mathbf{R}}$ is the acceleration of the point $O^{'}$ with respect to the fixed frame (XY) and ω and $\dot{\omega}$ are the angular velocity and angular acceleration of the tool around its centre line, respectively. The notation $(\dot{})$ denotes the first and $(\ddot{})$ the second derivative with respect to time. The word "planar" means here only trajectories located within the cross-section plane of the tool are considered. The total acceleration "sensed" by the sensor along its axis of measurement is given by

$$a_i = \mathbf{n}_i^T(\ddot{\mathbf{R}}_i - \mathbf{a}_g), \tag{2.2}$$

where $\mathbf{a}_g$ is the projection of the gravity field on the cross sectional plane ($a_g = g \sin\gamma$). It is important to stress that a_i is not the output measurement which is also affected by bias and noise caused by manufacturing imperfections, effect of temperature, and electrical interferences. Substituting Eq. (2.1) in Eq. (2.2) we can rewrite

$$a_i = \mathbf{n}_i^T \left(\ddot{\mathbf{R}} - \mathbf{a}_g\right) - \omega^2 \, \mathbf{n}_i^T \, \mathbf{r}_i + \mathbf{n}_i^T \, \left(\dot{\omega} \times \mathbf{r}_i\right). \tag{2.3}$$

The sensors configuration on the measurement tool cross-section in the rotating frame shown in Fig. 2.1 is described by

$$\mathbf{n}_1 = \begin{bmatrix} 1 \\ 0 \end{bmatrix}, \mathbf{n}_2 = \mathbf{n}_5 = \begin{bmatrix} 0 \\ 1 \end{bmatrix}, \mathbf{n}_3 = \begin{bmatrix} -1 \\ 0 \end{bmatrix}, \mathbf{n}_4 = \begin{bmatrix} 0 \\ -1 \end{bmatrix}, \tag{2.4}$$

and

$$\mathbf{r}_1 = \begin{bmatrix} r \\ 0 \end{bmatrix}, \mathbf{r}_2 = \begin{bmatrix} 0 \\ r \end{bmatrix}, \mathbf{r}_3 = \mathbf{r}_5 = \begin{bmatrix} -r \\ 0 \end{bmatrix}, \mathbf{r}_4 = \begin{bmatrix} 0 \\ -r \end{bmatrix}. \tag{2.5}$$

Substituting Eqs. (2.4) and (2.5) in (2.3), yields a system of equations presented by

$$\mathbf{A}\,\mathbf{x} = \mathbf{b}, \tag{2.6}$$

where the coefficients matrix, $\mathbf{A}$, the unknown's vector, $\mathbf{x}$, and output vector $\mathbf{b}$, are given by

$$\mathbf{A} = \begin{bmatrix} -r & 0 & 1 & 0 \\ -r & 0 & 0 & 1 \\ -r & 0 & -1 & 0 \\ -r & 0 & 0 & -1 \\ 0 & r & 0 & 1 \end{bmatrix}, \qquad \mathbf{x} = \begin{bmatrix} \omega^2 \\ \dot{\omega} \\ \ddot{R}_x \\ \ddot{R}_y \end{bmatrix}, \qquad \mathbf{b} = \begin{bmatrix} a_1 + (\mathbf{a}_g)_x \\ a_2 + (\mathbf{a}_g)_y \\ a_3 - (\mathbf{a}_g)_x \\ a_4 - (\mathbf{a}_g)_y \\ a_5 + (\mathbf{a}_g)_y, \end{bmatrix}, \tag{2.7}$$

with $\ddot{R}_x$ and $\ddot{R}_y$ the components of the acceleration $\ddot{\mathbf{R}}$ of the tool center along the rotating frame axes, x and y, respectively. Also, $(\mathbf{a}_g)_x$ and $(\mathbf{a}_g)_x$ correspond to the projection of the gravity component, $\mathbf{a}_g$, along x and y axes. Solving the system of equations provides

$$\mathbf{x} = \mathbf{A}^{\dagger}\,\mathbf{b}, \tag{2.8}$$

where $\mathbf{A}^{\dagger}$ is the Moore-Penrose pseudoinverse of $\mathbf{A}$ and is given by

$$\mathbf{A}^{\dagger} = \begin{bmatrix} -\frac{1}{4\,r} & -\frac{1}{4\,r} & -\frac{1}{4\,r} & -\frac{1}{4\,r} & 0 \\ 0 & -\frac{1}{2\,r} & 0 & \frac{1}{2\,r} & \frac{1}{r} \\ \frac{1}{2} & 0 & -\frac{1}{2} & 0 & 0 \\ 0 & \frac{1}{2} & 0 & -\frac{1}{2} & 0. \end{bmatrix}. \tag{2.9}$$

After substituting Eqs.(2.7) and (2.9) in Eq.(2.8), the unknowns, i.e. the angular velocity ω, angular acceleration $\dot{\omega}$ and x and y components of the tool center acceleration, $\ddot{R}_{x}$ and $\ddot{R}_{y}$, read

$$\omega^2(t) = -\frac{1}{4\,r}\sum_{i=1}^{4} a_i(t) \tag{2.10}$$

$$\dot{\omega}(t) = \frac{1}{2\,r}\left[2a_{5}(t) + a_{4}(t) - a_{2}(t)\right] \tag{2.11}$$

$$\ddot{R}_{x} = \frac{1}{2}\left[a_{1}(t) - a_{3}(t)\right] + \left(\mathbf{a}_g(t)\right)_{x} \tag{2.12}$$

$$\ddot{R}_{y} = \frac{1}{2}\left[a_{2}(t) - a_{4}(t)\right] + \left(\mathbf{a}_g(t)\right)_{y}. \tag{2.13}$$

Eqs. (2.10) and (2.11) indicate that for the sensors configuration under consideration, both the tool angular velocity, ω, and angular acceleration, $\dot{\omega}$, are independent of the gravity field.

2.3 An Alternative Formulation

Motivated by field and laboratory observation as well as model predictions; it is of interest to consider an alternative formulation to Eq. (2.1) by decomposing the motion as the combination of two instantaneous rotations: one around its own axis of revolution (tool angular velocity) and one around another axis located at distance R from the first (rotating frame xy).

$$\begin{aligned} \ddot{\mathbf{R}}_i &= \ddot{\mathbf{R}} + \ddot{\mathbf{r}}_i \\ &= \ddot{R}\,\mathbf{n}_{R} + 2\dot{R}\,\Omega\,\mathbf{n}_{\beta} + \dot{\mathbf{\Omega}} \times \mathbf{R} - \Omega^2\,\mathbf{R} + \dot{\omega} \times \mathbf{r_i} - \omega^2 \mathbf{r_i}, \quad i = 1, ..., 5, \end{aligned} \tag{2.14}$$

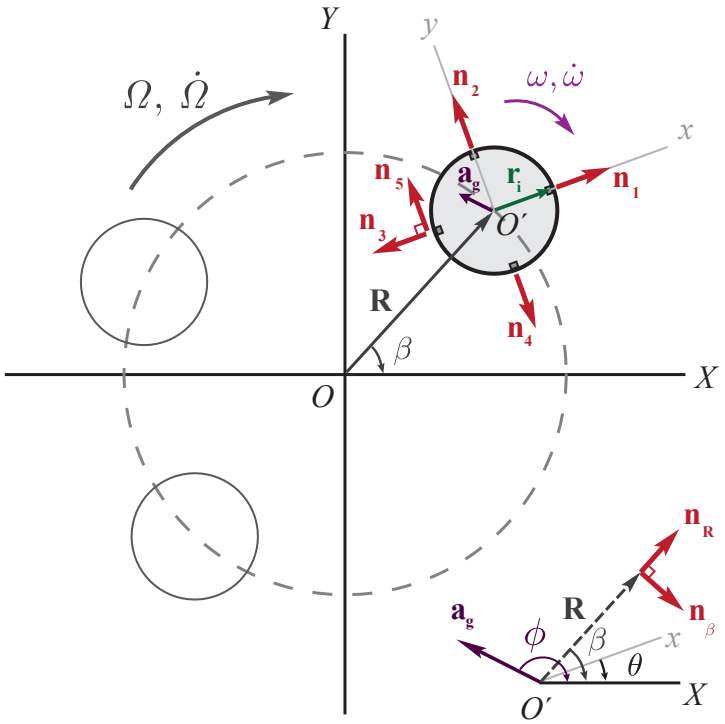

FIGURE 2.2: Bit kinematics decomposed into two instantaneous rotations.

where R and Ω are the instantaneous radius and angular whirl velocity, respectively, with

$$\Omega = \frac{d\beta}{dt}, \quad \dot{\Omega} = \frac{d\Omega}{dt} = \frac{d^2\beta}{dt^2}. \tag{2.15}$$

The unit vectors $\mathbf{n}_R$ and $\mathbf{n}_\beta$ are normal and tangential to $\mathbf{R}$. This formulation is more suited to describe whirl type trajectory. The acceleration recorded by each sensor can be written using Eqs. (2.2) and (2.14) as follows

$$\begin{aligned}
a_1 &= \left[\ddot{R} + R\Omega^2\right]\cos(\beta-\theta) + \left[2\dot{R}\Omega + R\dot{\Omega}\right]\sin(\beta-\theta) - g\sin\gamma\cos(\phi-\theta) - r\omega^2 \\
a_2 &= \left[\ddot{R} + R\Omega^2\right]\sin(\beta-\theta) - \left[2\dot{R}\Omega + R\dot{\Omega}\right]\cos(\beta-\theta) - g\sin\gamma\sin(\phi-\theta) - r\omega^2 \\
a_3 &= -\left[\ddot{R} + R\Omega^2\right]\cos(\beta-\theta) - \left[2\dot{R}\Omega + R\dot{\Omega}\right]\sin(\beta-\theta) + g\sin\gamma\cos(\phi-\theta) - r\omega^2 \\
a_4 &= -\left[\ddot{R} + R\Omega^2\right]\sin(\beta-\theta) + \left[2\dot{R}\Omega + R\dot{\Omega}\right]\cos(\beta-\theta) + g\sin\gamma\sin(\phi-\theta) - r\omega^2 \\
a_5 &= \left[\ddot{R} + R\Omega^2\right]\sin(\beta-\theta) - \left[2\dot{R}\Omega + R\dot{\Omega}\right]\cos(\beta-\theta) - g\sin\gamma\sin(\phi-\theta) + r\dot{\omega},
\end{aligned}$$

with $R(t)$, $\Omega(t)$, $\omega(t)$ and $\gamma(t)$ as unknowns. Although the borehole inclination γ may varies with time (in no straight borehole), it does at a time scale much slower than the other 3 unknowns.

Two particular cases are of particular interest, they correspond of a kinematic with

a constant radius of whirl.

Constant Whirl Velocity and Radius

$\Omega = const$, $\dot{\Omega} = 0$, $R = const$, $\dot{R} = \ddot{R} = 0$

$$\begin{aligned}
a_1 &= R\,\Omega^2\,\cos(\beta-\theta) - g\sin\gamma\cos(\phi-\theta) - r\omega^2 \\
a_2 &= R\,\Omega^2\,\sin(\beta-\theta) - g\sin\gamma\sin(\phi-\theta) - r\omega^2 \\
a_3 &= -R\,\Omega^2\,\cos(\beta-\theta) + g\sin\gamma\cos(\phi-\theta) - r\omega^2 \\
a_4 &= -R\,\Omega^2\,\sin(\beta-\theta) + g\sin\gamma\sin(\phi-\theta) - r\omega^2 \\
a_5 &= R\,\Omega^2\,\sin(\beta-\theta) - g\sin\gamma\sin(\phi-\theta) + r\dot{\omega}.
\end{aligned}$$

Varying Whirl Velocity, Constant Whirl Radius

Ω, $\dot{\Omega}$, $R = const$, $\dot{R} = \ddot{R} = 0$

$$\begin{aligned}
a_1 &= R\,\Omega^2\cos(\beta-\theta) + R\,\dot{\Omega}\sin(\beta-\theta) - g\sin\gamma\cos(\phi-\theta) - r\omega^2 \\
a_2 &= R\,\Omega^2\sin(\beta-\theta) - R\,\dot{\Omega}\cos(\beta-\theta) - g\sin\gamma\sin(\phi-\theta) - r\omega^2 \\
a_3 &= -R\,\Omega^2\cos(\beta-\theta) - R\,\dot{\Omega}\sin(\beta-\theta) + g\sin\gamma\cos(\phi-\theta) - r\omega^2 \\
a_4 &= -R\,\Omega^2\sin(\beta-\theta) + R\,\dot{\Omega}\cos(\beta-\theta) + g\sin\gamma\sin(\phi-\theta) - r\omega^2 \\
a_5 &= R\,\Omega^2\sin(\beta-\theta) - R\,\dot{\Omega}\cos(\beta-\theta) - g\sin\gamma\sin(\phi-\theta) + r\dot{\omega}.
\end{aligned}$$

Chapter 3

Determination of the Angular Velocity ω

3.1 Introduction

The goal of this chapter is to provide a robust method to compute in real-time, the tool instantaneous angular velocity using accelerometer and magnetometer recordings, separately, taking into account sensors bias and noise.

The first method proposed in this section relies on an extended Kalman filter model based on the dynamic model introduced in chapter 2 to relate the angular velocity and acceleration of the measurement sub to the accelerometer recordings at any instant of time. The Kalman filter is an optimal method to estimate the instantaneous state of a physical dynamic system considering dynamic uncertainties and indirect measurements perturbed by white noise. The state space notation of the continuous dynamic system is introduced first to provide an appropriate formulation to derive the discrete Kalman filter model. Methods to account and characterise noise, and bias are also discussed.

The second proposed algorithm deals with the frequency demodulation of the recordings of a magnetometer using Hilbert transform to estimate the instantaneous frequency of the sensor recording as a measure of the bit angular velocity.

Both models are then implemented on field data with particular attention to cases characterised by very low angular velocity and events of stick (zero angular velocity). Several simulations using downhole measurements with various duration are performed and the results are compared to the conventional methods existing in the literature.

Eventually, the advantages and disadvantages associated with each algorithm are discussed in detail.

3.2 Accelerometers

3.2.1 State Space Model

Mathematical models for physical systems are often expressed with a system of differential equations. It is usually very convenient to rewrite these equations as a system of first order differential equations that is usually referred to as the state space representation. Inputs, outputs and state variables of the continuous dynamic systems are related by state space model. The solution of this system is a time dependant vector (state vector) that contains information of the state of the dynamic system at any instant of time.

The model of the linear dynamic system for a rotating shaft in continuous time is described by [43],

$$\dot{\mathbf{x}}(t) = A\,\mathbf{x}(t) + B\,u(t), \tag{3.1}$$

where $\mathbf{x}(t)$ is a system state vector at time t, $u(t)$ is the system input, A is state coefficient matrix, B is the input coupling vector, and $(\dot{})$ denotes the first derivative with respect to time.

The state variables are chosen as the angular velocity, $\omega(t)$, and angular acceleration, $\dot{\omega}(t)$ of the tool

$$\mathbf{x}(t) = \begin{bmatrix} \omega(t) \\ \dot{\omega}(t) \end{bmatrix}, \quad \dot{\mathbf{x}}(t) = \begin{bmatrix} \dot{\omega}(t) \\ \ddot{\omega}(t) \end{bmatrix}, \tag{3.2}$$

where $(\ddot{})$ denotes the second derivative with respect to time. The input vector $u(t)$ is thus given as the second derivative of the angular velocity i.e. $\ddot{\omega}$. The matrix A and vector B are defined by

$$A = \begin{bmatrix} 0 & 1 \\ 0 & 0 \end{bmatrix}, \qquad B = \begin{bmatrix} 0 \\ 1 \end{bmatrix}. \tag{3.3}$$

Note that in state space notation, Eq. (3.1) is called the state equation.

3.2.2 Extended Kalman Filter

In most Kalman filter applications, the discrete models are usually used rather than continuous implementations even when the system is continuous, because the mea-

surements are always recorded in a discrete manner. Also, the non-linearity between measurements and state variables imply the use of a particular class of filters, the Extended Kalman Filters (EKF). In the EKF formulation, the non-linear system dynamic and measurement models is expanded into a first-order Taylor series about the current estimate [44].

We introduce $\mathbf{x}_k = \begin{bmatrix} \omega_k & \dot{\omega}_k \end{bmatrix}^T$ and $\mathbf{y}_k = \begin{bmatrix} \hat{\omega}_k^2 & \hat{\dot{\omega}}_k \end{bmatrix}^T$ as the discrete state and measurement vectors where ($\hat{}$) stands for the measurements, and formulate the discrete-time extended Kalman filter model using the continuous state space model introduced earlier in sec 3.2.1. Hence

$$\mathbf{x}_k = \mathbf{F}\,\mathbf{x}_{k-1} + \mathbf{w}_{k-1} \tag{3.4}$$

$$\mathbf{y}_k = \mathbf{h}(\mathbf{x}_k) + \mathbf{v}_k, \tag{3.5}$$

where $\mathbf{F}$ is the state transition matrix, and $\mathbf{y}$ is the measurement vector which is described as a function of the state vector with $\mathbf{h}(\cdot)$. The process noise, $\mathbf{w}_k$ (see 3.2.2.1) and measurement noise, $\mathbf{v}_k$ (see 3.2.2.3) are Gaussian, white, uncorrelated, and with zero-mean and known covariance matrices $\mathbf{Q}_k$ and $\mathbf{R}_k$,

$$\mathbf{w}_k \sim \mathcal{N}(0, \mathbf{Q}_k), \quad \mathbf{v}_k \sim \mathcal{N}(0, \mathbf{R}_k), \tag{3.6}$$

also

$$E\left[\mathbf{w}_k \mathbf{w}_j^T\right] = \mathbf{Q}_k\,\delta_{k-j}, \quad E\left[\mathbf{v}_k \mathbf{v}_j^T\right] = \mathbf{R}_k\,\delta_{k-j}, \quad E\left[\mathbf{w}_k \mathbf{v}_j^T\right] = 0, \tag{3.7}$$

where δ_{k-j} is the Kronecker delta function (that is, $\delta_{k-j} = 1$ if $k = j$, and $\delta_{k-j} = 0$ if $k \neq j$) and $E[\cdot]$ stands for the expected value.

The variables of the discrete state model are derived by integrating the continuous dynamic model of Eq. (3.1) over intervals t_{k-1} to t_k assuming that the sampling interval $T = t_k - t_{k-1}$ is constant with no missing measurements, and that the system is a stationary random process such that the means and autocorrelation functions do not change with time shifts [44, 45]. Therefore, the state transition matrix reads

$$\mathbf{F} = \exp\left(\int_{t_{k-1}}^{t_k} A\,dt\right), \tag{3.8}$$

while the process noise is calculated by

$$\mathbf{w}_{k-1} = \mathbf{F}\int_{t_{k-1}}^{t_k} \exp\left(-\int_{t_{k-1}}^{t_k} A\,d\tau\right) B\,u(t)\,d(t). \tag{3.9}$$

For small values of the time step T, $\mathbf{F}$ can be approximated using Taylor series expansion yielding

$$\mathbf{F} \approx \begin{bmatrix} 1 & T \\ 0 & 1 \end{bmatrix}. \tag{3.10}$$

The function $\mathbf{h}(\cdot)$ represents the non-linear relationship between measurements and state variables and is defined by

$$\mathbf{h}(\mathbf{x}_k) = \begin{bmatrix} h_1(x_k) \\ h_2(x_k) \end{bmatrix}, \tag{3.11}$$

where

$$h_1(x_k) = \omega_k^2 + \beta_{\hat{\omega}^2} \tag{3.12}$$

$$h_2(x_k) = \dot{\omega}_k + \beta_{\dot{\hat{\omega}}}, \tag{3.13}$$

with $\beta = \begin{bmatrix} \beta_{\hat{\omega}^2} & \beta_{\dot{\hat{\omega}}} \end{bmatrix}^T$ the bias vector due to measurement offset.

The process begins with the estimation of the state vector at $k = 0$. The vector $\hat{\mathbf{x}}_0^+$ is introduced as the initial estimate of the true state, $\mathbf{x}_0$, before any measurement is available and is defined as the expected value of the initial state since there is no measurement available to estimate $\mathbf{x}_0$,

$$\hat{\mathbf{x}}_0^+ = E(\mathbf{x}_0). \tag{3.14}$$

The uncertainty in our initial estimate is considered by introducing $\mathbf{P}_0^+$ as the covariance of the initial estimation error,

$$\mathbf{P}_0^+ = E\left[\left(\mathbf{x}_0 - \hat{\mathbf{x}}_0^+\right)\left(\mathbf{x}_0 - \hat{\mathbf{x}}_0^+\right)^T\right]. \tag{3.15}$$

If the initial state is known precisely, then $\mathbf{P}_0^+ = 0$. Otherwise, if $\hat{\mathbf{x}}_0^+$ is absolutely unknown, $\mathbf{P}_0^+$ will be chosen as large as possible ($\mathbf{P}_0^+ = \infty I$).

The covariance of the estimation error $\mathbf{P}_k$ is estimated for $\hat{\mathbf{x}}_k^-$ ($\mathbf{P}_k^-$) and $\hat{\mathbf{x}}_k^+$ ($\mathbf{P}_k^+$)

$$\mathbf{P}_k^- = E\left[\left(\mathbf{x}_k - \hat{\mathbf{x}}_k^-\right)\left(\mathbf{x}_k - \hat{\mathbf{x}}_k^-\right)^T\right] \tag{3.16}$$

$$\mathbf{P}_k^+ = E\left[\left(\mathbf{x}_k - \hat{\mathbf{x}}_k^+\right)\left(\mathbf{x}_k - \hat{\mathbf{x}}_k^+\right)^T\right]. \tag{3.17}$$

The "$-$" subscript denotes that the estimate is *a priori*. It is used when we have all of the measurements before (but not including) time k available in our estimate of $\mathbf{x}_k$. When we have all the measurements up to and including time k available to estimate $\mathbf{x}_k$, then we can form an *a posteriori* estimate which is denoted with "+" subscript.

The process to estimate the state variables with Kalman filters is two fold: prediction and correction.

During the prediction step, the estimate of the state vector and the associated covariance of the estimation error are updated considering the effect of uncertain system dynamics over the time step T. In some references, it is referred to as the time update [45],

$$\hat{\mathbf{x}}_k^- = \mathbf{F}_{k-1}\,\hat{\mathbf{x}}_{k-1}^+ \tag{3.18}$$

$$\mathbf{P}_k^- = \mathbf{F}_{k-1}\mathbf{P}_{k-1}^-\mathbf{F}_{k-1}^T + \mathbf{Q}_{k-1}. \tag{3.19}$$

At the correction step, the state variables estimate and its uncertainty are updated based on the sensor measurements and their associated random error, it is also called the measurement update. The measurement update equations of $\hat{\mathbf{x}}_k$ and $\mathbf{P}_k$ are given by

$$\mathbf{K}_k = \mathbf{P}_k^-\mathbf{H}_k^T\left(\mathbf{H}_k\mathbf{P}_k^-\mathbf{H}_k^T + \mathbf{R}_k\right)^{-1} \tag{3.20}$$

$$\hat{\mathbf{x}}_k^+ = \hat{\mathbf{x}}_k^- + \mathbf{K}_k(\mathbf{y}_k - \mathbf{H}_k\hat{\mathbf{x}}_k^-) \tag{3.21}$$

$$\mathbf{P}_k^+ = (\mathbf{I} - \mathbf{K}_k\mathbf{H}_k)\mathbf{P}_k^-, \tag{3.22}$$

where $\mathbf{K}_k$ is the Kalman gain and $\mathbf{H}_k$ is the Jacobian of the nonlinear relationship between measurements and state variables and is updated at each time step

$$\mathbf{H}_k = \left.\frac{\partial \mathbf{h}_k}{\partial \mathbf{x}}\right|_{\hat{\mathbf{x}}_k^-}. \tag{3.23}$$

The equations describing the propagation of the covariance error, shows how the sensor and process noises and also dynamic uncertainties contribute to the estimated system state. The Kalman gain is described as a weighting matrix which combines sensor measurements with a prior estimate to obtain a new estimate. It is in fact a partial solution of the so called Riccati equation [43].

3.2.2.1 Process Noise

The process noise $\mathbf{w}_k$ is a random vector defined as

$$\mathbf{w}_k = \begin{bmatrix} \frac{1}{2}T^2 \\ T \end{bmatrix} \ddot{\omega}_k, \tag{3.24}$$

where $\ddot{\omega}_k$ is the second derivative of the angular velocity also referred as the angular jerk.

To calculate the covariance of the process noise, the knowledge about the variance of the angular jerk is required. This can be inferred from a priori known dynamic properties of the mechanical structure the tool is mounted on. Field observation and measurements supported by modelling indicate that the dominant frequency of the torsional vibrations occurring while drilling (f_*) is very close to the first natural frequency of the drilling assembly [6, 46]. The angular velocity can thus be expressed as

$$\omega(t) \simeq \frac{1}{2}\omega_* \left(1 - \cos\left(2\pi f_* t\right)\right), \tag{3.25}$$

where the amplitude ω_* of the oscillation is typically found as high as 2 or 3 times the mean velocity , i.e $0 \leq \omega_* \leq (2 \sim 3)\,\omega_o$ with ω_o the average angular velocity imposed on surface [46]. Taking the second derivative of Eq. (3.25) with respect to time yields to

$$\ddot{\omega}(t) \simeq 2\left(\pi f_*\right)^2 \omega_* \cos\left(2\pi f_* t\right). \tag{3.26}$$

The variance of the jerk can then be determined by [38]

$$\begin{aligned} \sigma_{\ddot{\omega}}^2 &= \lim_{t\to+\infty}\left(\frac{1}{t}\int_0^t (\ddot{\omega}(u))^2 \mathrm{d}u\right) \\ &= 2\left(\pi f_*\right)^4 \left(\omega_*\right)^2. \end{aligned} \tag{3.27}$$

3.2.2.2 Bias Error

Accounting for the bias error β_i and the noise υ_i, the accelerometer output reads

$$\hat{a}_i = \mathbf{n}_i^T(\ddot{\mathbf{R}}_i - \mathbf{a}_g) + \beta_i + \upsilon_i. \tag{3.28}$$

The bias is known to drift with the downhole temperature that varies with the borehole depth. However, it can be estimated from the accelerometer measurements when the drilling operation is interrupted in order to add a new pipe to the drilling assembly. During a connection, the tool is steady and not rotating

$$\hat{a}_i = -\mathbf{n}_i^T \mathbf{a}_g + \beta_i + \upsilon_i. \tag{3.29}$$

The value of the bias is assumed constant between two consecutive connections, and determined from the accelerometer measurements averaged over the duration of the connection (when the tool is non rotating)

$$\begin{bmatrix} \beta_{\hat{\omega^2}} \\ \beta_{\hat{\dot{\omega}}} \end{bmatrix} = mean\left(\begin{bmatrix} \hat{\omega}_k^2 \\ \hat{\dot{\omega}}_k \end{bmatrix}\right)_c, \tag{3.30}$$

where the subscript ($_c$) stands for data recorded when the tool is not rotating (connection).

3.2.2.3 Measurement Noise

The measurement noise of each accelerometer is considered to be white and following a Gaussian distribution. It is legitimate to assume that the noises associated to all accelerometers are uncorrelated; the covariance matrix of the measurement noise vector can thus be written as

$$\mathbf{R}_k = \begin{bmatrix} \frac{1}{4\,r^2} & 0 \\ 0 & \frac{3}{2\,r^2} \end{bmatrix} \sigma_a^2, \tag{3.31}$$

where σ_a^2 is the variance of the noise intrinsic to the sensor and is provided by the sensor manufacturer.

3.3 Magnetometer

Magnetometer is a sensor used to measure the intensity of the magnetic field in the vicinity of the measurement tool.

The magnetometer measures the intensity of the the projection of the earth magnetic field along the sensor sensitivity axis ($\mathbf{n}_{\mathrm{M}}$), see sketch in Fig. 3.1. As a results, when the magnetometer is at position A (aligned with the earth field), the sensor measures the maximum value (H_{Max}) and at C, the magnetometer measurement is minimum (H_{Min}). In an ideal situation when there is no bias associated with the magnetometer, the sensor records zero when its position is either at B or D as the sensor axis is perpendicular to the magnetic north direction.

The magnetometer measurement, $H(t)$, at any instant of time can thus be written as

$$H(t) = H_{\mathrm{Max}}(t)\,\cos\theta(t) + \beta_m, \tag{3.32}$$

where $\theta(t)$ is the instantaneous angular position of the magnetometer with respect to the magnetic north direction and β_m stands for the sensor bias. Eq. (3.32) implies that the magnetometer measurement is proportional to the cosine of the angle between the sensor sensitivity axis and the magnetic north. Therefore, this measurement can be used to reconstruct the angular position of the measurement tool with respect to the magnetic north and consequently, the angular velocity of the measurement tool.

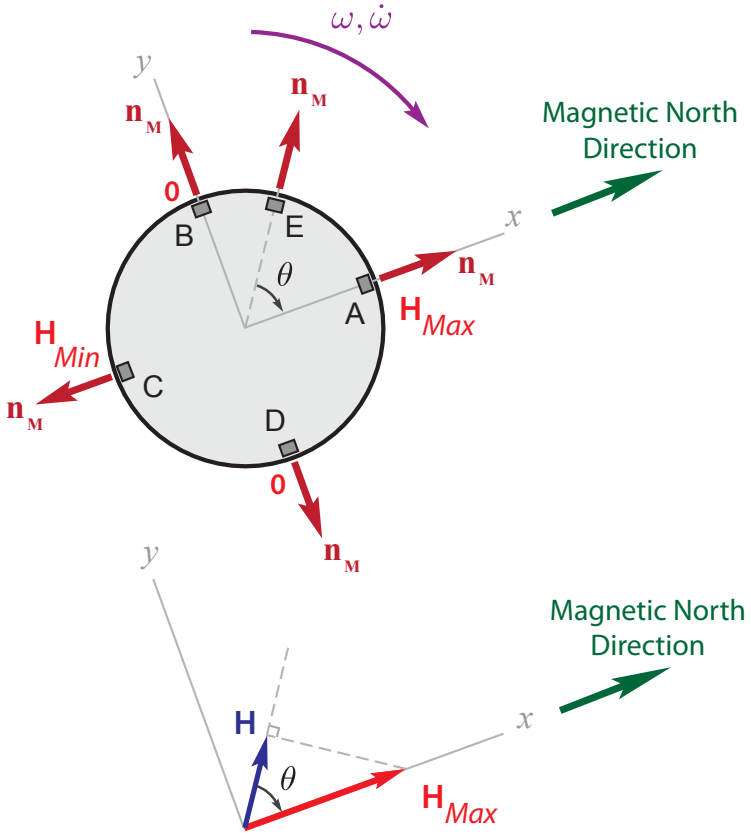

FIGURE 3.1: Magnetometer reading in relation to the sensor angular position with respect to the magnetic North.

Fig. 3.2 shows an example of the signal recorded by the magnetometer sensor for a period of 10 seconds where the interval between two consecutive peaks implies one full revolution of the measurement tool. However, the data indicate that the peak value is not exactly constant, this is in part explained by a parasitic magnetic field caused by the rotation of the drill rod and tool itself that is made of a magnetic material [47, 48].

The lack of repeatability in the measurement (in relation to the tool angular position), added to the fact that the *arccos* function is a non-single valued function (unique solution in terms of angle would require a second magnetometer ideally oriented perpendicular to the first one), motivated the use of Hilbert transform to demodulate the signal and infer the instantaneous frequency of the signal that is actually equivalent to the angular velocity of the measurement tool.

The Hilbert transform of a function $x(t)$ is given by an integral transform defined by [49]

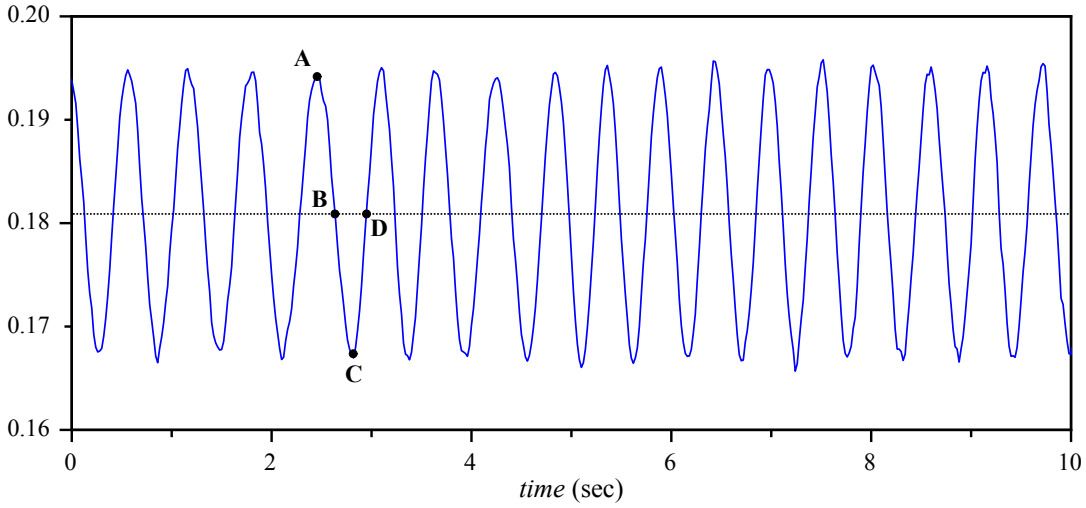

FIGURE 3.2: Magnetometer recording, the points A, B, C and D correspond to the tool positions shown in Fig 3.1.

$$\tilde{x}(t) = \frac{1}{\pi} P \int_{-\infty}^{+\infty} \frac{x(\tau)}{t-\tau}\, d\tau, \tag{3.33}$$

where $\tilde{x}(t)$ is the Hilbert transform of the function $x(t)$ and P stands for the Cauchy principal value of the integral because of a possible singularity at $t = \tau$. Hilbert transform operates as a linear filter keeping the amplitude of the frequency content of the signal unchanged, while shifting the phase by $\frac{\pi}{2}$. An example of the magnetometer measurement versus its Hilbert projection is illustrated in Fig. 3.3 with the phase lag of $\frac{\pi}{2}$ clearly noticeable. Note that the measurement DC component is removed prior to applying the transform.

The complex signal with real part $x(t)$ and imaginary part $\tilde{x}(t)$ is called the analytic or quadrature signal $X(t)$

$$X(t) = x(t) + i\,\tilde{x}(t), \tag{3.34}$$

that can also be represented in a polar form as

$$X(t) = A(t)\, e^{i\,\theta(t)}, \tag{3.35}$$

where $A(t)$ is the instantaneous amplitude of the analytic signal and is given by

$$A(t) = \left[x^2(t) + \tilde{x}^2(t)\right]^{\frac{1}{2}}, \tag{3.36}$$

and $\theta(t)$ is the instantaneous phase of the analytic signal and is defined by

$$\theta(t) = \arctan\left(\frac{\tilde{x}(t)}{x(t)}\right). \tag{3.37}$$

For numerical implementation, a four quadrant arctangent function has to be used in Eq. (3.37) to take into account the sign of both $x(t)$ and $\tilde{x}(t)$ and place $\theta(t)$ in the correct quadrant. This results in angles between $-\pi$ and π which correspond to a complete rotation of the measurement tool. The instantaneous phase of the magnetometer measurement obtained by Eq. (3.37) is also depicted in Fig. 3.3.

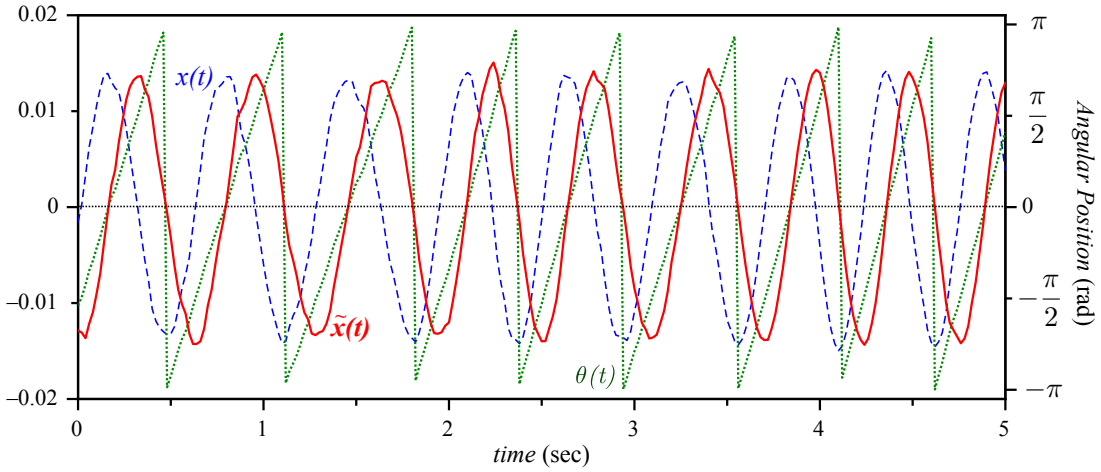

FIGURE 3.3: Magnetometer measurement $x(t)$, its Hilbert projection $\tilde{x}(t)$ and instantaneous phase $\theta(t)$.

The instantaneous frequency of the magnetometer record channel, $x(t)$, using its analytic expression is then defined as

$$\omega(t) = \dot{\theta}(t) = \frac{d\theta}{dt}, \tag{3.38}$$

where $\omega(t)$ stands for the instantaneous frequency. Note that for any arbitrary signal, there is a unique single value of the instantaneous phase at any given time and its dimension is radian per second.

The instantaneous phase in Eq. (3.38) has to be unwrapped prior to the differentiation to obtain a continuous phase. The unwrapping is performed by adding 2π at the end of every full cycle to provide a smooth and increasing phase function.

Another representation of the instantaneous frequency which avoids phase unwrapping is given by [49]

$$\omega(t) = \frac{x(t)\,\dot{\tilde{x}}(t) - \dot{x}(t)\,\tilde{x}(t)}{A^2(t)}, \tag{3.39}$$

where

$$\dot{\tilde{x}}(t) = \frac{1}{\pi}\mathrm{P}\int_{-\infty}^{+\infty} \frac{\dot{x}(\tau)}{t-\tau}\, d\tau. \tag{3.40}$$

The discrete-time expression of the instantaneous frequency can be written as

$$\omega_k = \frac{\theta_{k+1} - \theta_k}{T}. \tag{3.41}$$

where T stands for the measurement time step. Substituting Eq. (3.37) in Eq. (3.41) results in

$$\omega_k = \frac{1}{T}\left[\arctan\left(\frac{\tilde{x}_{k+1}}{x_{k+1}}\right) - \arctan\left(\frac{\tilde{x}_k}{x_k}\right)\right]. \tag{3.42}$$

Simplifying Eq. (3.42) provides the discrete-time expression of the instantaneous frequency obtained using Hilbert transform as

$$\omega_k = \frac{1}{T}\arctan\left[\frac{x_k\,\tilde{x}_{k+1} - \tilde{x}_k\,x_{k+1}}{x_k\,x_{k+1} + \tilde{x}_k\,\tilde{x}_{k+1}}\right]. \tag{3.43}$$

3.4 Numerical Results

The data analysed in this section have been recorded downhole with the Isub [31] while drilling a production well for oil. The Isub is a short autonomous instrumented downhole tool which is equipped with multiple sensors (accelerometers, strain gauges, and magnetometer), a complete data acquisition line, a microprocessor, memory chips and batteries and can be located at any place within the bottom-hole assembly (BHA). The measurement scanning rate can range between 20 and 250 Hz and the memories can hold up to 200-300 hours of recordings. Note that the results presented in this section are obtained by implementing the extended Kalman filter and instantaneous frequency estimation algorithms in Matlab.

An example of the recorded acceleration of centripetal and tangential accelerometers during a new connection over a 200 seconds time interval is illustrated in Fig. 3.4. When a new pipe is added to the drillstring, the BHA comes to a complete halt for a few minutes. Although the measurement tool is not rotating during a connection, the average acceleration of each channel might be non-zero due to the existence of either sensor bias or the gravity field (inclined borehole) or a combination of the two (Eq. (3.29)).

Numerical inferences about each sensor bias and noise statistical properties are made from the data recorded during a connection and are updated at every connection

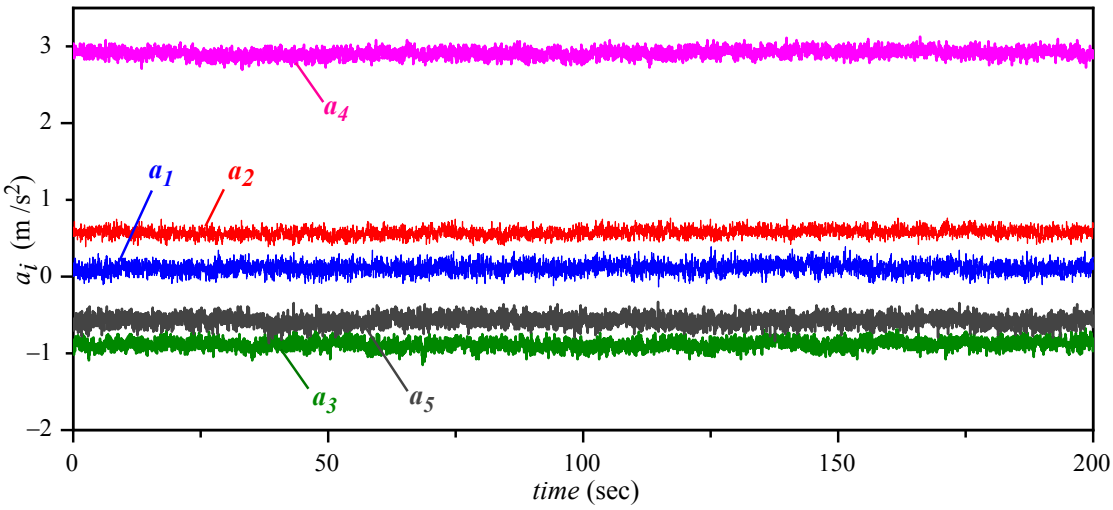

FIGURE 3.4: Centripetal and tangential accelerometer measurements recorded during a connection.

as both bias and noise might deviate due to the unforeseen variations in downhole conditions (temperature in particular).

The histogram of the centripetal acceleration a_4 recorded during the connection is displayed in Fig. 3.5. The figure supports the assumption of a Gaussian distribution for the sensor noise (which is also provided by the sensor manufacturer (see the accelerometer data-sheet [50]) and is essential prior to use a Kalman filter). The figure also shows the corresponding Gaussian distribution fit over the histogram along with its estimated distribution parameters i.e. mean and standard deviation. The procedure is eventually performed for every measurement channel at every connection to provide necessary information of the measurement noise covariance matrix for the extended Kalman filter model.

Also the assumption that measurement errors are uncorrelated over time (Eq. (3.7)) is supported by experimental data as it is illustrated in the autocorrelation function for recordings from sensor a_5 Fig. 3.6 (a) and the cross-correlation function between the recordings of the centripetal accelerometer a_3 and the tangential accelerometer a_5 Fig. 3.6 (b). Note however, that in the presence of correlation in either process noise or measurement noise, a modified Kalman filter can be used to deal with the coloured process noise and measurement noise [43].

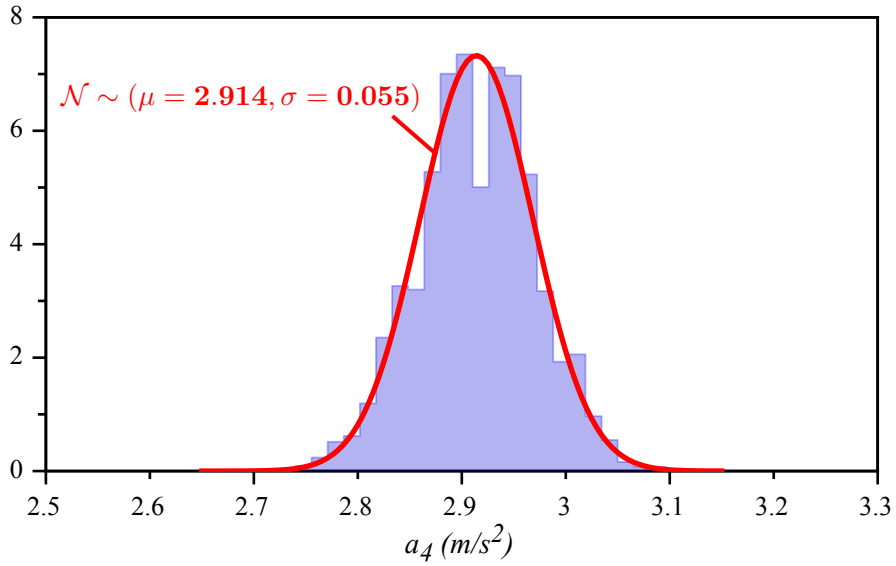

FIGURE 3.5: Histogram of the recorded acceleration during a connection.

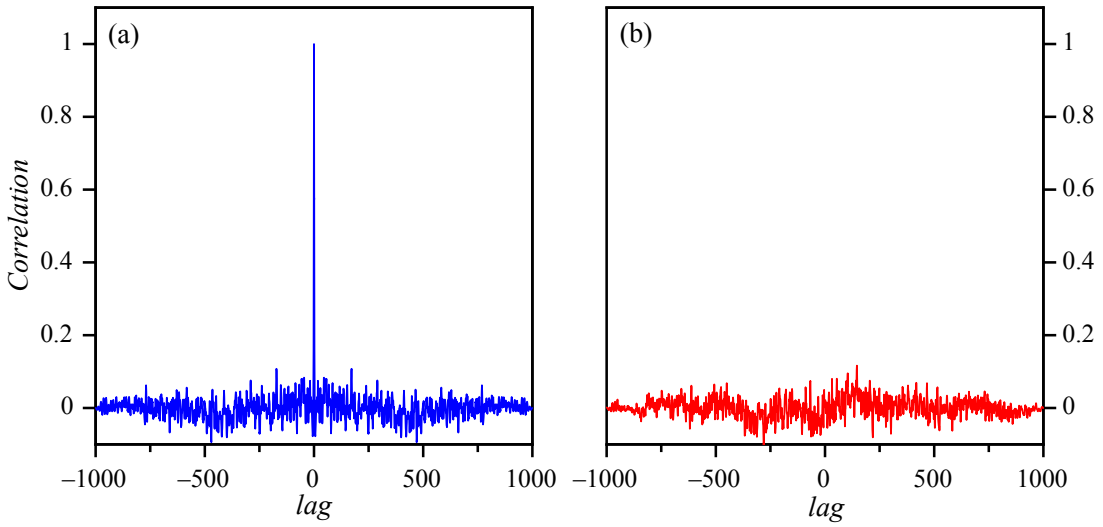

FIGURE 3.6: (a) Autocorrelation of the measured acceleration a_5 during a connection. (b) Cross-correlation between measured acceleration from centripetal a_3 and tangential a_5 accelerometers during a connection.

The parameters related to the tool configuration, r, T; the sensor properties (obtained from the manufacturer data-sheet [50]), σ_a; the dynamic characteristic of the system, ω_*, f_*; the estimated jerk standard deviation, $\sigma_{\dot{\omega}}$, and the bias error $\beta_{\hat{\omega}^2}$, $\beta_{\hat{\dot{\omega}}}$ (estimated at the connection preceding the analysed data set) are summarised in Table 3.1 .

Parameter	Value
T	0.02 s
r	91 mm
σ_a	0.055 m $/s^2$
$\sigma_{\ddot{\omega}}$	39 rad $/s^3$
ω_*	21 rad /s
f_*	0.6 Hz
$\beta_{\hat{\omega}^2}$	-7.5 (rad /s)^2
$\beta_{\hat{\dot{\omega}}}$	6.6 rad /s^2

TABLE 3.1: Numerical values of the EKF model parameters.

An example of the measured radial and tangential accelerations over a 20 seconds time interval while drilling is well illustrated in Fig. 3.7. The centripetal accelerometer, as shown, records larger variation.

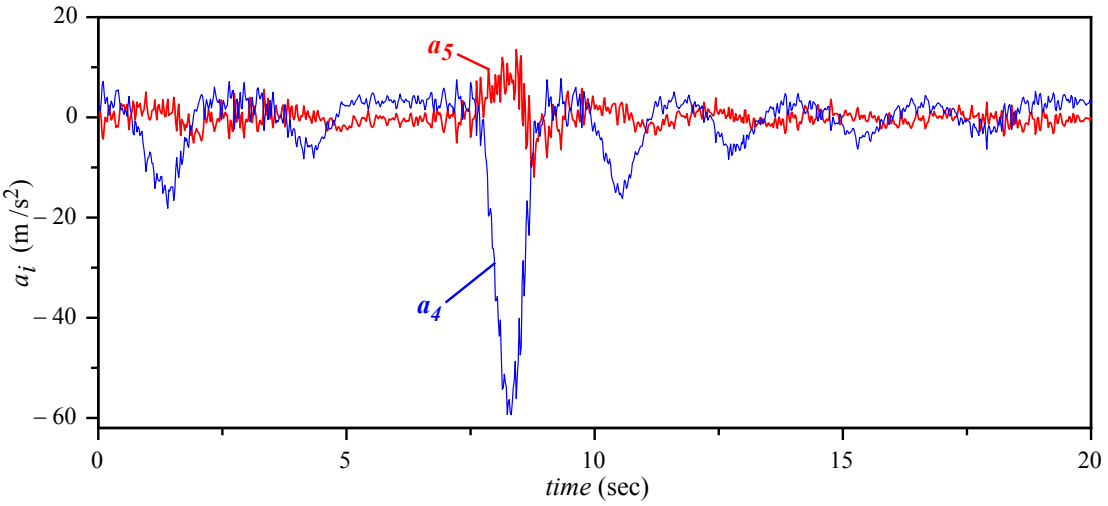

FIGURE 3.7: Centripetal and tangential accelerometer measurements.

3.4.1 Estimation using EKF Model

The angular velocity, ω, estimated with three different methods is shown in Fig. 3.8. The plot labelled "Method 1" is simply the square root of ω^2 determined by Eq. (2.10). It is observed that this estimation provides only information regarding the absolute value of the angular velocity and becomes poor whenever the angular velocity ap-

proaches zero.

The plot labelled "Method 2" in Fig. 3.8 involves performing the time integration of the angular acceleration, $\dot{\omega}$, which is obtained by Eq. (2.11) i.e.

$$\omega_2(t) = \omega(t_0) + \int_{t_0}^{t} \dot{\omega}(u)\, du. \tag{3.44}$$

The main problem associated with this method is the inevitable drift (see Fig. 3.8 "Method 2") caused by any error in the angular acceleration measurement being accumulated during the integration process, and as a result, suffers lack of precision over long recording period.

The estimation of the angular velocity using the extended Kalman filter model presented in sec. 3.2.2 is shown in Fig. 3.8 by the plot labelled "Method 3". The drilling operation is performed at the depth of 3474 m with constant angular velocity of 45 RPM on surface and average weight on bit of 85.5 kN.

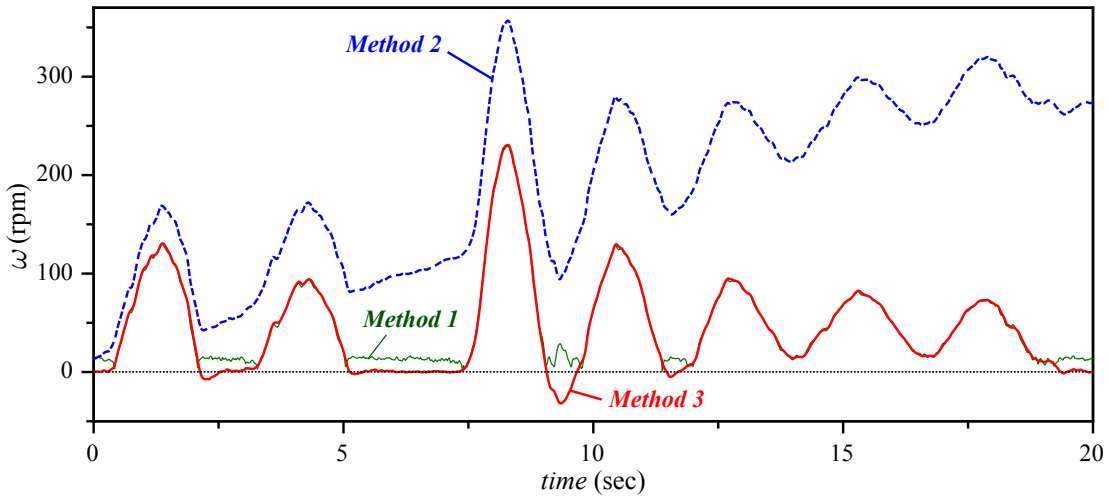

FIGURE 3.8: Estimated angular velocity of the measurement tool with three different methods. The imposed angular velocity on surface is 45 RPM.

The results show that the Kalman model is not only cancelling out the drift caused by the error accumulation intrinsic to the integration process ("Method 2"), but it is also capable of identifying events of backward rotation where angular velocity is negative. Besides, unlike "Method 1", Kalman model provides more precise results for low angular velocities.

The effect of uncertainties associated to the dominant frequency f_*, and amplitude of oscillation, ω_*, on the covariance matrix of the process noise is investigated by

considering different values of $\sigma_{\ddot{\omega}}$ (see Eq. (3.27)). Table. 3.2 shows the first five undamped torsional natural frequencies of the drillstring predicted by finite element model [51].

Torsinal Vibration Mode	Natural Freq (f_*) Hz
1	0.6
2	3.9
3	7.6
4	10.5
5	13.3

TABLE 3.2: Example of the natural frequencies of a drill string associated to the first five modes of torsional vibrations.

The results shown in Fig. 3.9 indicate that the Kalman filter model provides a robust estimate of the angular velocity for a relatively wide range of $\sigma_{\ddot{\omega}}$.

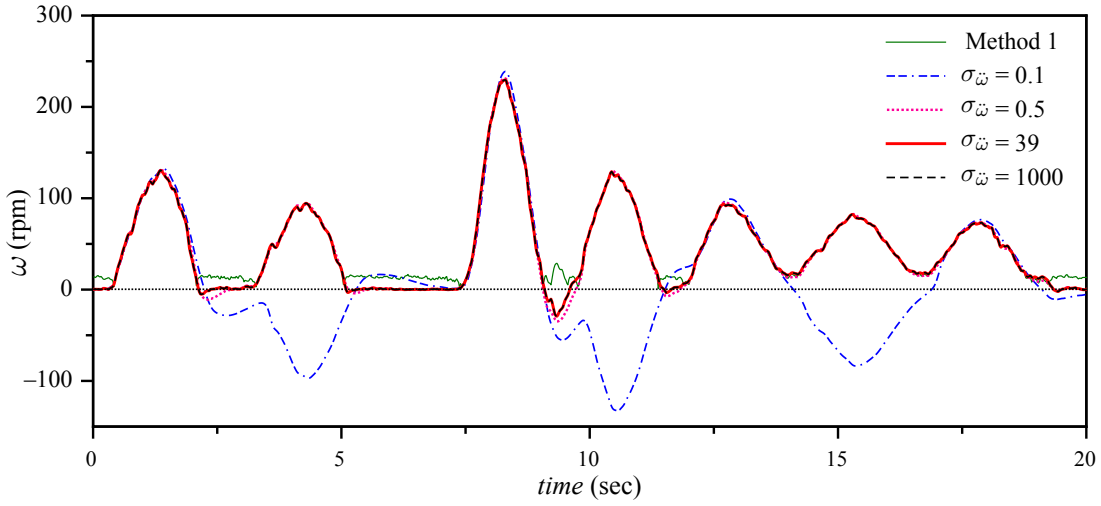

FIGURE 3.9: Sensitivity of the estimated angular velocity using extended Kalman filter model to the angular jerk variance.

The occurrence of backward rotation can also be confirmed using magnetometer measurement channel. The estimation of the angular velocity using extended Kalman filter model accompanied by the magnetometer record of the same time period is illustrated in Fig. 3.10. Magnetometer shows that at the onset and end of the backward

rotation, the full bit rotation is not complete and thus, the rotation has changed direction. Figure 3.10 (b) indicates that the amplitude of the induced magnetic field caused by the rotation of the drill rod is velocity dependant, and thus, the variation in the magnetometer measurement amplitude is noticeably larger due to the existence of the stick-slip vibration.

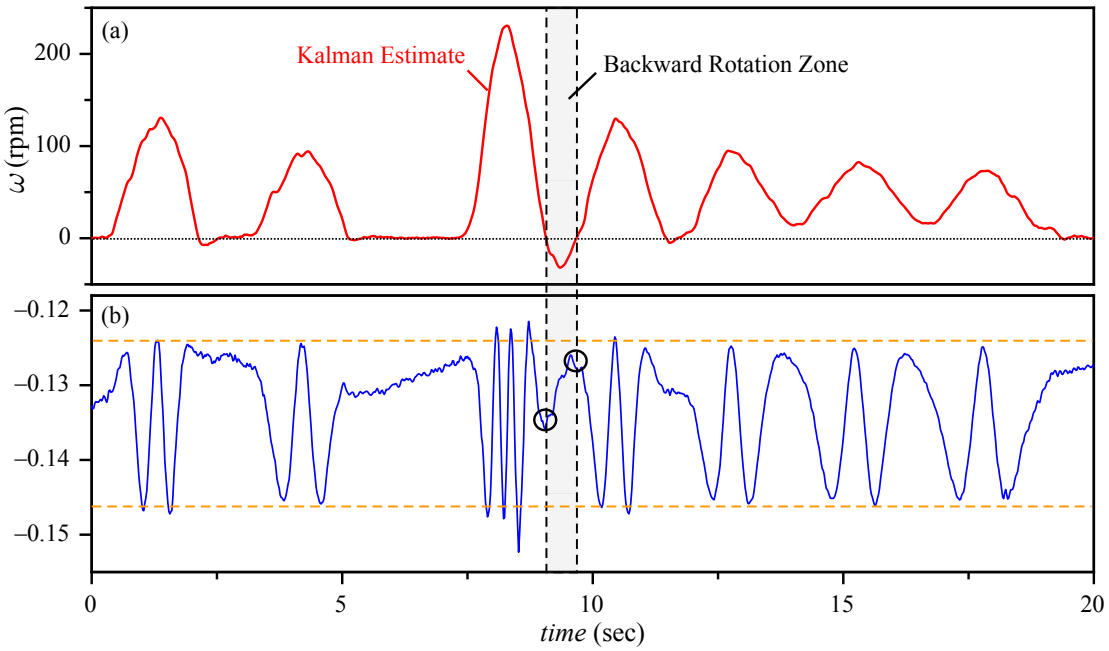

FIGURE 3.10: Confirmation of the existence of backward rotation using magnetometer measurement. (a) Angular velocity estimated by extended Kalman filter model (b) Magnetometer recording.

Another example of the estimated angular velocity, ω, using the three methods mentioned earlier, over a 120 seconds time interval, along with the accelerometer and magnetometer measurements is depicted in Fig. 3.11. The Kalman filter estimation indicates the occurrence of slight backward rotations right after every slip phases and before the onset of the stick phases (see Fig. 3.11 (b)).

The final example of this section shows the estimated angular velocity, ω, over a longer time interval (440 seconds of stick-slip vibration), along with the accelerometer and magnetometer measurements. As shown in Fig. 3.12, the Kalman estimate ("Method 3") does not drift with time even for longer period of measured signals.

A closer look at the results shown in Fig. 3.12 is depicted in 3.13, confirms the existence of another significant backward rotation being validated by the magnetometer

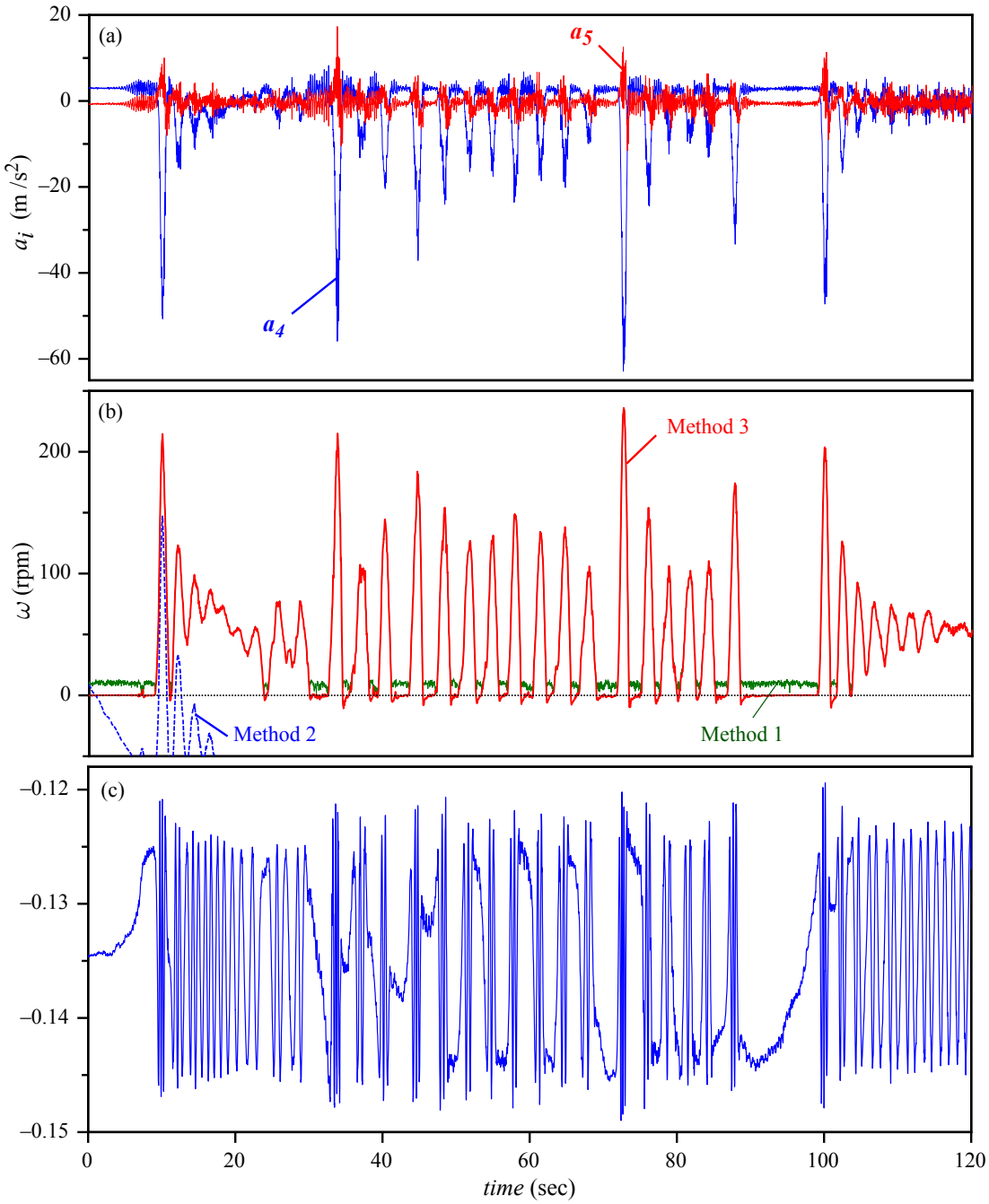

FIGURE 3.11: (a) Centripetal and tangential accelerometer measurements (b) Estimated angular velocity with the three different methods (c) Magnetometer measurement.

record as well.

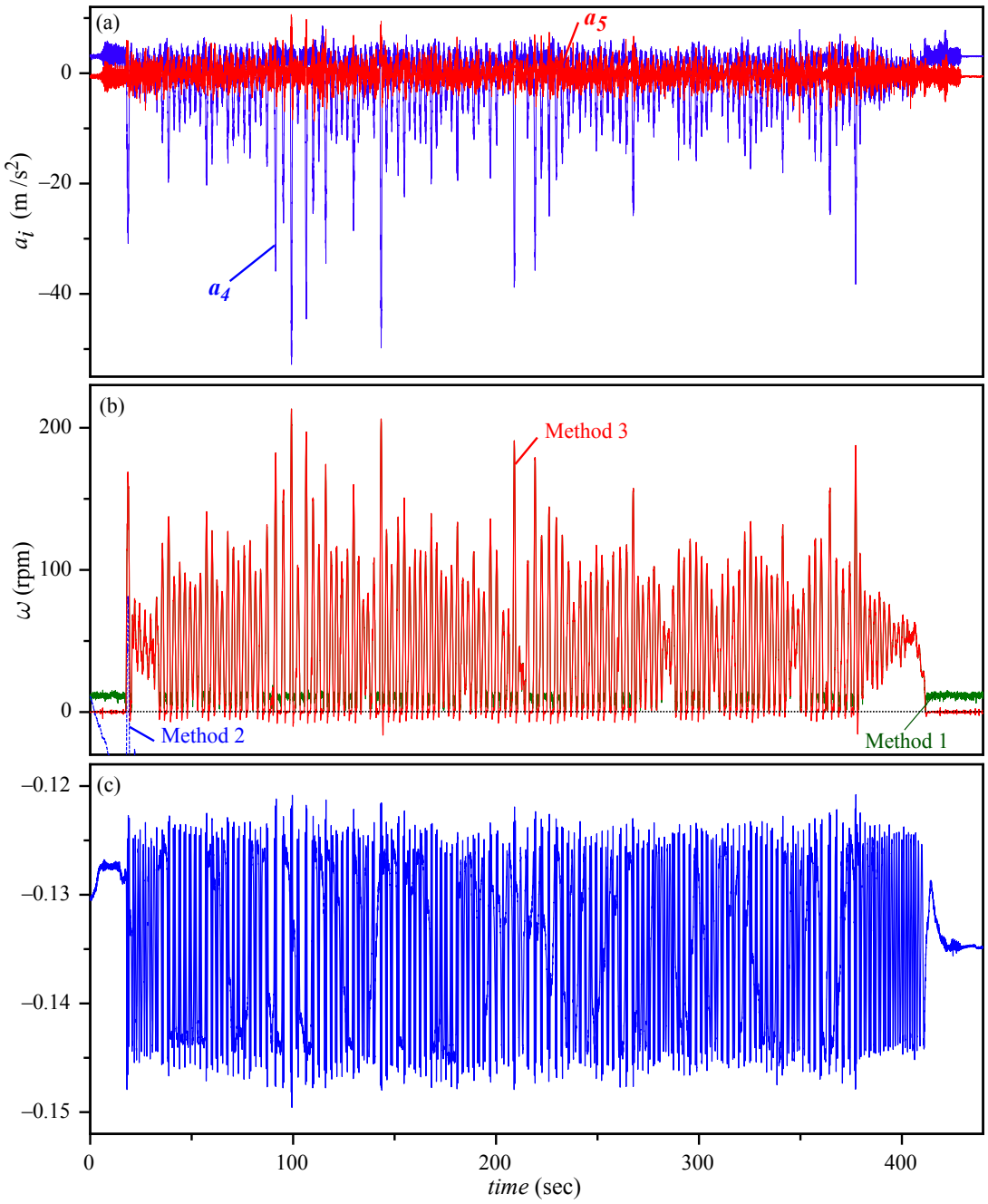

FIGURE 3.12: (a) Centripetal and tangential accelerometer measurements (b) Estimated angular velocity of the measurement tool with three different methods (c) Magnetometer measurement.

3.4.2 Estimation using Hilbert Transform

The estimated angular velocity of the measurement tool using magnetometer measurement and Eq. (3.43) for the example provided earlier in sec. 3.4.1 (see Fig. 3.8) is

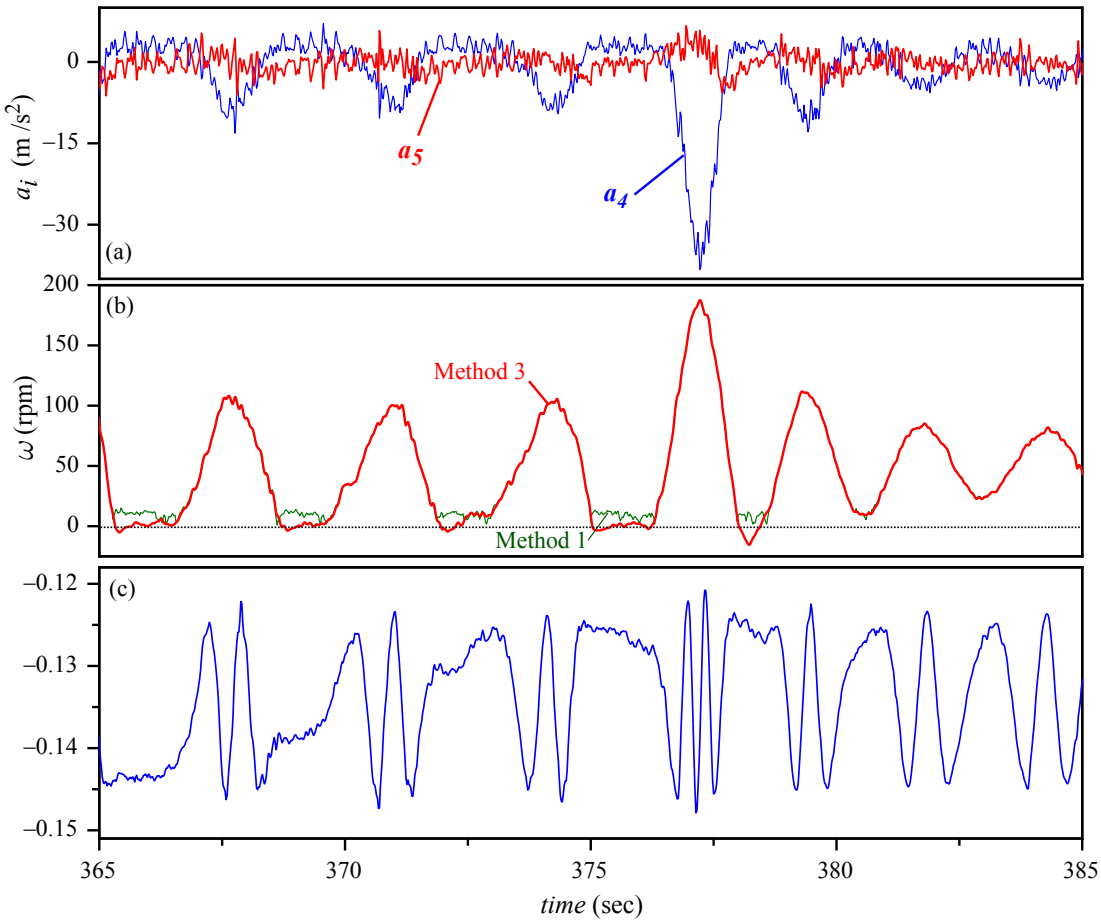

FIGURE 3.13: (a) Centripetal and tangential accelerometer measurements (b) Estimated angular velocity o with three different methods (c) Magnetometer measurement.

illustrated in Fig. 3.14. The high frequency oscillations of the angular velocity signal are an artefact caused by the differentiation of the instantaneous phase and do not have any physical meaning since even small level of added noise of the magnetometer recorded signal excites the higher frequencies of the instantaneous phase signal. A moving average filter is thus applied to provide a smoother signal.

The results shown in Fig. 3.14 indicates that the estimate of ω using magnetometer measurement at higher angular velocities is relatively good. However,the precision is quite low as the angular velocity approaches zero. Furthermore, the method is also incapable of capturing events of backward rotation.

Another example considering only strictly positive angular velocity is depicted in Fig. 3.15. The results of the two methods match quite well apart from the the high frequency oscillation (magnetometer measurement) caused by the derivative operation.

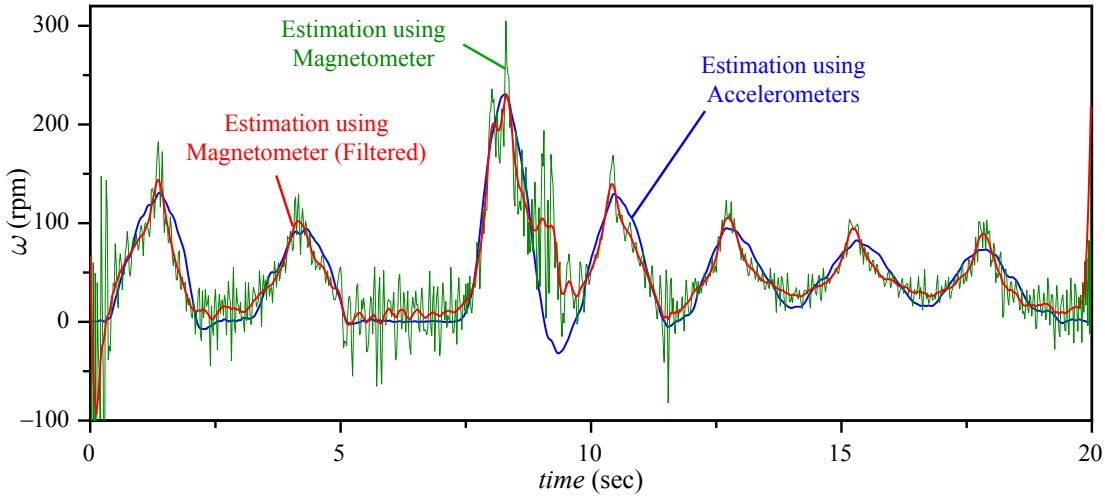

FIGURE 3.14: Comparison between the angular velocity estimated using accelerometer and magnetometer measurements.

Similar to the previous example, a moving average filter is performed to provide a smoother estimate.

3.5 Discussion

The first and most important advantage of using accelerometer and Kalman filters to estimate the angular velocity rather than the magnetometer is that the former can be implemented in real-time while the latter uses batch processing. Estimating the new state vector requires just the previous state estimate and the information about the history of the signal is being preserved through Kalman gain, which is updated at each estimate. But Hilbert transform needs to be performed over a window long enough with respect to the main oscillation period. Therefore, the Kalman filter model performs much faster in practice compare to the Hilbert Transform.

Also as illustrated in Fig. 3.14, the magnetometer provides poor estimation when the angular velocity approaches zero and is also unable to detect the negative angular velocities in case of backward rotation occurrence. It is simply explained by the nature of the magnetometer that measures the projection of the magnetic field intensity along its sensitivity axis. As the cosine function is unable to retain the information about the rotation direction ($\cos(-\theta) = \cos(\theta)$), thus, a single axis magnetometer is unable to identify the change in the rotation direction within the Hilbert transform. An additional

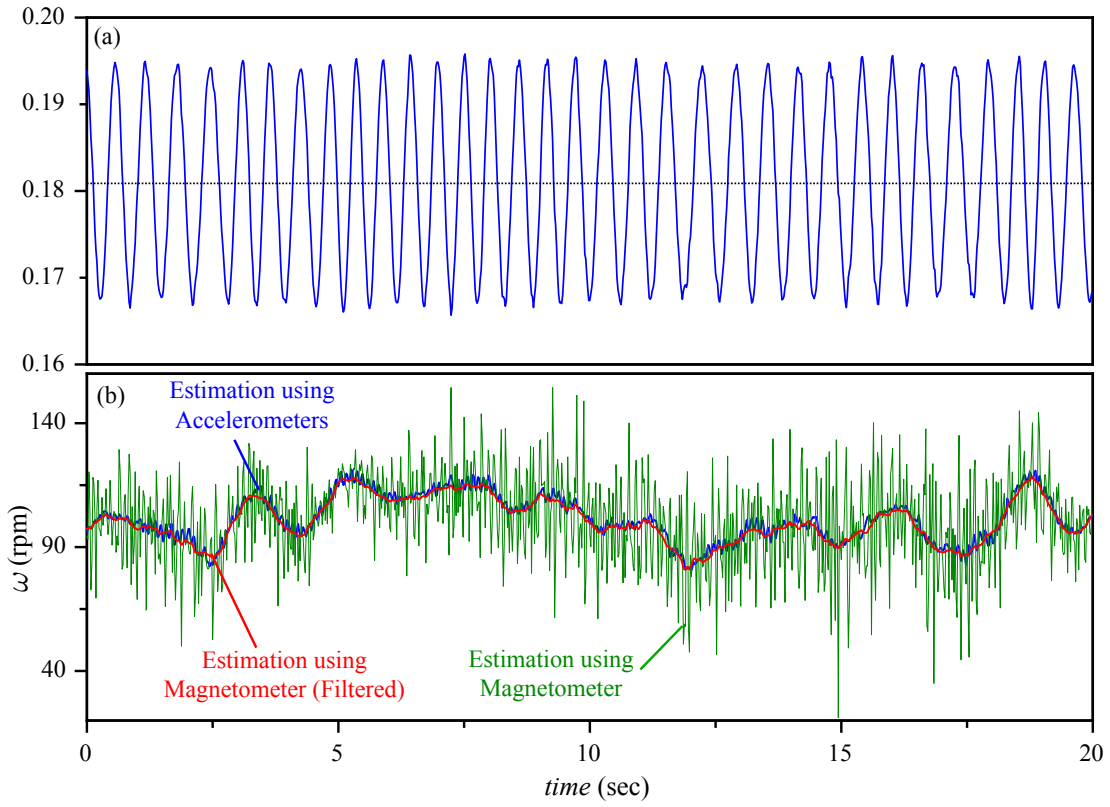

FIGURE 3.15: Comparison between the angular velocity estimated using accelerometer and magnetometer measurements (a) Magnetometer recording (b) Angular velocity estimated with the two methods.

axis of measurement is necessary to overcome the problem. Remember, however, that the amplitude variation of the magnetometer channel, as mentioned earlier, may provide information regarding the occurrence of backward rotation.

Despite these limitations, the simulations show that for large and positive angular velocities, the magnetometer estimate is quite satisfactory, and could be considered as an alternative sensor in some application. Fig. 3.15 illustrate the magnetic sensor measurement and the angular velocity of the Isub estimated separately by using the accelerometer and magnetometer measurements respectively.

Chapter 4

Conclusions

4.1 Main Results and Practical Implications

The first part of the proposed research aims at developing a new algorithm to detect the existence and severity of the down-hole torsional vibrations while drilling, in particular the occurrence of backward rotation. The importance of the drilling vibrations was discussed in detail and the related works were investigated thoroughly. It was well understood from the literature that downhole vibrations while drilling are inevitable due to the intrinsic properties of the drillstring (slenderness and low compliance) and also the nature of the bit-rock and drillsting-wellbore interactions. The three main downhole self-excited vibration modes (axial, torsional and lateral) as well as their detrimental effects on the BHA and the bit were discussed in details motivating the necessity for the methods to detect and mitigate their occurrence and reduce their associated damages to the drilling assembly in real-time.

A new technique to estimate the angular velocity of the drill bit as a measure to monitor the state of the torsional vibrations was presented in this part. The method is based on the extended Kalman filters and uses centripetal and tangential accelerometer measurements recorded downhole by means of an instrumented sub. The mathematical model for the dynamic system was formulated first using laws of kinematics and the knowledge about the configuration of the accelerometers mounted on the measurement sub.

The state-space and extended Kalman filter model were extracted and the angular velocity and acceleration of the bit were introduced as the state variables of the kalman

model. The time varying bias and noise associated to each sensor were considered in the model and updated using the accelerometer measurements during the connection. An alternative formulation of the tool kinematics was also presented for particular interests on studying the whirl motion.

A method based on the frequency demodulation of the measure of the intensity of the magnetic field in the vicinity of the instrumented sub was presented afterwards. The Hilbert transform was used whithin the proposed algorithm to determine the instantaneous frequency of the uniaxial magnetometer sensor as a measure of the angular velocity of the instrumented sub.

The estimation of the bit angular velocity by means of the proposed methods using downhole field measurements were eventually demonstrated. The EKF method was proven to be capable of clearly identifying events of stick as well as occurrence of backward rotations followed by the confirmation of the magnetometer sensor. Several simulations using measurements with different length were carried out and the results were compared to the conventional methods exist in the literature. The EKF model estimate was also observed to be consistent by increasing the signal length.

The computational advantage of the algorithms based on the extended Kalman filters are quite marginal since the method does not require the entire estimates history to predict the next state of the dynamic system but relies only on the last estimate and Kalman gain. Thereby, it is very memory efficient and well-suited to carry out fast estimation and as a result, can be performed in real-time. The proposed algorithm can be eventually implemented using embedded electronic mounted downhole, allowing to transmit only precise diagnosis on the nature but also severity of the torsional vibration to surface while drilling a wellbore.

The angular velocity estimation using the magnetometer measurement and Hilbert transform was observed to match quite well with the results obtained from EKF model for strictly positive angular velocities. However, the method was perceived to be unable to detect the events of stick phases as well as the occurrences of backward rotations. Though, the magnetometer measurement carries information about the occurrence of backward rotation.

4.2 Note on the Minimum Number of Sensors

The compact memory space and also limited energy powered by the battery in the downhole instrumented subs necessitate the minimisation of the number of various sensors mounted on the tool. Thus, it is worth to investigate the minimum number of required accelerometers to estimate the angular velocity of the bit. Alternative formulation of the Isub kinematic (Eq. (2.14)) shows that the square angular velocity can also be obtained by

$$\omega^2(t) = -\frac{1}{2\,r}\left[a_2(t) + a_4(t)\right] = -\frac{1}{2\,r}\left[a_1(t) + a_3(t)\right]. \tag{4.1}$$

Eqs (2.11) and (4.1) indicate that only two centripetal and one tangential accelerometers (sensors correspond to $\mathbf{n}_2$, $\mathbf{n}_4$ and $\mathbf{n}_5$ for the configuration given by Fig. 2.1) are necessary and sufficient to build up the measurement vector of the EKF model and the corresponding bias vector information, yielding the estimation of the tool angular velocity. However, estimation of the bit center trajectory requires all four centripetal and one tangential accelerometers.

4.3 Future Works on the Whirl Trajectory

The Kalman filter model can be extended to estimate the trajectory of measurement tool center with respect to the borehole centre line by using the measurements of the acceleration of the tool center in x and y directions obtained by Eqs. (2.12) and (2.13). The description of the Kalman model as well as the state-space model is provided in appendix A.

The model involves the double integration of the accelerations, $\hat{\ddot{R}}_X$ and $\hat{\ddot{R}}_Y$, to obtain the position of the bit center, R_X and R_Y, and thus, suffers lack of precision due to inevitable drift caused by the error in accelerometer measurements accumulated in the integration process. Therefore, additional measurement is required in order to correct the estimate for the drift. One possible measurement is the bending moment (measured at a certain distance from the plane in which the accelerometers are located), as the bending moment is related to the deviation of the tool centre line from the BHA centre line.

Alternative formulation of the instrumented sub kinematics is also a solution to obtain information about the whirl vibration. As it was briefly discussed in sec. 2.3,

simplifying the whirl motion into well-understood scenarios along with the frequency an amplitude demodulation techniques may aim at identifying the whirl parameters i.e. whirl radius, R and whirl angular velocity, Ω over time.

Considering the whirl velocity and radius to be constant over the time interval, similar to the scenario presented in sec. 2.3, the squared difference of the acceleration recorded by the sensors correspond to $\mathbf{n}_1$ and $\mathbf{n}_2$ (for the configuration given by Fig. 2.1) is obtained by

$$(a_1 - a_2)^2 = \left(R\,\Omega^2\right)^2 \Big[1 - \sin\left[2\,(\Omega - \omega)\,t\right]\Big]. \tag{4.2}$$

As it can be inferred from 4.2, frequency demodulation of the $(a_1 - a_2)^2$ should provide information regarding the frequencies exist in the system, or in other words, $\Omega - \omega$.

Part II

A Novel Tool for Piecewise Linear Segmentation

Chapter 1

Introduction

1.1 Background

Nowadays, numerous drilling data are collected on the rig floor by mud-loggers while drilling for hydrocarbons. Historically, as indicated by the name, the primary activity of mud loggers consisted literally in logging the mud coming out of the well, and in particular, the rock debris (referred as cuttings) carried out by the mud. The original activity of mud-loggers was descriptive (essentially scanning the cutting for traces of hydrocarbons and gas), and although, over the years, additional data, mainly drilling data (forces, velocities), were introduced in the scope of mud logging activities, their activity is still limited to the recording and monitoring of drilling operations. No real effort has been dedicated to the processing and interpretation of data or even the objective documenting of drilling performances.

Commonly, the data are archived in their raw format with no or little processing and are presented in the form of logs (well-logs) simply showing the evolution of the drilling parameters with the borehole depth, often one point per foot drilled (borehole depth can commonly reach several kilometres). Lately, the emergence of downhole drilling data (downhole force, accelerations, velocities) has provided valuable insight on some of the drilling events and responses occurring downhole, but has not drastically modified the way drilling data are handled and presented. Short sections of raw data are only very rarely singled out to analyse particular (often detrimental) events. And thus, despite the wealth of available data, the measure of drilling performances are reduced to average drilling parameters, most often averaged over an entire borehole section (several tens or

hundreds of metres). As much as raw data are practically not manageable on a routine basis, such non-selective contraction of the data tends unfortunately to impoverish the information/conclusions one can draw, yielding often a quite non-objective assessment of performance or comparison between performances.

Over the last decades, there has been some effort in the industry to measure objectively, the drilling performance and possibly optimise it in real-time (Detournay and Defourny, 1992; Fear, 1996 [52]; Dupriest and Koederitz, 2005 [53]; Dupriest, 2006 [54]; Cayeux et . al., 2009 [55]; Eren and Ozbayoglu, 2010 [56]). Most methods rely on drilling rate models that relate the operating parameters (applied axial force and angular velocity) to the resulting drilling rate of advance or rate of penetration. However, the models are applied on the raw data and yield additional log variables computed foot by foot; they are applied irrespective of the relevance of the data, in particular irrespective of whether the drilling response is stationary or not. This is particularly true for the rate of penetration that is currently simply calculated as the derivative of the hook vertical position (position of the hook hoisting the drillstring that is travelling down while drilling). The derivative operator added to the imprecision in the position measurement yields a measure of the rate of penetration that exhibits quite large dispersion in comparison to the operating parameters, in particular the axial force (weight-on-bit), as it is illustrated in Fig. 1.1. Furthermore, drilling rate models are based on bit-rock interface laws that consider a certain level of stationarity as variables are taken averaged over several bit revolutions. The implementation of such models on surface data also assume that the hook (surface) axial velocity is representative of the bit axial velocity (downhole), which however holds true only under conditions of stationarity. In fact, under condition of varying axial load, elongation of the drillstring affect the depth measurements which in turn can affect drastically the estimate of the rate of penetration.

In order to enhance the readability, the quality and the relevance of drilling data, we argue that it is necessary to segment the data. The segmentation is aimed at isolating regions characterised by stationary responses over which models can be implemented with higher level of confidence. Segmentation will reduce the dispersion associated to some of the measurements, eliminate sections of data that are not representative because affected by artefacts of the drilling operations (elongation of the drillstring). Segmentation would also allow more robust and efficient assessment and documentation

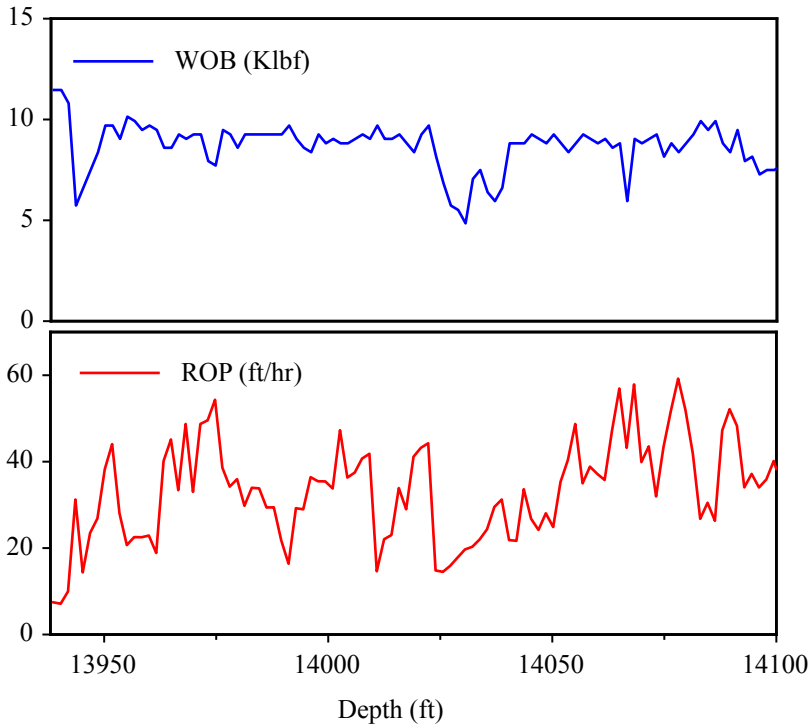

FIGURE 1.1: Example of drilling surface data showing excessive dispersion in the rate of penetration measurement (ROP) in comparison to the axial force measurement.

of performance as well as objective comparison between different drilling performances.

The simplest segmentation one can propose is piece-wise linear. Drilling data consist of various measurements over several days or weeks (up to millions of points per channel) characterised by a wide range of noise intensity and in some instance, non-stationary noise. It is therefore necessary to rely on a fast segmentation method that can handle signal polluted by noise of various intensity and possibly non-stationary. The example shown in Fig. 1.2, illustrates how piece-wise linear segmentation of the hook position yields a far less dispersed estimate of the rate of penetration.

1.2 Literature Review (Piece-wise Linear Segmentation of Time Series)

Time series are increasingly and widely used in various domains such as manufacturing, medicine, finance, engineering, geo-sciences. Along with the development of advanced data acquisition systems and storage technologies, they raise practical issues associated with handling and processing of very large amount of data. It is thus often critical to

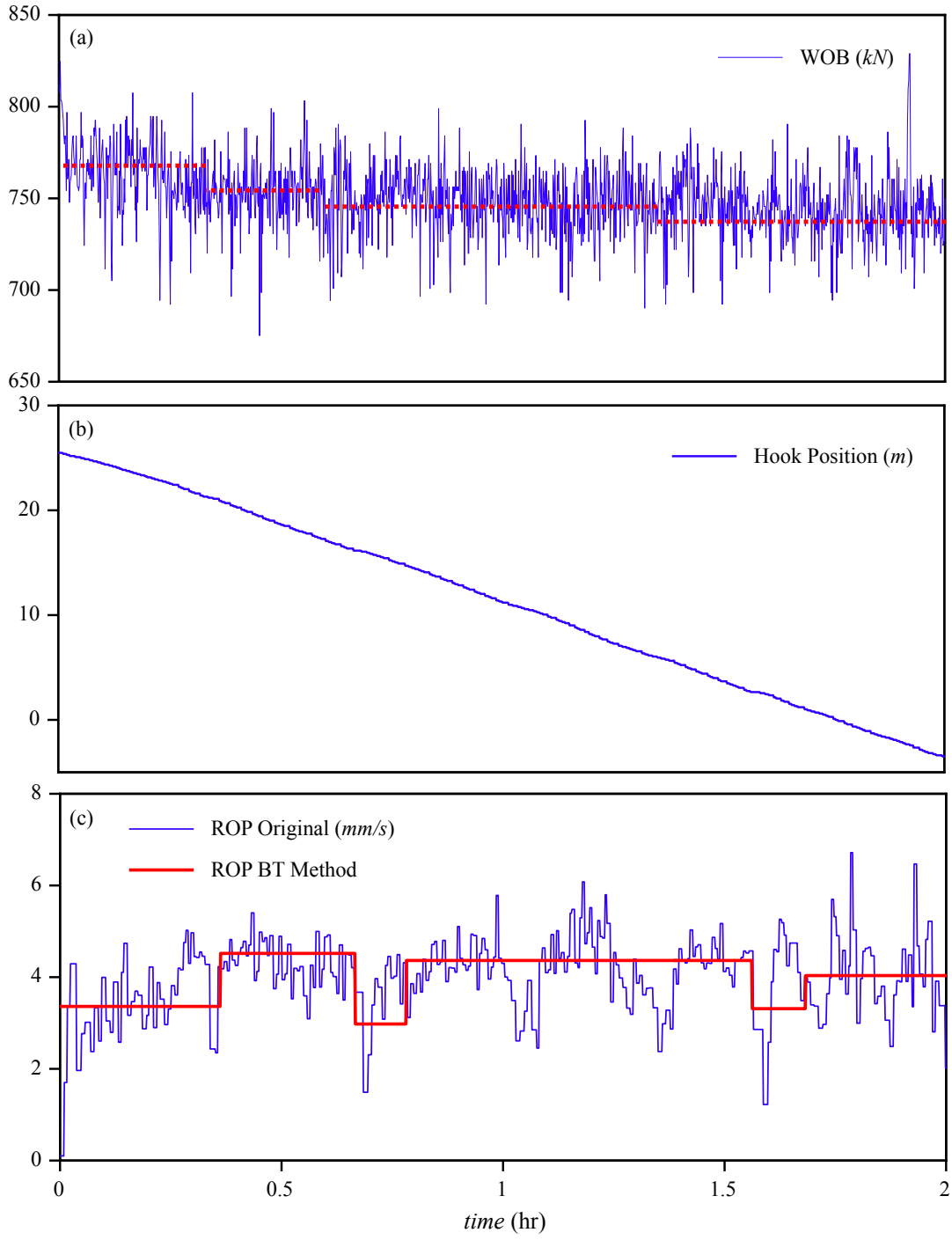

FIGURE 1.2: Surface weight on bit (a). Surface hook position (b). Original rate of penetration compared with an estimate resulting from piecewise linear segmentation of the hook position (c).

reduce the volume of data for efficiency purposes. Also, in a wide range of applications, the underlying trend of the signal carries most of the relevant information; homoge-

neous, qualitative or stationary response are often sought for their relative simplicity. It is therefore often neither efficient nor necessary to archive or analyse the entire time series, but rather deal with approximate representation. Piece-wise linear approximation has raised particular attention over the past few years due to its inherent simplicity.

There is a vast amount of literature dedicated to time series approximation (in particular piece-wise linear approximation) covering broad range of fields such as applied mathematics and statistics (Barry and Hartigan, 1993 [57]; Fearnhead, 2006 [58, 59]; Szusz and Willms, 2010 [60]) signal processing (Lavielle and Lebarbier, 2001 [61]; Mahmoodi and Sharif, 2006 [62]), computer science and data mining (Keogh et al., [63–68]; Liu et al., 2008 [69]) medicine (neurology) (Kaplan et al., 2001 [70]), geosciences (Hawkins, 2000 [71]; Kehagias et. al., 2005 [72]), acoustic and vibrations engineering, cartography (Douglas and Peucker, 1973 [73]). Methods are found under various names such as curve fitting, signal segmentation or multiple change-point detection; they deal with signals of quite different nature (wells logs, stock-market, heart rate, maps contours, speech data, etc) and are driven by quite different associated goals (model fitting, features or event detection, transient detection). The signal properties (background trend, envelop, noise level, frequency content) and the underlying objective of the approximation are the root causes for the diversity of proposed techniques for segmentation or change-point detection such as maximum likelihood ratio (Appel and Brandt, 1983 [74, 75]; Basseville and Nikiforov, 1993 [76] ; Siegmund and Venkatraman, 1995 [77]; Gustafsson, 1996 [78]), least squares approximation in sliding, shrinking or growing time window (Chu, 1995 [79]; Keogh et. al., 2001 [66]; Keogh et al., 2004 [65]; Lemire 2007 [80]; Liu et. al., 2008 [69]; Fuchs et. al., 2010 [81]), minimisation of cost function within the set of all possible segmentations (Kehagias et. al., 2005), Fourier or wavelet transforms (Chan et. al., 2003 [82]; Tseng et. al., 2009 [83]), Bayesian inferences (Sclove, 1983 [84]; Barry and Hartigan, 1993 [57]; Punskaya et. al., 2002 [85]; Fearnhead, 2005 [86]), "energy" optimisation (Mahmoodi and Sharif [62]). While most of these methods aim at a fast maximum likelihood segmentation and say nothing about the uncertainties, the Bayesian inferences methods (exact curve fitting or combined with Monte Carlo Markov Chain techniques), although more greedy, assess the posteriori distribution of the segmentation model parameters.

Despite the extensive range of applications and methods catalogued as segmentation, only few authors have attempted to review and classify the various techniques

beyond the evident online and offline distinction. Szusz and Willms (2010) [60] provide a historical overview of the work in the field of mathematics. In the very active field of data mining, Keogh et. al., 2001 [66] propose three main categories, namely: sliding window, top-down and bottom-up algorithms. He also conducted an extensive empirical comparison of performances between the three families of algorithms using an example for each method and applying them on several reference signals.

In all of these works, the results are measured against a metric used to construct stopping criteria, the metric is based on (i) an estimation error global and/or per segment (least square or minimax criterion) and (ii) the number of identified segments. The smaller the estimation error and number of segments are, the better the approximation is rated. The criteria used to find a balanced between error and over-fragmentation is often empirical and govern by the data and the overarching goal of the segmentation. Inspired from model selection criteria, some authors attempted to construct a universal criterion such as Bayesian information criterion (BIC) with some success, Kehagias et. al., 2005 [72].

It is also well known that the noise properties (in particular the presence of outliers) can have strong effects on the results of segmentation. The issue is inherent to Bayesian inferences methods (as noise statistical properties are part of the model parameters) and often one of the motivation for such approach. In the field of data mining, this issue is however rarely discussed and the data considered are often characterised by low noise to signal ratio.

In this part of the research, we introduce a novel technique for piece-wise linear segmentation proposed by Denoel et. al, [87], with a particular interest for noise contaminated piece-wise continuous signal such as well logs data (hydro-geology, drilling, geophysical logs). The method relies on the geometrical properties of the signal of residue (absolute difference between the original signal and the current fit). The idea of splitting the signal at the point of maximum deviation is not novel (Shatkay and Zdonik, 1996 [88]), however, we consider here the maximum angular deviation from the overall fit or in other words, the sharpest peak in the residual signal. For this, we introduce a mechanical-mathematical tool dubbed "BBQ Tong" that is used to identify in the residual signal, the sharpest or most triangular peaks which correspond to break-points in the original signal. This intuitive method proves to be quite efficient, the "BBQ Tong" operates as a transform operator acting as a low-pass filter with

appropriate selection of the tool properties.

1.3 Conceptual Description of the Proposed Segmentation Method

Piece-wise linear segmentation in this paper is referred to the approximation of a time series with additive white Gaussian noise of length n, $x = (x_1, x_2, \ldots, x_n)$, by k linear segments ($(1 \leq k \leq (n-1))$). The series is approximated as

$$x_i = f(t_i) + \epsilon_i, \qquad i = 1, \ldots, n, \tag{1.1}$$

where $f(\cdot)$ is the piece-wise linear function to be determined and ϵ_i is a zero-mean white Gaussian noise with standard deviation of σ ($E[\epsilon_i, \epsilon_i] = \sigma^2 \delta_{ij}$ where δ_{ij} is the Kronecker delta function that is, $\delta_{ij} = 1$ if $i = j$, and $\delta_{ij} = 0$ if $i \neq j$, and $E[\cdot]$ stands for the expected value). Note that the word "noise" in this thesis refers to the white Gaussian noise hereafter.

The procedure often reduces to identifying $(k-1)$ break-points located at τ_j $(1 < j < n)$ with the time series simply approximated between two consecutive break-points by function $f(\cdot)$ as

$$f(t_i) = \alpha_m t_i + \beta_m, \qquad \tau_{m-1} \leq t_i \leq \tau_m, \tag{1.2}$$

where α_m and β_m $(1 \leq m \leq k)$ are coefficients representing (i) the linear least square approximation or (ii) the interpolation of the time series over the segment.

The segmentation algorithm presented in this thesis is categorised as a top-down method [65], meaning that knowledge about the entire sequence is required prior to the segmentation. The recursive segmentation process begins by approximating the time series with one linear segment using a linear interpolation between the first and last data point of the time series denoted by "First Fit" in Fig. 1.3 (a). The signal of residuals is then computed as the absolute value of the difference between the time series and the linear fit ("Residual 1") as shown in Fig. 1.3 (b).

A break-point is characterised as a point where the slope of the residual's underlying trend changes from α_1 to α_2 (in another word, where there is a slope discontinuity in the time series). It is thus anticipated that break-points appear as peaks in the signal of residuals. The break-point associated with the maximum slope change from α_{m-1} to

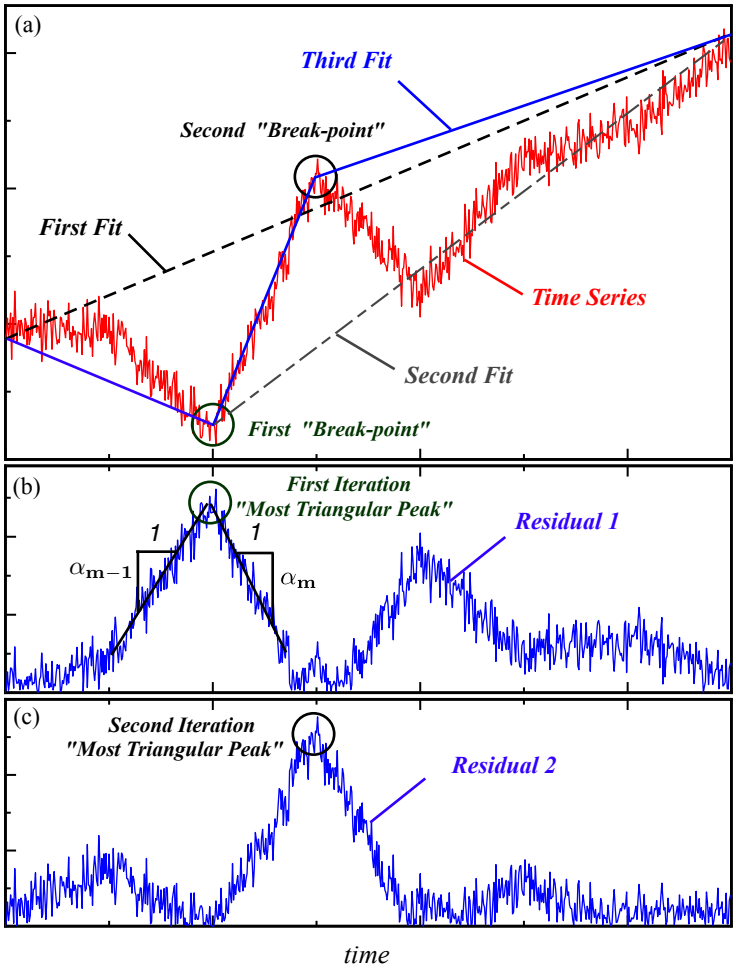

FIGURE 1.3: Time series (a), First signal of residuals (b), Second signal of residuals (c).

α_m corresponds to the "sharpest" peak or in other words, the "most triangular peak" in the residual signal, see Fig. 1.3 (b). The idea developed in this thesis is to substitute the search for break-points in the original time series with the search for the "most triangular peaks" in the signal of residuals.

After the first break-point is identified, the time series is divided into two segments and the new linear fit (labelled "Second Fit" in Fig. 1.3 (a)) is approximated by a linear interpolation between the two successive break-points (first and last point of the time series are assumed as initial break-points). The second signal of residual is then computed as the absolute difference between the time series and the "Second Fit" and the same procedure is applied to find the second "most triangular peak" corresponding to the second break-point, see Fig. 1.3 (c). This iterative procedure is

finally terminated when a user defined stopping criteria (such as maximum number of segments or minimum error) is satisfied.

Note that not necessarily all the break-points appear as triangular peaks in the residual signal at every iteration (a break-point might be sitting on the linear fit). However, we presume that all break-points are to be detected since the linear fit is updated at each iteration.

It is worth mentioning that the reason for using linear interpolation for piece-wise linear approximation in the iterative process is to avoid disjointed segments. However, the final approximation is computed by performing linear least square fit on each segment to provide the minimum segmentation error.

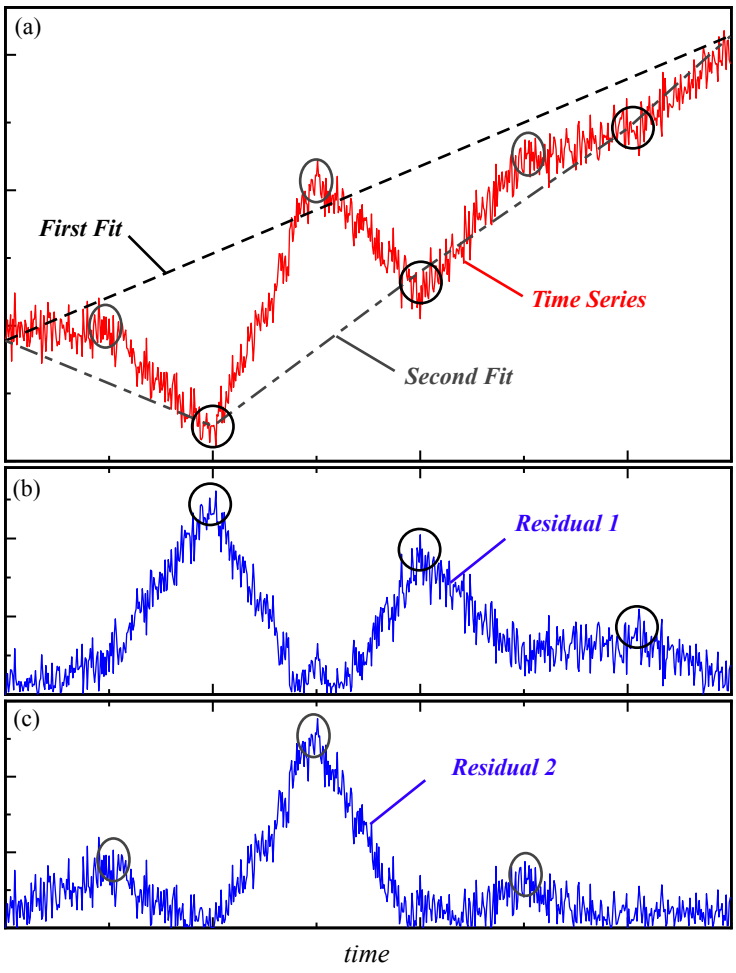

FIGURE 1.4: Time series (a), First signal of residuals (b), Second signal of residuals (c).

Although the procedure is thought as iterative, several break-points can be detected

at each iteration. As it is illustrated in Fig. 1.4, break-points shown by circles in "Residual 1" (see Fig. 1.4 (b)) can be identified at first iteration and break-points displayed by ellipses in "Residual 2" (see Fig. 1.4 (c)) can be detected at second iteration. In this case, only two iterations are necessary and sufficient to identify all the break-points. This is discussed in detail in the next chapter.

1.4 Outline of Part II

Following this introduction, this part is divided into three chapters. The mathematical model associated with the tool ("BBQ Tong") is first introduced in chapter 2 and illustrated with a representative example. A parametric study of the tool respoonse to white Gaussian noise is then carried out yielding practical recommendations for the selection of the tool specifications as a function of the signal and noise properties. The numerical implementation of the segmentation method is described in chapter 3, followed by numerical examples whose results are compared with two segmentation methods proposed in the literature. Finally, in chapter 4, the conclusions are drawn, limitations of the current method and possible future works (in particular the management of outliers) are also thoroughly discussed.

Chapter 2

The BBQ Tong

In this chapter, a mechanical-mathematical tool dubbed "BBQ Tong" and is designed to identify the most triangular peaks throughout a time series signal is introduced. The concept of the "BBQ Tong" along with its governing equation is presented first and its response is illustrated then via a synthetic example. The effect of the noise on the probabilistic response of the tool is investigated thoroughly and the analytical solution followed by sensitivity analysis of the tool to the peakiness of the peaks is eventually performed to conclude guidelines for selecting the proper tool specifications to segment a given time series.

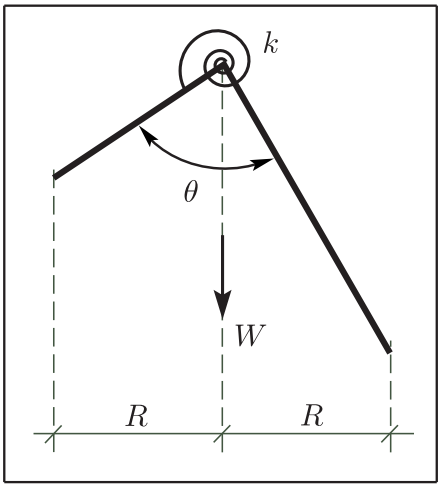

FIGURE 2.1: The "BBQ Tong".

2.1 Concept

The tool, dubbed "BBQ Tong" for its geometrical resemblance to the appliance, is composed of two legs connected together with a hinge, see Fig. 2.1. The legs are adjustable in length under the constraint that their horizontal coverage is constant and equal to R. The tool opening is constrained by a torsional spring of stiffness k located at the hinge where the total weight W of the tool is assumed concentrated. The lower angle, θ, between the left and right legs is referred to as the "hinge angle".

The tool is travelled above the signal with the successive horizontal positions of the hinge given by the time series sequence. At each point of the time series, the equilibrium position of the tool is computed under the constraints that the two legs are in contact with the signal, but neither the hinge nor the legs can penetrate (cross) the signal. As illustrated in Fig. 2.2, the equilibrium position of the tool is governed by the tool mechanical and geometrical properties, but also by the geometrical local features of the signal.

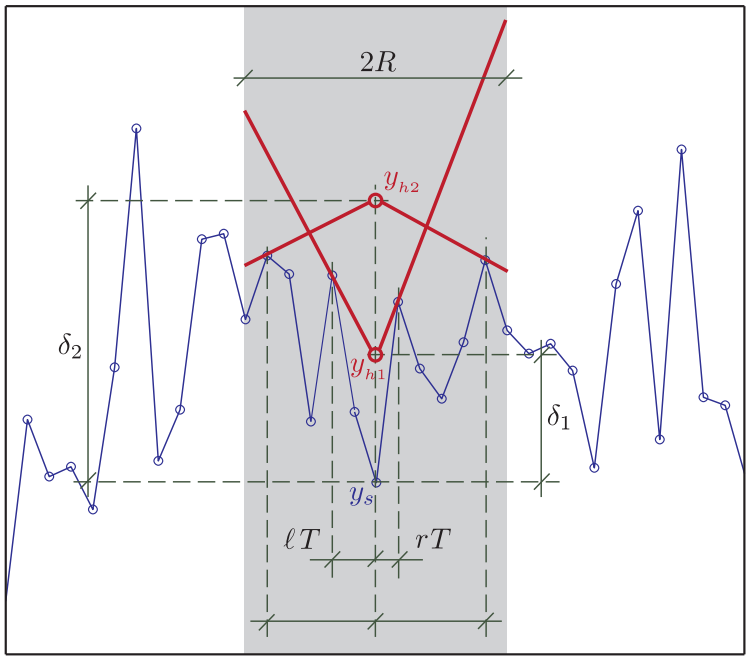

FIGURE 2.2: Two possible equilibrium positions for different stiffnesses of the torsional spring.

The examples shown in Fig. 2.3 illustrate that the equilibrium position of a given tool can yield a hinge angle that carries information relative to the peakiness of the

underlying signal.

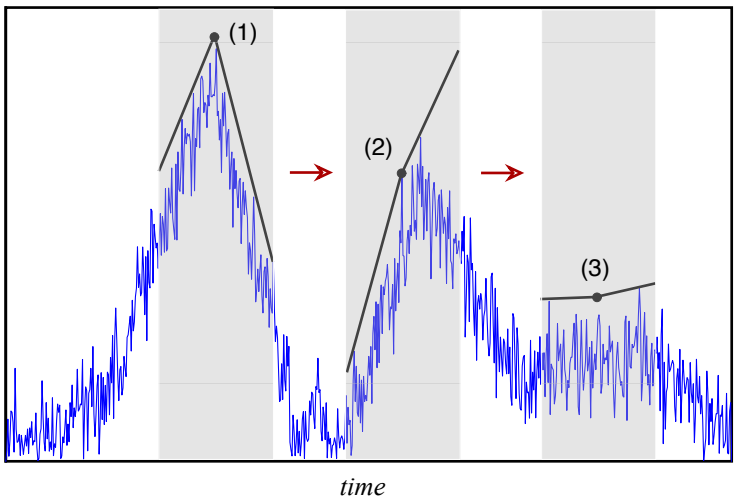

FIGURE 2.3: Three examples of the response of the "BBQ Tong" to the signal of residuals.

2.2 Governing Equation

2.2.1 Geometrical Considerations

On a signal $y = (y_1, \ldots, y_i, \ldots, y_n)$ with time-step $T = t_{i+1} - t_i$, each leg covers N points of the signal with

$$N = \frac{R}{T}. \tag{2.1}$$

At a given point (t_s, y_s), the vertical location of the hinge y_h is defined by

$$y_h = y_s + \delta, \qquad \delta \geq 0, \tag{2.2}$$

and the left (right) leg contacts the signal at point y_ℓ (y_r) at an horizontal distance ℓT (rT) from the hinge, see Fig. 2.4. The condition of non-penetration imposes on r and ℓ that

$$\arctan\left(\frac{\ell T}{y_h - y_\ell}\right) = \max_{i\in[1,N]}\left[\arctan\left(\frac{\ell T}{y_h - y_i}\right)\right], \tag{2.3}$$

$$\arctan\left(\frac{rT}{y_h - y_r}\right) = \max_{j\in[1,N]}\left[\arctan\left(\frac{rT}{y_h - y_j}\right)\right]. \tag{2.4}$$

Note that ℓ, r, i and j are positive integers counted from the hinge position. The hinge angle, θ, then simply reads $\theta = \theta_\ell + \theta_r$ with

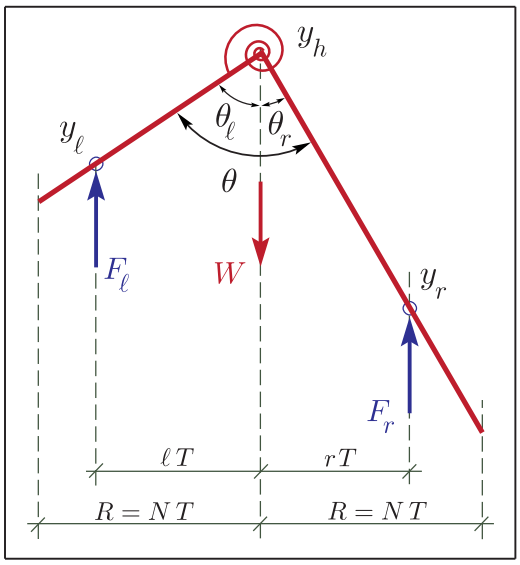

FIGURE 2.4: "BBQ Tong" specifications.

$$\theta_\ell = \arctan\left(\frac{\ell T}{y_h - y_\ell}\right) \quad \text{and} \quad \theta_r = \arctan\left(\frac{rT}{y_h - y_r}\right). \tag{2.5}$$

2.2.2 Equilibrium Equations

For the sake of simplicity, it is assumed that the forces at the contact points between the signal and the legs are vertical. The global force equilibrium of the tool and the balance of moment of each leg around the hinge yield the left, F_ℓ, and right, F_r, contact forces

$$F_\ell = \frac{r}{\ell + r} W, \qquad F_r = \frac{\ell}{\ell + r} W. \tag{2.6}$$

Expressing the moment around the hinge as $M = k\,\theta$ [89], the moment balance of each leg can be written as

$$\kappa\,\theta = \left(\frac{\ell r}{\ell + r}\right), \tag{2.7}$$

where κ represents a dimensionless stiffness defined as

$$\kappa = \frac{k}{W\,T}. \tag{2.8}$$

Note that using Eq. (2.7) the lower (given by $\ell = r = 1$) and upper bounds ($\ell = r = N$) for the hinge angle can be inferred as

$$\theta \in \left[\frac{1}{2\kappa}\,;\,\frac{N}{2\kappa}\right]. \tag{2.9}$$

2.2.3 Solution

The solution in terms of the hinge angle is given by Eq. (2.7) where both sides of the equation are a function of the hinge position δ above the signal. The solution is thus sought in terms of the hinge position δ^* that satisfies Eq. (2.7). For a given δ, the left (referred to as "closing moment") and right hand side ("opening moment") of the equation are computed independently using the non-penetration condition that yields ℓ and r and the elastic law of the spring, $k\theta$. An example of the evolution of the closing and opening dimensionless moments with the hinge position is shown in Fig. 2.5; the equilibrium solution δ^*, is simply the intersection between the two curves that is found numerically using the bisection method.

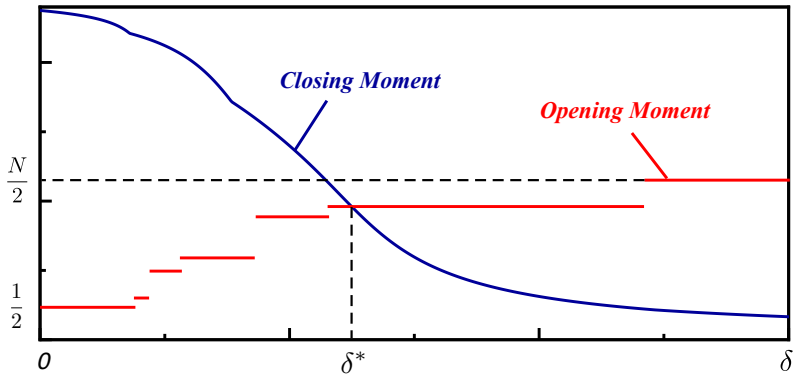

FIGURE 2.5: A schematic example of the evolution of the "closing" and "opening" moments with respect to δ.

As shown in Fig. 2.5, the opening moment is a discrete function as ℓ and r only accept integer values. As a result, there are cases with no intersection between the two curves, corresponding to a situation where a leg is resting on two contact points (aligned with the leg) and the contact force is distributed between the two contacts. In such case, the solution in terms of hinge angle is simply given by the hinge position at the transition between two successive plateau.

In particular, for the case of zero stiffness ($\kappa = 0$), the hinge is located on the signal ($\delta = 0$) and the equilibrium angle is simply given by the condition of non penetration, there is in fact no equilibrium equation for this particular case where the solution is governed only by geometrical constraints.

2.3 A Numerical Example

In this section, the response of the "BBQ Tong" is discussed by considering an example of a piece-wise linear time series corrupted by a white Gaussian noise, see Fig. 2.6. The time series consists of 700 data points with a time step $T = 0.002$ s, and the noise is characterised as Gaussian with zero mean and a standard deviation of 0.05. The results show the evolution of the hinge angle considering different values for the legs length N and spring stiffness κ. Note that the signal is extended on both ends with noise with the same statistical properties as to generate a hinge angle signal with the same length as the original signal.

As it is well illustrated in Fig. 2.6 (c), for very small coverage ($N = 10$), the tool response is highly affected by the noise resulting in large fluctuation in the hinge angle, while for very large coverage ($N = 100$), the response is controlled by the slow varying background trend of the signal. As for the stiffness, we observe that low stiffness ($\kappa = 0.0005$) yields to high dispersion in the hinge angle. With low stiffness, the tool response is strongly dominated by the noise; in the limit case of zero stiffness the hinge does actually sit on the signal. On the other hand, in the case of very large stiffness the hinge stands relatively high above the signal, and the equilibrium angle is quite insensitive to the signal properties, see Fig. 2.6 (b). As a result, the equilibrium angle is quite small and with low dispersion. The response of the tool with intermediate stiffness tend to filter out the effect of the noise with the most triangular peaks in the signal clearly mapped into distinct valleys in the angle sequence. These results outline two possible different strategies to find breakpoints: (i) use a tool with zero stiffness and look for all angles smaller than π (which represents every single peak over the signal) or (ii) use a tool with non-zero stiffness and seek breakpoints iteratively as the minimum in the angle sequence.

The method is highly efficient on a signal with no noise for which a tool with very short legs ($N = 1$) can be used, offering very fast computation time and the ability to capture small segments. However, it is also clear that noise strongly affects the tool response, stressing the need to filter out the effect of noise. "Filtering" capability of the tool is governed by the tool length and/or stiffness; and selection of the tool properties will be governed by the noise properties (variance) and the minimum length of segments we are after. It is thus essential to study the response of the tool to noise. The study is

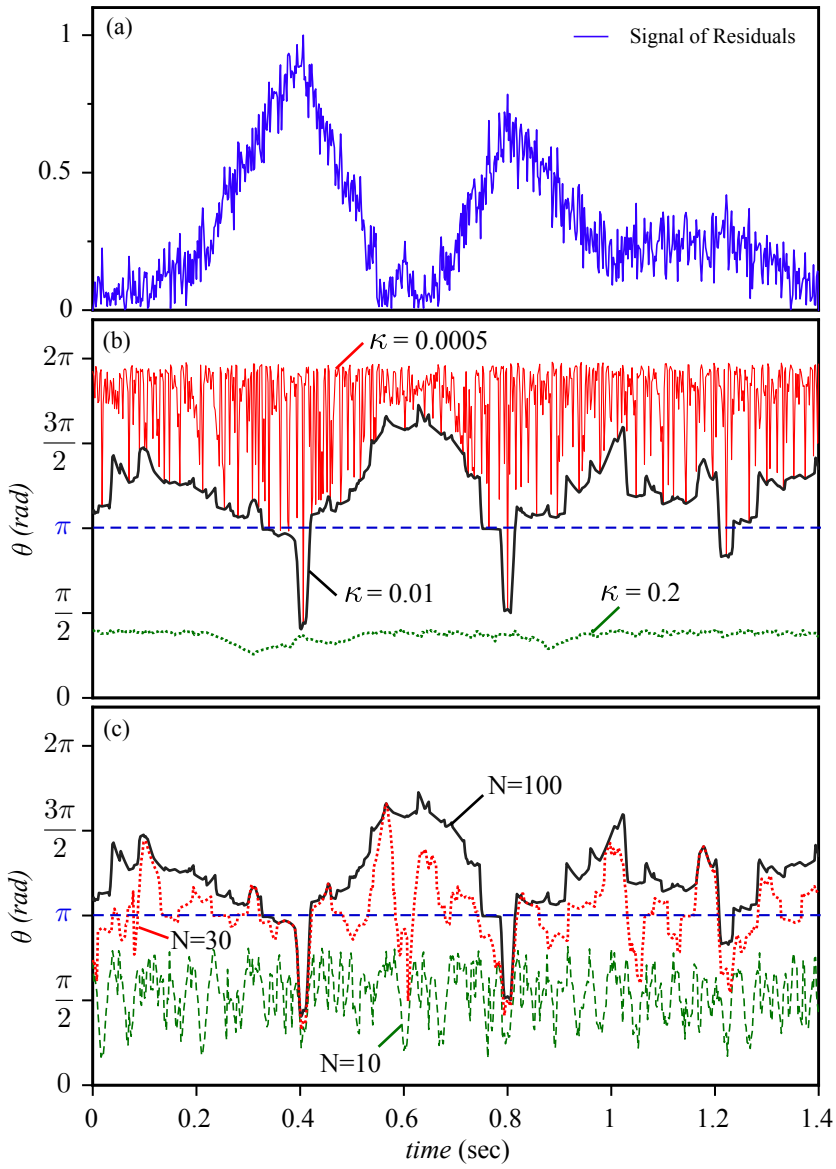

FIGURE 2.6: (a) Signal of residuals over which, the "BBQ Tong" is travelled. (b) Hinge angle for $N = 100$ and $\kappa = 0.0005$, 0.01 and 0.2. (c) Hinge angle for $\kappa = 0.01$ and $N = 10$, 30 and 100.

to be carried into two distinct steps. The first step deals with the tool response to noise alone, and more precisely, it consists in computing the probability density function of the hinge angle for a noise with given statistical properties. The second step deals with the effect of the noise with given statistical properties superimposed on a given signal. In practice, we will consider a simple academic background signal that is an isosceles triangle, with three different angles at the apex.

2.4 Effect of Noise on the Tool Response - Zero Stiffness Case

As discussed earlier, one of the proposed strategies is to seek peaks in the signal of residuals as the points characterised by hinge angles smaller than π using a zero stiffness tool. However, because of the noise, this approach yields also hinge angles below π at locations not associated with a peak. The objective of this section is to find the appropriate tool leg length as to minimise the occurrence of such events.

2.4.1 Response to White Gaussian Noise

The objective of this section is to conduct a thorough parametric analysis of the tool response to a white Gaussian noise, and eventually provide some guidelines for the selection of the tool legs length as a function of the noise intensity. We introduce a discrete-time white Gaussian noise Y uniformly spaced ($T = 0.002$ seconds) with zero mean and a standard deviation of σ

$$Y \sim \mathcal{N}\left(0, \sigma^2\right)$$

and first determine analytically the probability density function of the hinge angle, θ given by a tool with zero stiffness travelled over the signal Y. The response is sought as the probabilistic behaviour of the hinge angle as a function of the noise standard deviation and the tool specifications. The effect of legs length, N, and noise standard deviation, σ, on the hinge angle, θ, is then investigated thoroughly.

The derivation of an analytical solution is a challenging task and commonly such problems are tackled using extensive Monte Carlo simulations which although efficient, are known to offer limited insight.

Both the numerical and analytical intermediate results provided in this section are obtained with a code written under Matlab. For the numerical implementations, a white Gaussian noise with $30,000$ data points is generated.

2.4.1.1 Analytical Solution

As it was mentioned earlier and is also illustrated in Fig. 2.7, when the "BBQ Tong" stiffness is zero, the hinge is always positioned on the residual signal ($\delta = 0$) as the "closing moment" is always equal to zero. The hinge angle, Θ, is then decomposed into

$$\Theta = \Theta_L + \Theta_R, \tag{2.10}$$

with Θ_L, the left angle, and Θ_R, the right angle.

In the sequel, capital letters are used to denote random variables. As a variable takes a particular value, it is denoted with the corresponding lower-case letter.

The process of computing the probability density function of the random variable, Θ, starts with evaluating the probability density functions of the hinge left and right angles i.e. random variables Θ_L and Θ_R. As the derivation is identical for both the left and right angles, the procedure is only detailed for the left angle Θ_L. The pdf of the left and right angles are eventually combined to determine the joint probability density function of the hinge left and right angles, $f_{\Theta_L \Theta_R}(\theta_L, \theta_R)$ and finally the probability density function of θ.

As it is well illustrated in Fig. 2.7, it is first assumed that the left leg touches the residual signal at the i^{th} point on the left side of the hinge where i is the index of any arbitrary point on the signal covered by the left leg ($1 \leq i \leq N$). Note that i is an integer counted from the hinge towards the tip of the "BBQ Tong" left leg.

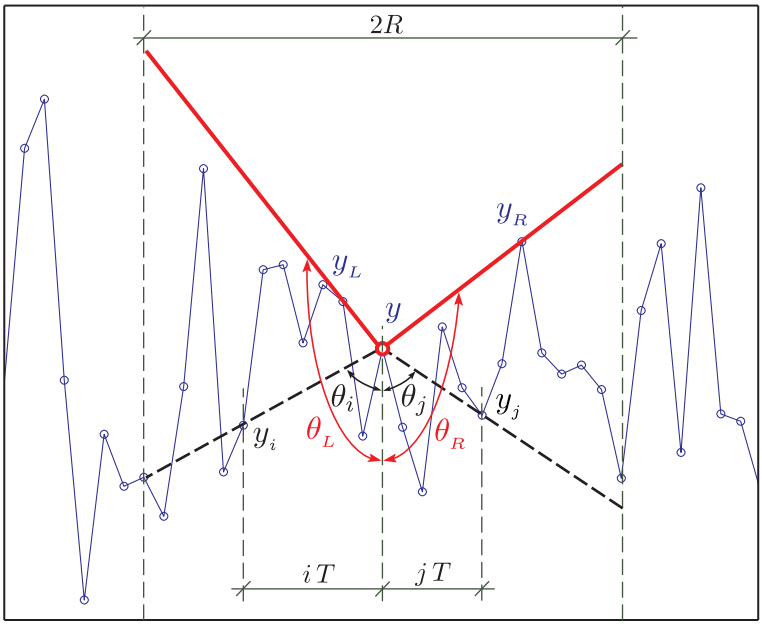

FIGURE 2.7: "BBQ Tong" with zero stiffness sitting on a white Gaussian noise.

The value of the residual signal at contact is Y_i, while the signal value at the hinge location is Y. The hinge left angle Θ_i (the subscript L is kept for the equilibrium

solution) is then related to the residual signal as follows

$$\tan\left(\frac{\pi}{2}-\Theta_i\right)=\frac{Y-Y_i}{i\,T},\qquad 1\leq i\leq N. \tag{2.11}$$

We can then rearrange Eq. (2.11) to obtain Y_i as a function of the rest of the variables

$$Y_i=Y-(i\,T)\tan\left(\frac{\pi}{2}-\Theta_i\right). \tag{2.12}$$

Since we assume that Y and Y_i are independent and identically distributed random variables following a Gaussian distribution (as the noise is considered white Gaussian), for a given value of y we have

$$\left(y-(i\,T)\tan\left(\frac{\pi}{2}-\Theta_i\right)\right)\sim\mathcal{N}(0,\sigma^2). \tag{2.13}$$

The probability density function of the Gaussian random variable , Y_i, with zero mean and standard deviation of σ conditioned on y is defined by [90]

$$f_{Y_i|y}\left(y_i\right)=\frac{1}{\sqrt{2\pi\sigma^2}}\,\exp\left(-\frac{1}{2}\frac{y_i^2}{\sigma^2}\right). \tag{2.14}$$

Eq. (2.12) allows us to express Θ_i as a function of Y_i explicitly. As the probability density function of Y_i is known, the probability density function of Θ_i can be written as [90]

$$f_{\Theta_i|y}(\theta_i)=f_{Y_i|y}\left(g^{-1}(\theta_i)\right)\left|\frac{d}{d\theta_i}g^{-1}(\theta_i)\right|, \tag{2.15}$$

where

$$\Theta_i=g\left(Y_i\right)=\frac{\pi}{2}-\arctan\left(\frac{Y-Y_i}{i\,T}\right). \tag{2.16}$$

Substituting Eqs. (2.14) and (2.16) in Eq. (2.15) and after simplification provides the probability density function of Θ_i conditioned on y as

$$f_{\Theta_i|y}\left(\theta_i\right)=f_{Y_i|y}\left(g^{-1}(\theta_i)\right)\,\left|-(i\,T)\left[1+\tan^2\left(\frac{\pi}{2}-\theta_i\right)\right]\right|, \tag{2.17}$$

where

$$f_{Y_i|y}\left(g^{-1}(\theta_i)\right)=\frac{1}{\sqrt{2\pi\sigma^2}}\,\exp\left[-\frac{1}{2\sigma^2}\left[y-(i\,T)\tan\left(\frac{\pi}{2}-\theta_i\right)\right]^2\right]. \tag{2.18}$$

The corresponding cumulative distribution function (cdf) of Θ_i for a given value of y is then determined by

$$F_{\Theta_i|y}\left(\theta_i\right)=\int_{-\infty}^{\theta_i}f_{\Theta_i|y}\left(\theta_i\right)\,d\theta_i. \tag{2.19}$$

By definition, neither the "BBQ Tong" hinge nor the legs are allowed to penetrate the signal. The criteria yields the final left angle, Θ_L, for a given y as

$$\Theta_L|y = \max\left(\Theta_i|y\right), \qquad 1 \leq i \leq N. \tag{2.20}$$

The cumulative distribution function of Θ_L given y can be determined using order statistics [91]. Considering that for a given y, the variables $\{\Theta_1, \ldots, \Theta_N\}$ are independent and non-identically distributed RVs, the cumulative distribution function of their maximum can be written as the product of their cumulative distribution functions as follows

$$F_{\Theta_L|y}\left(\theta_L\right) = \Pr\left(\Theta_L|y \leq \theta_L\right) = \prod_{i=1}^{N} F_{\Theta_i|y}\left(\theta_L\right). \tag{2.21}$$

Differentiating the cdf of $\Theta_L|y$ (given by Eq. (2.21)) with respect to θ_L, provides the probability density function of the left angle, θ_L, given y. Hence

$$\begin{aligned} f_{\Theta_L|y}\left(\theta_L\right) &= \frac{d}{d\,\theta_L} F_{\Theta_L|y}\left(\theta_L\right) \\ &= \prod_{i=1}^{N} F_{\Theta_i|y}\left(\theta_L\right) \sum_{i=1}^{N} \left[\frac{f_{\Theta_i|y}\left(\theta_L\right)}{F_{\Theta_i|y}\left(\theta_L\right)}\right]. \end{aligned} \tag{2.22}$$

The analytical and numerical representation of the probability density function of $\Theta_L|y$ for a noise standard deviation of $\sigma = 0.01$, $y = 0.02$ and $N = 100$ matches quite well as it is illustrated in Fig. (2.8). Note that Θ_L (Θ_R) always varies between zero and π.

The same procedure has been followed to calculate the probability density function of the right angle, Θ_R given y. The right leg of the "BBQ Tong" touches the residual signal at the j^{th} point on the right side of the hinge where j varies from 1 to N and the probability density function of the right angle given y reads

$$f_{\Theta_R|y}\left(\theta_R\right) = \prod_{i=1}^{N} F_{\Theta_j|y}\left(\theta_R\right) \sum_{j=1}^{N} \left[\frac{f_{\Theta_j|y}\left(\theta_R\right)}{F_{\Theta_j|y}\left(\theta_R\right)}\right]. \tag{2.23}$$

The joint cumulative distribution function of Θ_L and Θ_R conditioned on y can be written as

$$\begin{aligned} F_{\Theta_L\Theta_R|y}\left(\theta_L, \theta_R\right) &= P\left(\Theta_L|y \leq \theta_L,\, \Theta_R|y \leq \theta_R\right) \\ &= \prod_{i=1}^{N} F_{\Theta_i|y}\left(\theta_L\right) \prod_{j=1}^{N} F_{\Theta_j|y}\left(\theta_R\right). \end{aligned} \tag{2.24}$$

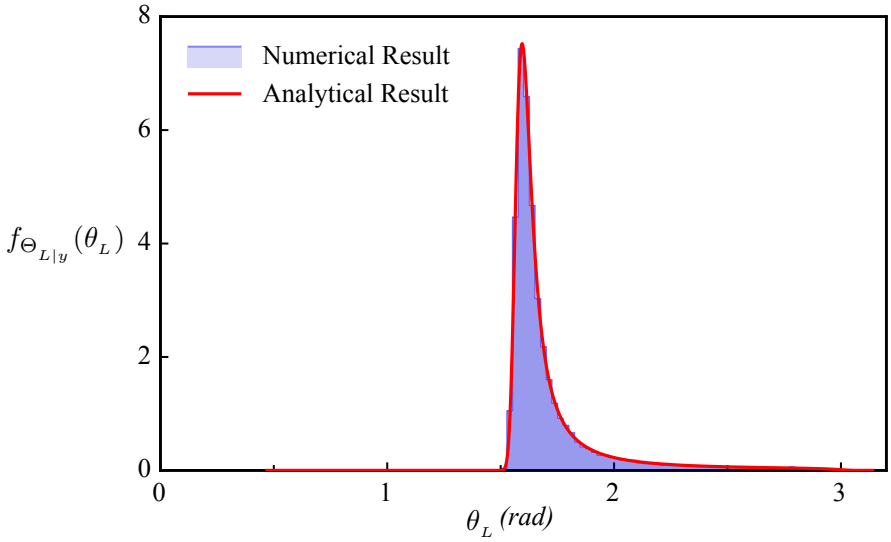

FIGURE 2.8: Numerical and analytical representation of $f_{\Theta_L|y}(\theta_L)$ for $\sigma = 0.01$, $y = 0.02$ and $N = 100$.

The joint probability distribution function of Θ_L and Θ_R given y is obtained by differentiating Eq. (2.24) partially with respect to θ_L and θ_R as follows

$$\begin{aligned} f_{\Theta_L\Theta_R|y}(\theta_L,\theta_R) &= \frac{\partial^2}{\partial\theta_L\,\partial\theta_R} F_{\Theta_L\Theta_R|y}(\theta_L,\theta_R) \\ &= \prod_{i=1}^{N} F_{\Theta_i|y}(\theta_L) \prod_{j=1}^{N} F_{\Theta_j|y}(\theta_R) \\ &\quad \sum_{i=1}^{N}\left[\frac{f_{\Theta_i|y}(\theta_L)}{F_{\Theta_i|y}(\theta_L)}\right] \sum_{j=1}^{N}\left[\frac{f_{\Theta_j|y}(\theta_R)}{F_{\Theta_j|y}(\theta_R)}\right]. \end{aligned} \tag{2.25}$$

Substituting Eqs. (2.22) and (2.23) in Eq. (2.25) provides

$$f_{\Theta_L\Theta_R|y}(\theta_L,\theta_R) = f_{\Theta_L|y}(\theta_L)\; f_{\Theta_R|y}(\theta_R)\,. \tag{2.26}$$

As it can be seen in Eq. (2.26), the joint probability distribution function of Θ_L and Θ_R given y is in fact the product of the conditional probability density functions of the left and right angles. Since the mathematical expression for Θ_L and Θ_R has y in common, these two random variables are expected to be dependent. However, Eq. (2.26) confirms that for a given y, Θ_L and Θ_R are independent. In other words, Θ_L and Θ_R are conditionally independent.

Bayesian rule is then used to eliminate the condition on y from Eq. (2.26). As the probability density function of Y is known ($Y \sim \mathcal{N}\left(0,\sigma^2\right)$), the joint probability

distribution function of Θ_L, Θ_R and Y is determined by

$$f_{\Theta_L\Theta_R Y}(\theta_L, \theta_R, y) = f_Y(y)\ f_{\Theta_L\Theta_R|y}(\theta_L, \theta_R). \tag{2.27}$$

Substituting Eq.(2.26) in Eq. (2.27) results in

$$f_{\Theta_L\Theta_R Y}(\theta_L, \theta_R, y) = f_Y(y)\ f_{\Theta_L|Y}(\theta_L)\ f_{\Theta_R|Y}(\theta_R). \tag{2.28}$$

The marginal joint probability distribution function of Θ_L and Θ_R is then determined by integrating the joint probability distribution of the Eq. (2.28) over all values of y. Hence

$$\begin{aligned} f_{\Theta_L\Theta_R}(\theta_L, \theta_R) &= \int_{-\infty}^{+\infty} f_{\Theta_L\Theta_R Y}(\theta_L, \theta_R, y)\ dy \\ &= \int_{-\infty}^{+\infty} f_Y(y)\ f_{\Theta_L|y}(\theta_L)\ f_{\Theta_R|y}(\theta_R)\ dy. \end{aligned} \tag{2.29}$$

Eq. (2.29) expresses the joint probability distribution function of the left angle, Θ_L, and the right angle, Θ_R, independent of y. As it was discussed earlier, the random variables Θ_L and Θ_R are dependent. Therefore, their joint probability density function is not the product of their individual probability density functions.

The analytical and numerical representation of the joint probability distribution function of Θ_L and Θ_R for $\sigma = 0.01$ and $N = 1$ are in good agreement as it is illustrated in Fig. (2.9).

Recalling Eq. (2.10), the hinge angle Θ can be thought as a function of two dependent random variables, Θ_L and Θ_R i.e.

$$\Theta = g(\Theta_L, \Theta_R). \tag{2.30}$$

Thus, the cumulative distribution function of Θ can be determined by integrating the joint probability distribution function of Θ_L and Θ_R in the plane $\theta_L - \theta_R$ over the region $\theta_L + \theta_R \leq \theta$ [90]. Hence

$$F_\Theta(\theta) = \int_{-\infty}^{+\infty} \int_{-\infty}^{\theta-\theta_R} f_{\Theta_L\Theta_R}(\theta_L, \theta_R)\ d\theta_L\, d\theta_R. \tag{2.31}$$

Finally, the response of the "BBQ Tong" or in other words, the probability density function of Θ is determined by differentiating its cumulative distribution function, $F_\Theta(\theta)$, with respect to θ. As a result

$$f_\Theta(\theta) = \frac{d}{d\theta} F_\Theta(\theta) = \int_{-\infty}^{+\infty} f_{\Theta_L\Theta_R}(\theta_L, \theta - \theta_L)\ d\theta_L. \tag{2.32}$$

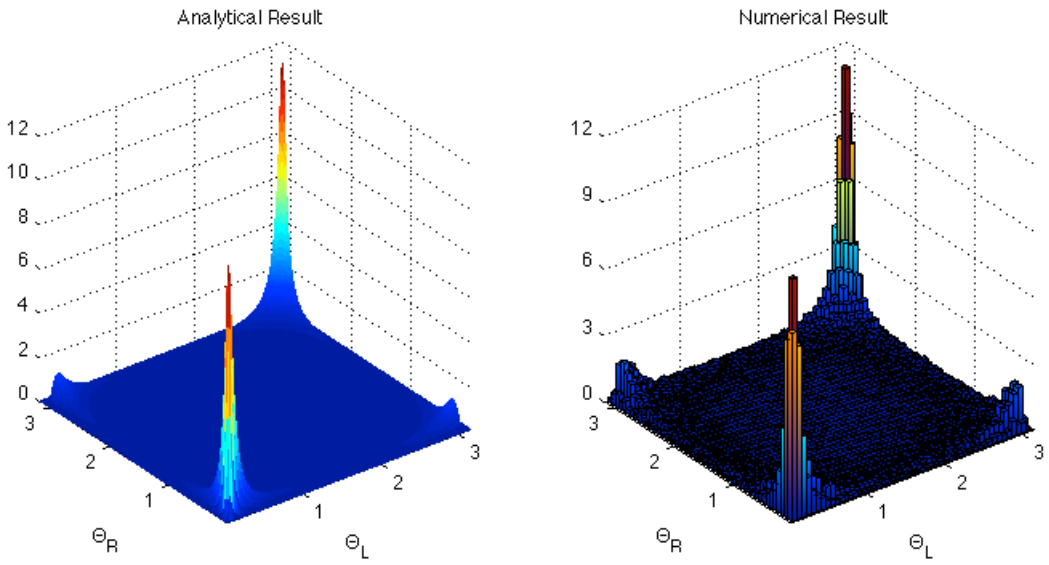

FIGURE 2.9: Numerical and analytical representation of $f_{\Theta_L\Theta_R}(\theta_L, \theta_R)$ for $N = 1$ and $\sigma = 0.01$

which is the analytical expression for the probability density function of the hinge angle, θ, for a given input signal with white Gaussian properties. The analytical and numerical representation of the probability density function of Θ is depicted in Fig. (2.10). Note that the hinge angle can vary from zero to 2π.

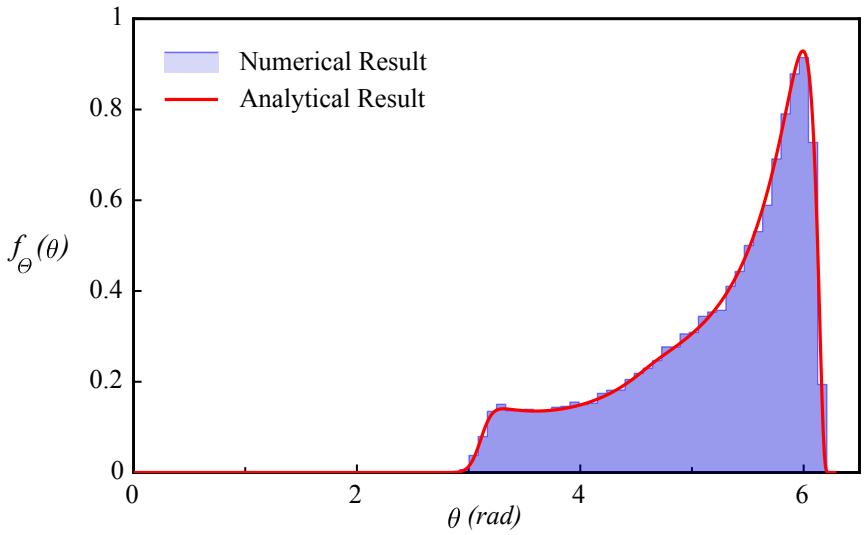

FIGURE 2.10: Numerical and analytical representation of $f_\Theta(\theta)$ for $\sigma = 0.01$ and $N = 100$.

The analytical representation of the hinge angle pdf now allows us to study the

sensitivity of the response to the variation of either the noise standard deviation, σ, or legs length, N.

The response of the "BBQ Tong" to a correlated Gaussian noise has also been derived. For more details refer to appendix B.

2.4.1.2 Parametric Analysis

The analytical solution is a convenient and efficient tool to carry out a parametric analysis and explore the effect of the legs length and the noise intensity on the tool response. The response of the "BBQ Tong" with zero stiffness and various legs length N, to a white Gaussian noise with zero mean and standard deviation of 0.01 is shown in Fig. 2.11. For small values of N, considerable part of the hinge angle's probability density function covers angles below π. (Recall that the strategy proposed earlier consists in using a tool with zero stiffness and select points with angle below π as break-points.) For example, when $N = 1$, there are precisely fifty percent occurrences of the hinge angles to be smaller than π as the corresponding pdf in Fig. 2.11 is symmetric with respect to π (time-step taken $T = 0.002$ seconds for this plot).

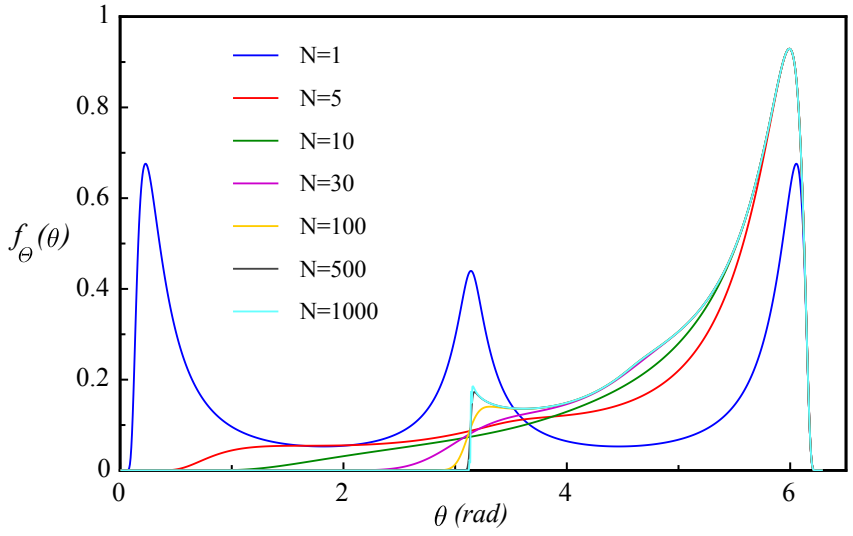

FIGURE 2.11: Pdf of the hinge angle ($\kappa = 0$) for different leg lengths (N), response to a white Gaussian noise with a zero mean and a standard deviation $\sigma = 0.01$.

Increasing N allows the legs to reach local maxima located at further distance from the hinge (when the hinge itself is located on a local maxima). Therefore, the likelihood of the hinge angle being larger than π increases smoothly as the tool legs become longer.

This is also illustrated in Fig. 2.11 as the probability density function of θ drifts to the right side with the increase of N.

The response of the "BBQ Tong" with $\kappa = 0$ and $N = 100$ to a white Gaussian noise with zero mean and various standard deviation ($\sigma = 0.01$, 0.02, 0.05 and 0.01) is illustrated in Fig. 2.12. Increasing the noise intensity distorts the tool response causing (i) hinge angles larger than π to become even larger and (ii) angles smaller than π to become smaller. Therefore, when the majority of the probability density function of θ is located above π (in other words, when there is more than fifty percent chance for the hinge angle to be above π), the probability density function of θ shifts to the right side and becomes eventually narrower as the standard deviation of the noise increases (see Fig. 2.12).

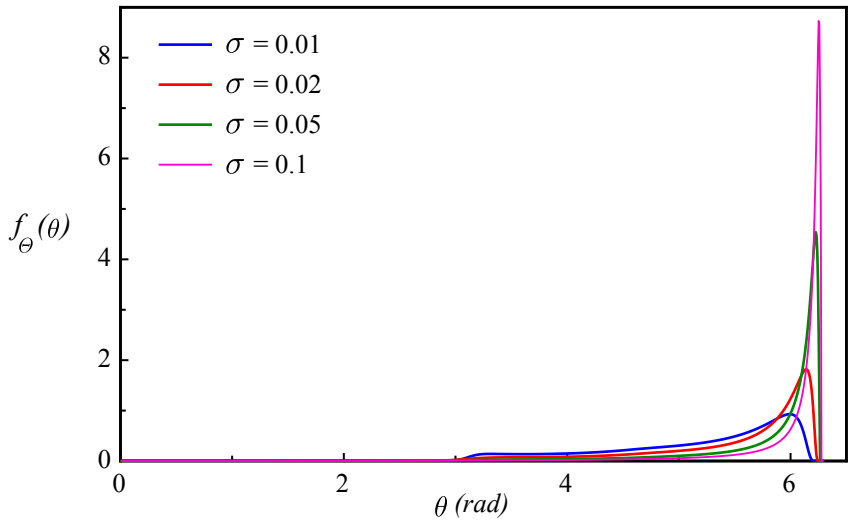

FIGURE 2.12: Pdf of the hinge angle ($\kappa = 0$) for different noise standard deviations (σ), response to a white Gaussian noise with legs length $N = 100$.

We now introduce S as the area under the probability density function of θ from 0 to π as

$$S = \int_0^{\pi} f_{\Theta}(\theta)\, d\theta, \tag{2.33}$$

which denotes the probability of the hinge angle, θ, being smaller or equal to π.

Interestingly, the integral is first found independent of the noise intensity but also decreasing with increasing legs length N (see Fig. 2.13). This is due to the fact that a change in the noise standard deviation does not affect the ratio between the number of angles below and over π. Therefore, the probability of θ being below (or over) π for

a given N but varying σ remains unchanged.

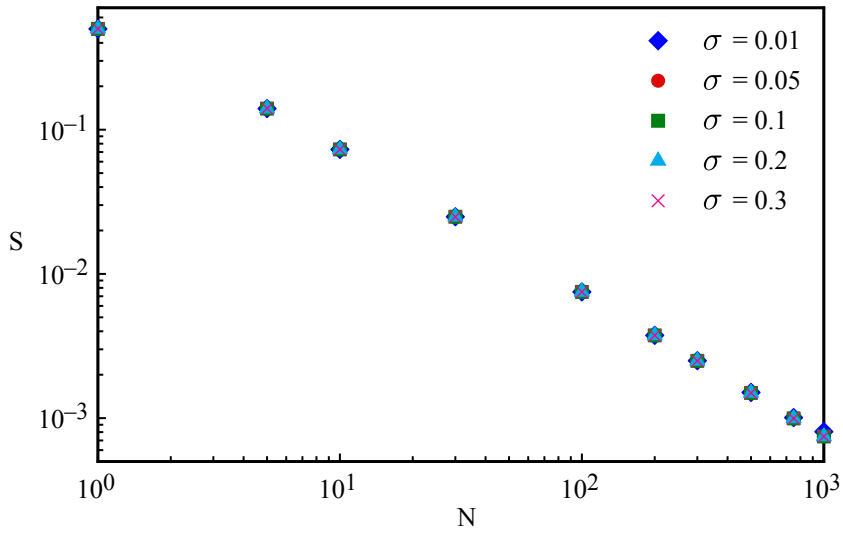

FIGURE 2.13: Evolution of S versus N in a logarithmic scale for various noise standard deviation σ.

Increasing N reduces the amount of points characterised by a hinge angle smaller than π, but also yields higher computation time and affects the minimum size segments the method can capture. In addition, although S decreases with N, it never reaches zero, as there is always at least one point (the maximum) with a hinge angle smaller than π. It means that the method would yield points with hinge angles smaller than π that are actually not break-points and would require particular attention.

2.4.2 Noise Superimposed on Background Signal

The theoretical study outlined above provides some insight on the effect of the noise on the tool response. It is however not sufficient to make inferences about the response of the "BBQ Tong" to any signal corrupted by a white Gaussian noise. In fact, the effect of the noise on the tool response varies with the local properties of the underlying signal. For that purpose, we have considered an academic example with a background signal that consists of a simple isosceles triangle superimposed on a white Gaussian noise (with zero mean and $\sigma = 0.01$, 0.1 and 0.3). We consider three distinct triangles characterised by a different angle at the apex: sharp (0.395 rad), moderate (0.761 rad) and flat (2.214 rad), see Fig. 2.14.

Each peak has 200 data points equally spaced with $T = 0.002$ seconds and is

analysed separately (zero padded whenever required). Note that the simulation for every peak and given tools length, N, and noise intensity, σ, is repeated for $30,000$ different randomly created noise vectors to draw statistical inferences.

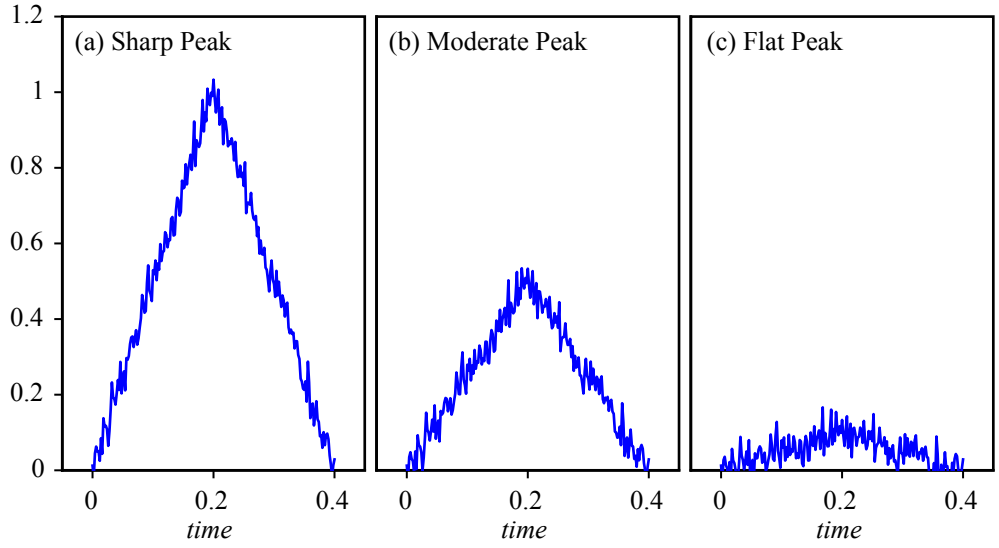

FIGURE 2.14: Three background peaks: (a) Sharp (b) Moderate and (c) Flat, corrupted by white Gaussian noise.

Let us name t_p, the vector of position (time index) associated with hinge angles below π. The histogram of the computed t_p over $30,000$ runs (the time index of the angles below π at each run is identified and stored in t_p) for $N = 100$ and each peak style and noise standard deviation is shown in Fig. 2.15. As it is well illustrated, the histogram is clearly affected by the sharpness of the background peak in relation to the noise intensity, for the same noise intensity, smaller peak angle results in wider histograms. Higher noise intensity widens the histograms, as the signal-to-noise ratio (SNR) decreases, the probability of outliers yielding angles below π increases significantly.

We now introduce the variable γ defined as the ratio of the standard deviations of t_p to the width of the background peak (equal to 0.4 in the examples). The evolutions of γ with respect to the noise standard deviation for different values of N (10, 50, 100, 200 and 500) and each type of peak (sharp, moderate and flat) are illustrated in Figs. 2.16, 2.17 and 2.18 respectively. This scaled standard deviation is a measure of the deviation in terms of relative position error with respect to the location of the true peak.

As the noise intensity increases, the standard deviation of t_p always increases regardless of the peak style and legs length N. However, the rate of growth increases

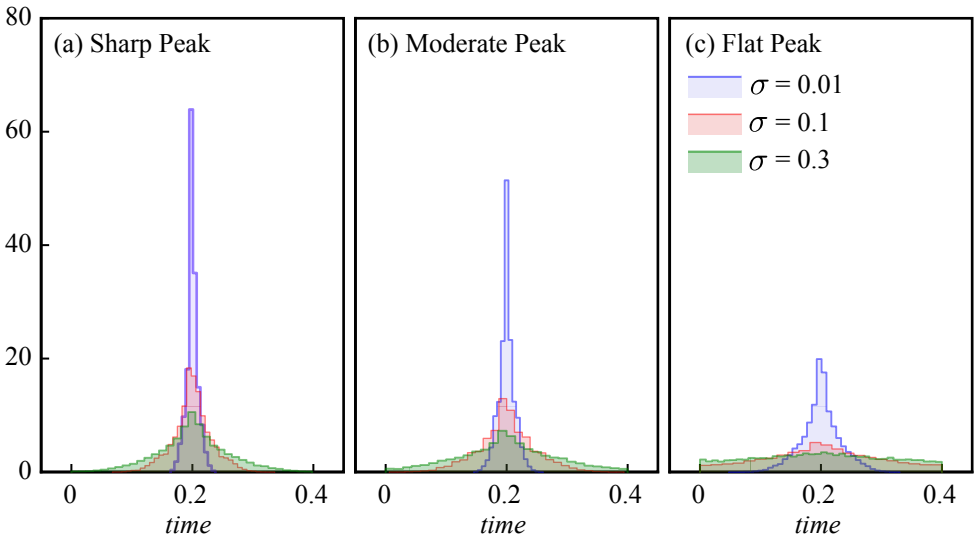

FIGURE 2.15: Histogram of the position of the hinge angles below π for $N = 100$ and various noise intensities.

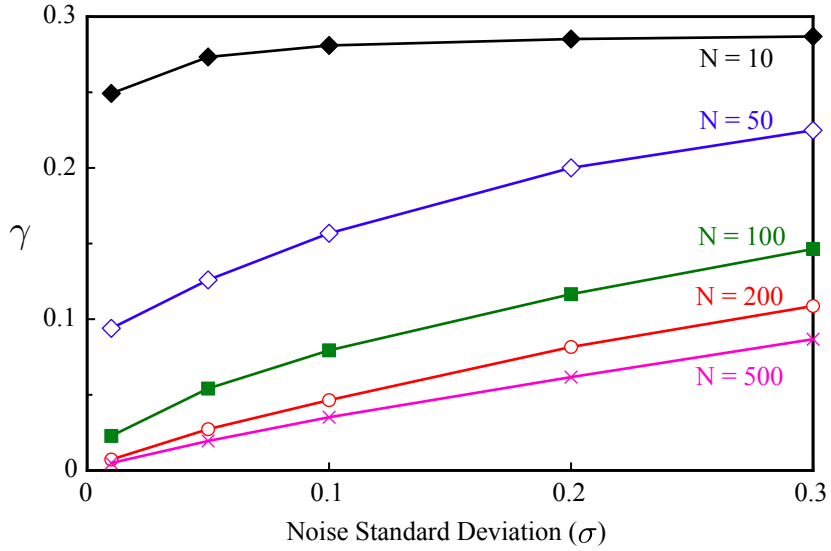

FIGURE 2.16: Standard deviation of t_p scaled by the peak width (γ) for various noise intensities, σ, and legs length, N (Sharp Peak).

as the peak style varies from "Sharp" to "Flat". Note that the lower the standard deviation of t_p, the higher the chance of the candidate break-points to be closer to the true break-point (peak apex).

It can be also inferred from Figs. 2.16, 2.17 and 2.18 that for a given noise intensity, increasing N leads to a significant drop in the t_p standard deviation regardless of the peak style. Nevertheless, the rate of change (drop) increases with the peak varying

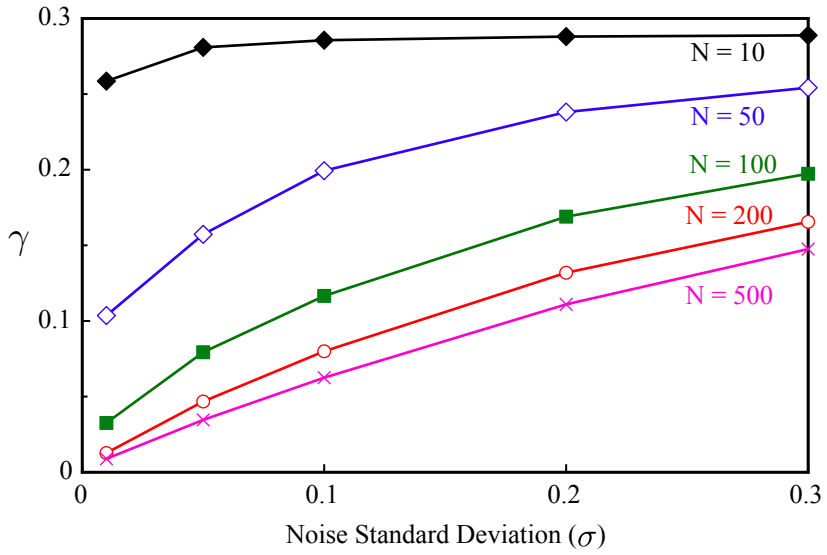

FIGURE 2.17: Standard deviation of t_p scaled by the peak width (γ) for various noise intensities, σ, and legs length, N (Moderate Peak).

from "Flat" to "Sharp".

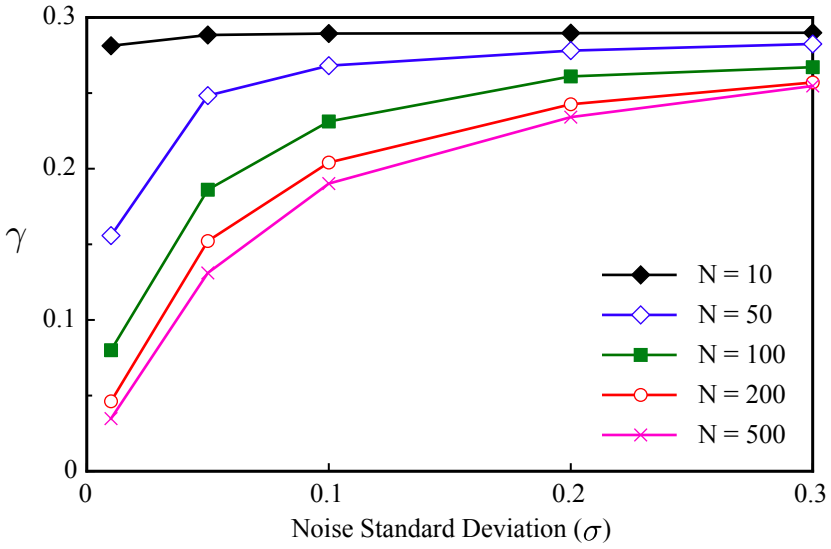

FIGURE 2.18: Standard deviation of t_p scaled by the peak width (γ) for various noise intensities, σ, and legs length, N (Flat Peak).

Finally, Figs. 2.16, 2.17 and 2.18 imply that for a given N and σ, transition from "Sharp" to "Flat" peak increases the probability of the points with angle below π being located at the further distance from the peak apex. As a result, the quality of the approximation is reduced in the vicinity of the peaks with lower angles.

2.5 Effect of Noise on the Tool Response - Non-Zero Stiffness Case

Similar to sec. 2.4, the response of the "BBQ Tong" with non-zero stiffness to a white Gaussian noise is first studied. Then, the sensitivity of the tool response to the sharpness of the background peaks is investigated by considering the simple academic background signal that is an isosceles triangle, with three different angles at the apex (described earlier in sec. 2.4.2) corrupted by white Gaussian noise with various intensities.

2.5.1 Response to White Gaussian Noise

Similar to sec. 2.4, in this section, we determine first analytically, the probability density function of the hinge angle, θ, given by a tool with non-zero stiffness travelled over a discrete-time white Gaussian noise Y, uniformly spaced with a zero mean and a standard deviation of σ ($Y \sim \mathcal{N}\left(0, \sigma^2\right)$).

The probabilistic response in the non-zero case is rather complex since the hinge position over the signal (δ^*) is a random variable obtained by solving the moment equilibrium equation of the tool described earlier in secs. 2.2.2 and 2.2.3. Thus, the analytical derivation is a challenging task and requires adequate recourse to extreme order statistics and first passage time analysis of stochastic processes. Despite the fact that analytical approaches are quite uncommon for such problem for which extensive Monte Carlo simulations are usually preferred, however, in this research, analytical study is carried out to obtain the final probabilistic response.

Similar to sec. 2.4.1, both numerical and analytical intermediate results provided in this section are obtained using a code written under Matlab. For the numerical implementations, white Gaussian noise with $30,000$ data points and time-step $T = 0.002$ seconds is generated within Matlab.

2.5.1.1 Analytical Solution

The response of the tool with non-zero stiffness is different from the one obtained in sec. 2.4 for the zero stiffness tool. Depending on (i) the geometry of the local features of the signal being covered by the legs and (ii) the tool specifications, the hinge finds equilibrium at a distance δ^* above the signal where δ^* is also a random variable.

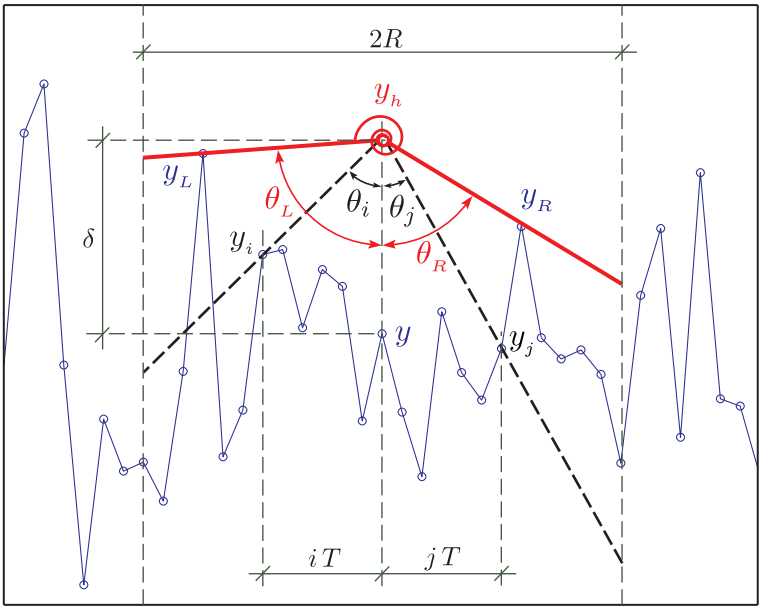

FIGURE 2.19: "BBQ Tong" with non-zero stiffness sitting on a Gaussian white noise.

The final position of the hinge above the signal at any given position can be found using the procedure described in sec. 2.2.3. The goal here is to translate this procedure in a probabilistic manner. To achieve this goal, two random (stochastic) processes are introduced as follows

$$\mathbf{x}_1(\delta) = \kappa\,\theta, \qquad \mathbf{x}_2(\delta) = \left(\frac{\ell\, r}{\ell + r}\right). \tag{2.34}$$

The newly introduced random processes, $\mathbf{x}_1(\delta)$ and $\mathbf{x}_2(\delta)$, are in fact the left and right hand side of the tool moment equilibrium equation, respectively. They are given by Eq. (2.7) and are referred to as the "closing" and "opening" moments. The process $\mathbf{x}_1(\delta)$ is a continuous-state strictly decreasing random process which varies between zero and $2\kappa\pi$ for any value of δ while $\mathbf{x}_2(\delta)$ is a discontinuous-state increasing random process as it can only exhibit discontinuous paths which are piece-wise linear constant functions varying between $\frac{1}{2}$ and $\frac{N}{2}$ at any "instant" of δ (see Eq. (2.9)).

For any fixed δ, $\mathbf{x}_1(\delta)$ and $\mathbf{x}_2(\delta)$ are simply random variables equal to the state of the given processes at distance δ. These states are labelled X_1 and X_2 respectively.

The solution to the moment equilibrium given by Eq. (2.7) is in fact equivalent to the state where process $\mathbf{x}_1(\delta)$ passes process $\mathbf{x}_2(\delta)$ or simply when process $\mathbf{x}(\delta)$ passes zero, with $\mathbf{x}(\delta)$ defined as

$$\mathbf{x}(\delta) = \mathbf{x}_1(\delta) - \mathbf{x}_2(\delta). \tag{2.35}$$

Note that the random process $\mathbf{x}(\delta)$ is also strictly decreasing and for a fixed value of δ, is simply a random variable labelled X. Thus, at any fixed δ

$$X = X_1 - X_2. \tag{2.36}$$

This so-called first passage [92, 93] takes place at a random distance, $\delta^\diamond$, which varies from realization to realization. Therefore, the first passage distance $\delta^\diamond$ is a random variable. It is worth mentioning that $\delta^\diamond$ is different from δ^* as at this stage, the passage can occur at negative values of δ as well. After enforcing the non-penetration condition for the hinge (see sec. 2.2.3), δ^* is simply obtained by

$$\delta^* = \max\left(0, \delta^\diamond\right). \tag{2.37}$$

To compute the probability density function of Θ, the probability density function of the first passage distance, $\delta^\diamond$, is required. For this purpose, we first need to determine the probability density function of X. It can be inferred from Eq. (2.36) that knowledge of the joint probability distribution of the random variables X_1 and X_2 is necessary and sufficient to obtain the pdf of X.

The analytical representation of the joint probability distribution function of X_1 and X_2 for given values of $y = 2$ and $\delta = 0$, $N = 10$, $\sigma = 1$ is well illustrated in Fig. (2.20). For details on how to obtain the joint probability distribution function of the random variables X_1 and X_2, refer to appendix C.

The function $f_{X_1X_2|y,\delta}\left(x_1, x_2\right)$ is the joint probability distribution of the continuous random variable, X_1, and the discrete random variable, X_2 for given values of y and δ. Therefore, as shown in Fig. (2.20), its representation is continuous in one dimension and discrete in the other dimension. Knowing the joint probability distribution of X_1 and X_2 given y and δ, the cumulative distribution function of X under the same conditions is determined by integrating the joint in $x_1\, x_2$ plane over the region with $x_1 - x_2 \leq x$. Thus

$$F_{X|y,\delta}\left(x\right) = \sum_{x_2} \int_{-\infty}^{x+x_2} f_{X_1X_2|y,\delta}\left(x_1, x_2\right)\, dx_1. \tag{2.38}$$

Note that, as the joint pdf of X_1 and X_2 is discrete with respect to any realisation of x_2, the integration operator is substituted by summation operator.

Finally, the probability density function of X, given y and δ, is determined by

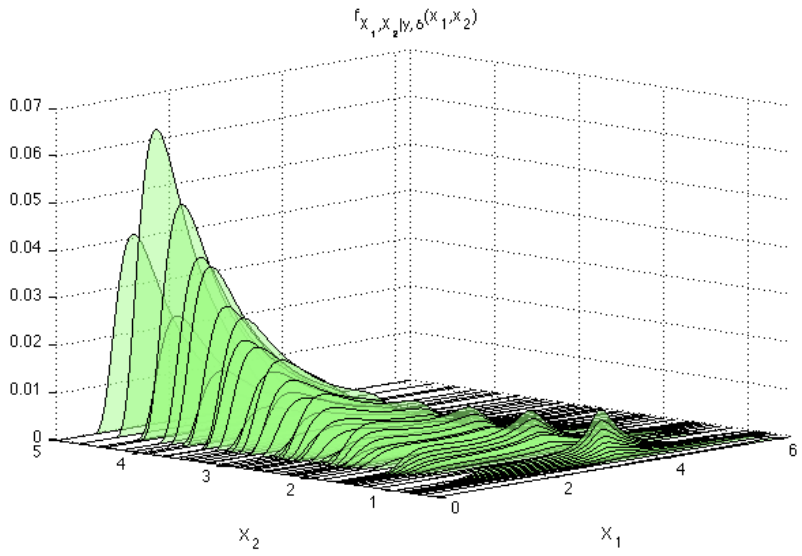

FIGURE 2.20: Analytical representation of $f_{X_1X_2|y,\delta}(x_1, x_2)$ for $y = 2$ and $\delta = 0$, $N = 10$, $\sigma = 1$.

differentiating its cumulative distribution function, $F_{X|y,\delta}(x)$, with respect to x

$$f_{X|y,\delta}(x) = \frac{\partial}{\partial x} F_{X|y,\delta}(x) = \sum_{x_2} f_{X_1X_2}(x + x_2, x_2). \tag{2.39}$$

The analytical and numerical representation of the probability density function of X for given values of $y = 0$, $\delta = 0$, 1.5, 4, $N = 10$, $\sigma = 1$ and $\kappa = 1$ is illustrated in Fig. (2.21).

As it is shown in Fig. (2.21), it can be inferred that for the given configuration, the probability that the random process $\mathbf{x}(\delta)$ passes zero at either $\delta = 0$ or $\delta = 4$ is nearly zero. That is because, at $\delta = 0$, the random variable X is always positive as almost the entire probability density function of X for $\delta = 0$ is located at the right side of $x = 0$. For the same reason, the probability of the zero passage occurrence of $\mathbf{x}(\delta)$ at $\delta = 4$ is zero as well. However, it is more likely to have the first passage occurring at $\delta = 1.5$ as X can take an either positive or negative values. Remember that the passage occurs when the random process $\mathbf{x}(\delta)$ changes its instant state from positive values to negative values.

Despite the complexity associated with extracting the joint probability distribution of the continuous random variable X_1, and discrete random variable X_2 (with non-uniformly spaced outcomes), and the challenges related to the numerical implementation of the obtained solutions, the analytically observed complex shaped prob-

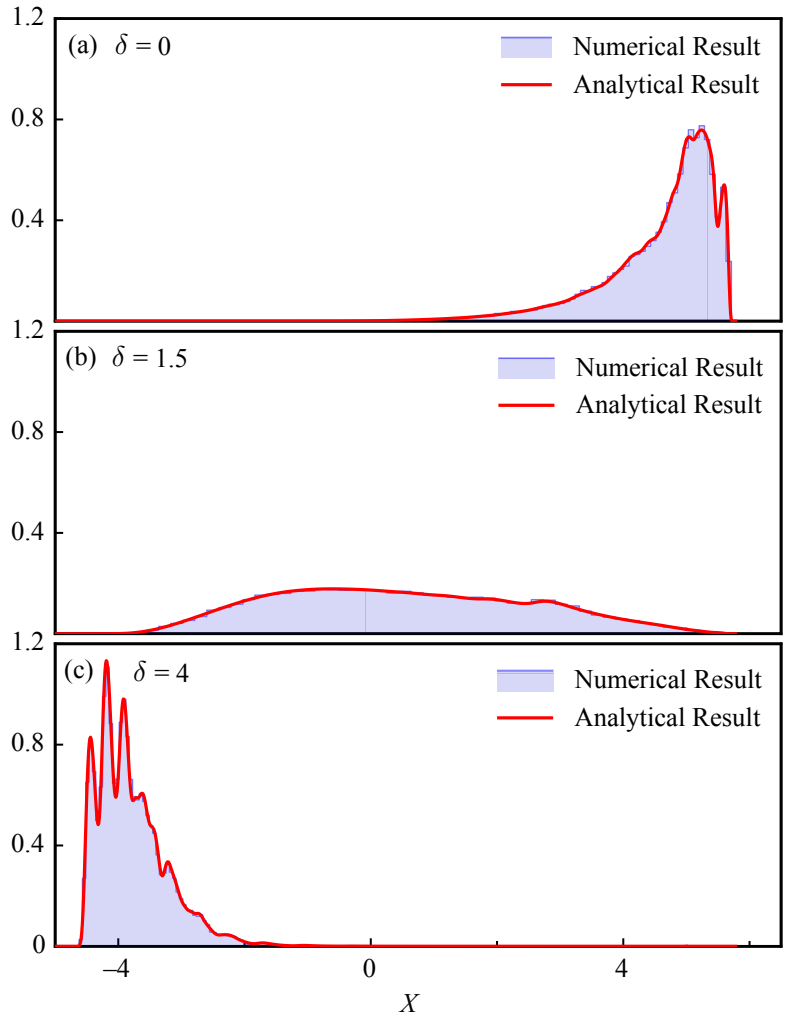

FIGURE 2.21: Numerical and analytical representation of $f_{X|y,\delta}(x)$ for $y = 0$, $\delta = 0$ (a), $\delta = 1.5$ (b), $\delta = 4$ (c), $N = 10$, $\sigma = 1$ and $\kappa = 1$.

ability density functions, as shown in Fig. (2.21), are in complete agreements with the numerical results.

Random variables X_p and X_n are introduced as the states of the random process $\mathbf{x}(\delta)$ just before (at the fixed distance δ and given y) and just after (at the fixed distance $\delta + d\delta$ and given y) the zero passage occurs. As it was mentioned earlier, the random process $\mathbf{x}(\delta)$ is strictly decreasing. As a result, the probability density function of the first passage distance, $\delta^{\diamond}$, can be written as the double integral of the joint probability distribution of X_p and X_n in $x_p x_n$ plane over the region where x_p is positive and x_n is

negative [90]. Thus,

$$\begin{aligned} f_{\Delta^\diamond|y}(\delta^\diamond)\,d\delta^\diamond &= \Pr\left(X_p > 0 \,\&\, X_n < 0\right) \\ &= \int_{-\infty}^{0}\left(\int_{0}^{+\infty} f_{X_pX_n}(x_p, x_n)\,dx_p\right)dx_n, \end{aligned} \tag{2.40}$$

where $f_{X_pX_n}(x_p, x_n)$ is the joint probability distribution function of X_p and X_n. Note that $\delta < \delta^\diamond < \delta + d\delta$. After some development, the probability density function of $\delta^\diamond$ conditioned on y is given by

$$\begin{aligned} f_{\Delta^\diamond|y}(\delta^\diamond) &= \frac{1}{d\delta^\diamond}\int_{-\infty}^{0}\left(f_{X|y,\delta+d\delta}(x) - f_{X|y,\delta}(x)\right)dx \\ &= \frac{1}{d\delta^\diamond}\left(F_{X|y,\delta+d\delta}(0) - F_{X|y,\delta}(0)\right). \end{aligned} \tag{2.41}$$

The derivations leading to Eq. (2.41) are detailed in appendix D. Note that the general form of the first passage time problems in stochastic processes are usually tackled by solving the *Fokker − Planck* equation of the Markov process being studied [94]. However, as $\mathbf{x}(\delta)$ is strictly decreasing, the solution is simplified to Eq. (2.40).

The analytical and numerical representations of the probability density function of $\delta^\diamond$ for given values of $y = 0$, $N = 10$, $\sigma = 1$ and $\kappa = 0.2$, 2 is illustrated in Fig. 2.22.

Finally, using Eq. (2.37), the probability density function of δ^* is expressed as

$$f_{\Delta^*|y}(\delta^*) = \begin{cases} \int_{-\infty}^{0} f_{\Delta^\diamond|y}(\delta^\diamond)\,d\delta^\diamond & , \quad \delta^* = 0 \\ \\ f_{\Delta^\diamond|y}(\delta^\diamond) & , \quad \delta^* > 0, \end{cases} \tag{2.42}$$

as for any negative occurrences of $\delta^\diamond$, the moment equilibrium equation of the tool is no longer a valid measure to determine the position of the hinge with respect to the signal and the hinge is simply positioned on the signal (see also sec. 2.2.3).

The probability density function of X_1^* ("closing moment" after solving the moment equilibrium equation of the tool and enforcing the non penetration condition), is affected depending on whether the zero passage happened or the hinge is positioned on the signal. For either conditions, the pdf of X_1^* for given values of δ and y is obtained using the joint probability distribution function of X_1 and X_2 provided in appendix C. Hence [90]

$$f_{X_1^*|y,\delta}(x_1^*) = \begin{cases} \frac{\sum_{x_1<x_2} f_{X_1X_2|y,\delta^*}(x_1,x_2)}{\sum_{x_2}\int_{-\infty}^{x_2} f_{X_1X_2|y,\delta^*}(x_1,x_2)\,dx_1} & , \quad \delta^* = 0 \\ \\ \frac{f_{X_1X_2|y,\delta^*}(x_1,x_2=x_1)}{f_{X_2|y,\delta^*}(x_2=x_1)} & , \quad \delta^* > 0. \end{cases} \tag{2.43}$$

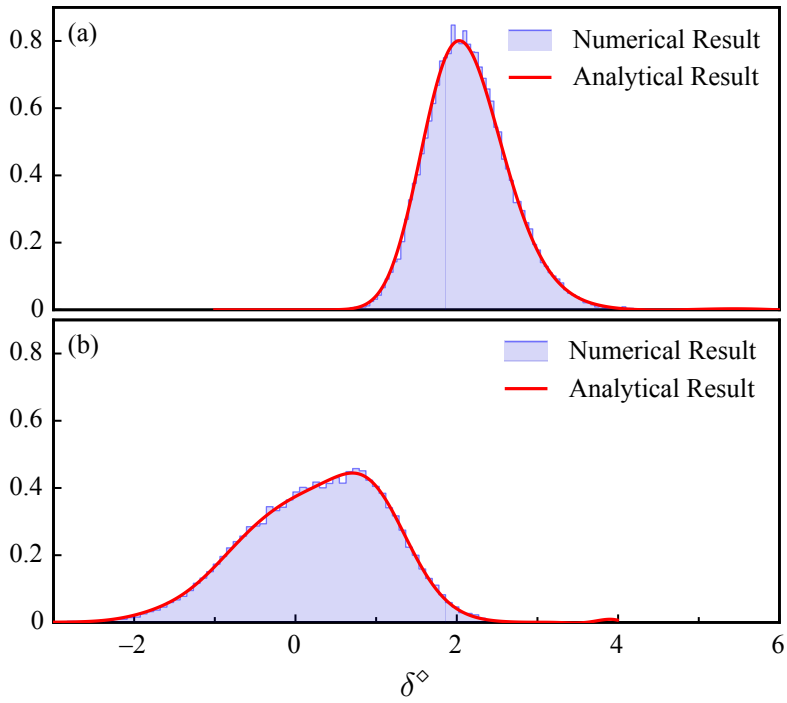

FIGURE 2.22: Numerical and analytical representation of $f_{\Delta^{\diamond}|y}(\delta^{\diamond})$ for $y = 0$, $N = 10$, $\sigma = 1$, $\kappa = 2$ (a) and $\kappa = 0.2$ (b).

The condition $\delta^* = 0$ is simply equivalent to $x_1 < x_2$. In this case, the hinge is always positioned on the signal and X_1^* is a continuous random variable. However, when $\delta^* > 0$, the random variable X_1^* corresponds to the observations associated to $x_1 = x_2$, and therefore, always takes discrete values.

The analytical and numerical representations of the probability mass function of X_1^* for given values of $y = 0$, $\delta^* = 2$, $N = 10$, $\sigma = 1$ and $\kappa = 2$ match as it is well illustrated in Fig. (2.23).

The final goal of this section is to obtain the marginal probability density of X_1^* (and Θ). As the probability density function of δ^* is known, the joint probability distribution function of X_1^* and δ^* is obtained using the Bayesian rule as

$$f_{X_1^*\Delta^*|y}(x_1^*, \delta^*) = f_{X_1^*|y,\delta}(x_1^*)\, f_{\Delta^*}(\delta^*). \tag{2.44}$$

The marginal density function of X_1^* given y is then determined by integrating the joint over all possible values of δ^*. Thus

$$f_{X_1^*|y}(x_1^*) = \int_{-\infty}^{+\infty} f_{X_1^*\Delta^*|y}(x_1^*, \delta^*)\, d\delta^* = \int_{-\infty}^{+\infty} f_{X_1^*|y,\delta}(x_1^*)\, f_{\Delta^*}(\delta^*)\, d\delta^*. \tag{2.45}$$

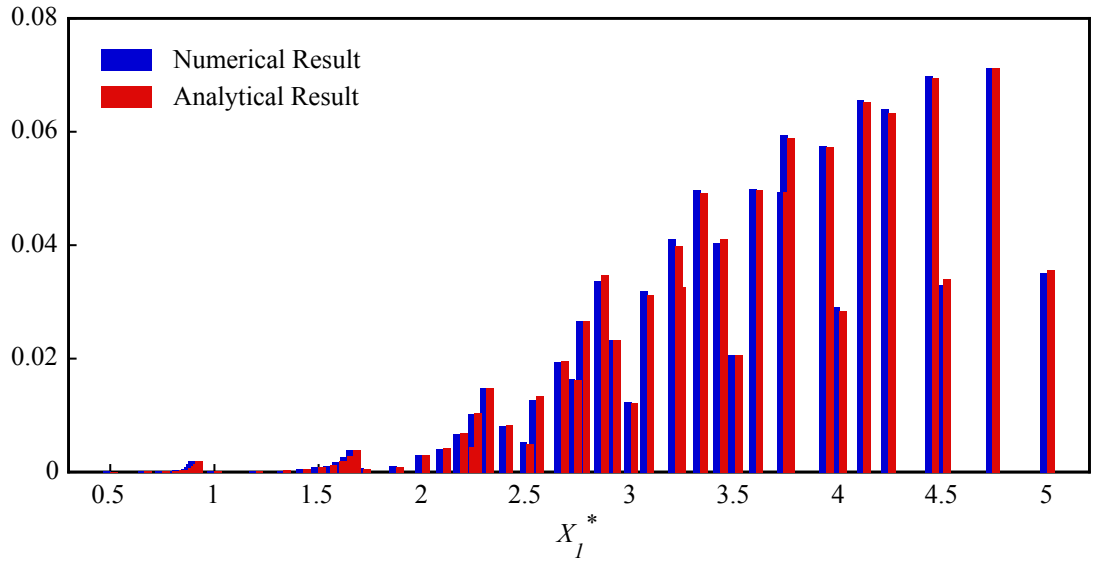

FIGURE 2.23: Numerical and analytical representation of $f_{X_1^*|y,\delta^*}(x_1^*)$ for $y = 0$, $\delta^* = 2$, $N = 10$, $\sigma = 1$ and $\kappa = 2$.

The analytical and numerical representation of the probability distribution function of X_1^*, for given values of $y = 2$, $N = 10$, $\sigma = 1$ and $\kappa = 2$ is illustrated in Fig. (2.24). The contribution of the pdf of X_1^* for $\delta^* = 0$ (continuous trend) and the pmf of X_1^* for $\delta^* > 0$ (spikes) is well observed in the figure.

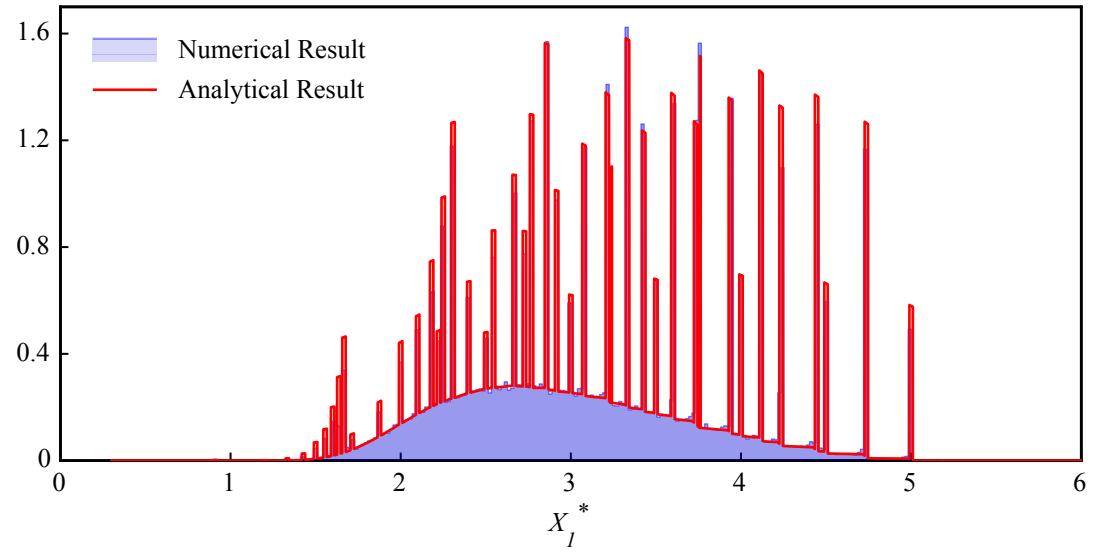

FIGURE 2.24: Numerical and analytical representation of $f_{X_1^*|y}(x_1^*)$ for $y = 2$, $N = 10$, $\sigma = 1$ and $\kappa = 2$.

Use of the Bayesian rule provides the joint probability distribution function of X_1^*

and Y as

$$f_{X_1^*Y}(x_1^*, y) = f_{X_1^*|y}(x_1^*)\, f_Y(y), \tag{2.46}$$

and the marginal probability density function of X_1^* is then determined by

$$f_{X_1^*}(x_1^*) = \int_{-\infty}^{+\infty} f_{X_1^*Y}(x_1^*, y)\, dy = \int_{-\infty}^{+\infty} f_{X_1^*|y}(x_1^*)\, f_Y(y)\, dy. \tag{2.47}$$

Using Eq. (2.34), the probability density function of the hinge angle, Θ, is given by

$$f_\Theta(\theta) = \kappa\, f_{X_1^*}(\kappa\theta). \tag{2.48}$$

Equation (2.48) expresses the analytical solution for the probability density function of the hinge angle, θ, for a given input signal with white Gaussian properties.

Unfortunately, numerical implementation of the derived solution leads to excessive running time in particular for $N > 10$ and is thus impractical to conduct thorough parametric analysis that was such performed using extensive Monte Carlo simulations. However, the analytical derivation and some intermediate results provide clear insight on the tool behaviour providing such guidelines.

2.5.1.2 Parametric Analysis

In the case of non-zero stiffness, the segmentation strategy relies on filtering the effect of the noise with the tool properties tuned such that the hinge angle while travelling on noise is close to π. The response of the "BBQ Tong" with two combinations of stiffness and legs length ($N = 100$ and $\kappa = 0.01$ and 0.1) to a white Gaussian noise with zero mean and various values of standard deviation are shown in Figs. 2.25 and 2.26. The results are obtained using a white Gaussian noise including $30,000$ data points equally spaced with time-step $T = 0.002$ seconds.

As it is illustrated in Fig. 2.25, for given "BBQ Tong" specifications with $N = 100$ and $\kappa = 0.01$, increasing the noise standard deviation displaces the corresponding probability density function to the right side as the majority (more than fifty percent) of the hinge angles for $\sigma = 0.01$ are above π. Fig. 2.25 also shows how the standard deviation of the hinge angle increases (the pdf widens) along with the growth in the noise intensity for given tool specifications.

As it is shown in Fig. 2.26, increasing the stiffness of the "BBQ Tong" to $\kappa = 0.05$ with N kept constant, results in decreasing the values of the hinge angle, θ, as the hinge is forced to be positioned further away from the signal to satisfy the tool equilibrium

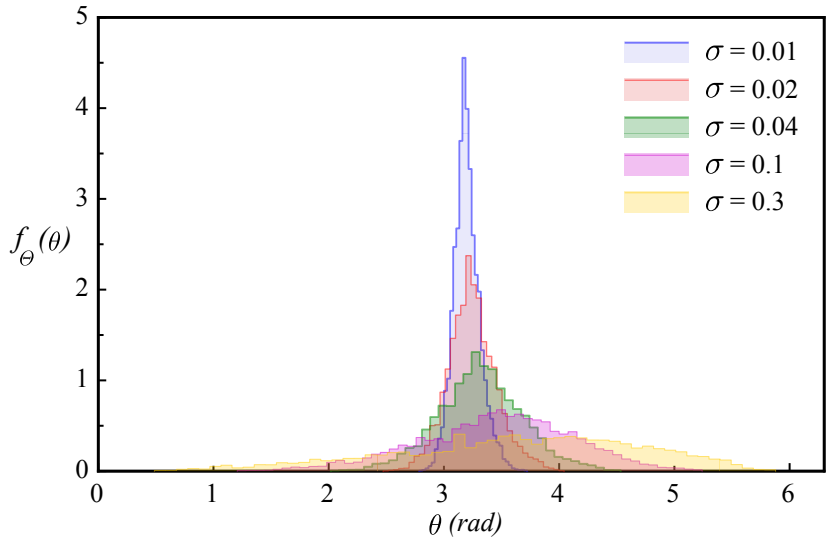

FIGURE 2.25: Pdf of the hinge angle for $\kappa = 0.01$, $N = 100$ and different noise standard deviations σ.

equation, Eq. (2.7). However, this time, increasing the noise standard deviation forces the probability density function of the hinge angle to move to the left since the entire pdf of θ for $\sigma = 0.01$ is located below π. Alike Fig. 2.25, the standard deviation of the hinge angle once more tends to increase as the noise intensity goes up.

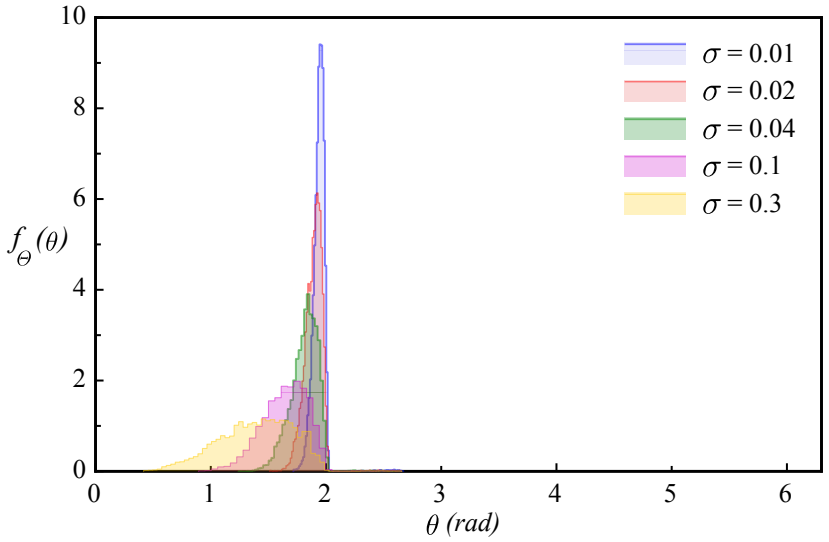

FIGURE 2.26: Pdf of the hinge angle for $\kappa = 0.05$, $N = 100$ and different noise standard deviations σ.

The effects of increasing the tool stiffness, κ, while keeping $N = 100$ on the response to a white Gaussian noise with constant $\sigma = 0.1$ is well illustrated in Fig. 2.27. For

smaller values of the stiffness, as it is anticipated, the response converges to the one observed with zero stiffness in sec. 2.4.1.2. It can also be concluded from Fig. 2.27 that increasing κ not only reduces the value of the hinge angle, but also limits the variation of θ by decreasing its standard deviation whereas for quite large values of the stiffness (plot with $\kappa = 0.1$), the hinge angle is quite small and the corresponding pdf is relatively narrow.

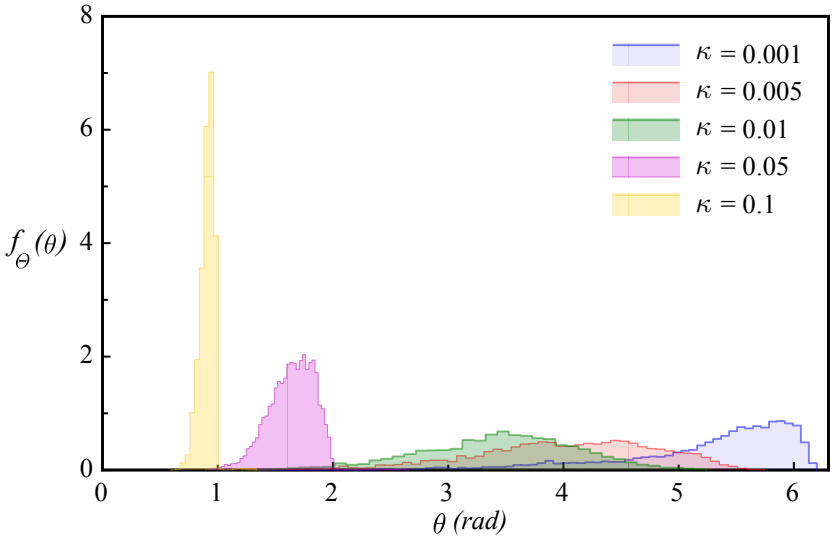

FIGURE 2.27: Pdf of the hinge angle for $N = 100$, $\sigma = 0.1$ and different values of tool stiffness κ.

Fig. 2.28 shows how increasing the legs length, N, affects the response of the "BBQ Tong" with $\kappa = 0.01$ to the white Gaussian noise with standard deviation of $\sigma = 0.1$. It can be inferred from the figure that increasing N has an effect on the tool response opposite to the effect of κ. Increasing N causes the tool legs to touch the signal at a further distance from the hinge. As a consequence, the right side of the tool equilibrium equation given by Eq. (2.7) increases, and since κ is given, θ must increase accordingly to keep the equilibrium equation satisfied. Hence, increasing N shifts the corresponding hinge angle pdf to the right in Fig. 2.28.

The parametric analysis up to this moment indicates that the way the pdf of the hinge angle is distributed around π (for a given N, κ and σ) is the key to predict how the response changes with a modification of either the tool specifications (N and κ) or the noise standard deviation (σ). Let us introduce P_1 (P_2) as the probability of the hinge angle being smaller (larger) than π. Thus,

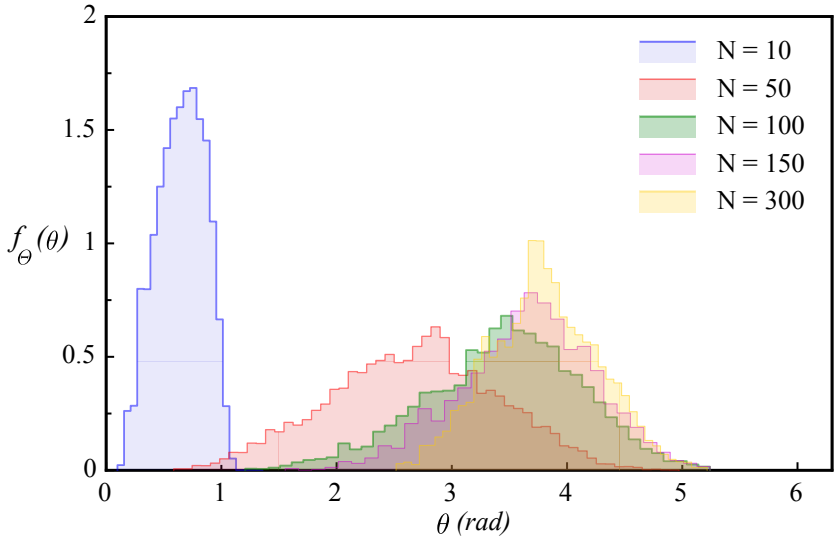

FIGURE 2.28: Pdf of the hinge angle for $\kappa = 0.01$, $\sigma = 0.1$, and different legs' length N.

$$P_1 = \int_0^{\pi} f_\Theta(\theta)\, d\theta, \qquad P_2 = \int_{\pi}^{2\pi} f_\Theta(\theta)\, d\theta. \tag{2.49}$$

The median of the hinge angle, $\tilde{\theta}$, is a relevant measure of the ratio between P_1 and P_2. When the median is equal to π, it simply means that $P_1 = P_2 = \frac{1}{2}$. Median values, $\tilde{\theta}$, below (over) π indicate that more (less) than fifty percent of the hinge angles are below (over) π or in other words, $P_1 > P_2$ ($P_1 < P_2$).

Fig. 2.29 shows the evolution of the median $\tilde{\theta}$ of the hinge angle with respect to the noise standard deviation for $N = 100$ and different values of the stiffness, $\kappa = 0.001$, 0.01, 0.03, 0.1 and 0.3. For lower stiffness values, the angle median converges towards 2π as the noise intensity increases. However, for high values of stiffness, the angle median is almost independent of the noise intensity.

As it was observed earlier, Fig. 2.29 also confirms that for moderate stiffness values, if $\tilde{\theta}$ is larger than π (example with $\kappa = 0.01$), increasing σ results in increasing $\tilde{\theta}$ (because the corresponding angle pdf moves to the right as it was illustrated in Fig. 2.25). However, when $\tilde{\theta}$ is smaller than π (example with $\kappa = 0.02$ and $\kappa = 0.03$), $\tilde{\theta}$ tends to decrease with increasing σ (because the corresponding angle pdf tends to move to the left as it was illustrated in Fig. 2.26).

The analytical derivation and the results shown in Fig. 2.29 suggest that there exists an optimum stiffness, κ_*, for which, the median of the hinge angle is always equal to π

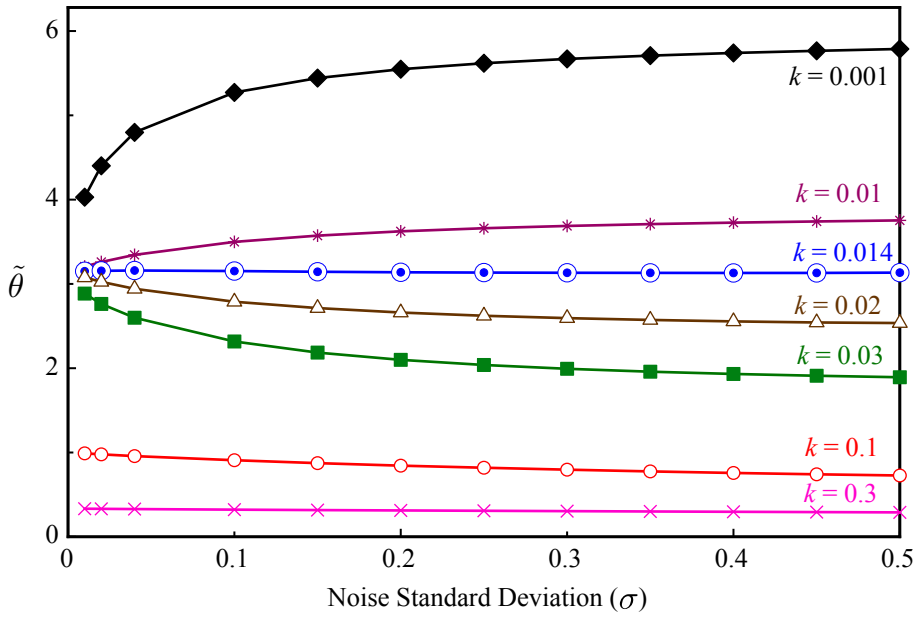

FIGURE 2.29: Median of the hinge angle for $N = 100$ and various κ versus noise standard deviation.

regardless of the noise intensity ($\kappa_* \simeq 0.014$ in the provided example). For any given legs length, N, a tool with such stiffness provides a response with $\tilde{\theta}$ independent of the noise standard deviation σ. Note that for moderate stiffness values, the probability density function of the angle is relatively symmetric. Thus, the mean value of the angle, $\bar{\theta}$, is approximately equal to the angle median, $\tilde{\theta}$, and thus similar conclusions can be drawn for the mean angle.

The evolution of the standard deviation of the hinge angle with respect to the noise standard deviation, σ, and given values of the stiffness ($\kappa = 0.001$, 0.01, 0.03, 0.1 and 0.3) is depicted in Fig. 2.30. Very large or very small values of stiffness result in having independent angle standard deviation by increasing the noise intensity (plots correspond to $\kappa = 0.001$ and $\kappa = 0.3$) whereas for moderate stiffness values, standard deviation of the hinge angle always increases with the noise intensity no matter if the angle median, $\tilde{\theta}$, is above or below π.

Interestingly, the optimum stiffness κ_* increases linearly with the legs length N as it is shown in Fig. 2.31. This means that computing κ_* for only one value of N is enough to make inferences about κ_* for any other values of N. Note that the coefficient of proportionality varies with the signal time step, indeed rescaling the signal x-coordinate affects the value of the equilibrium angle and therefore κ_*.

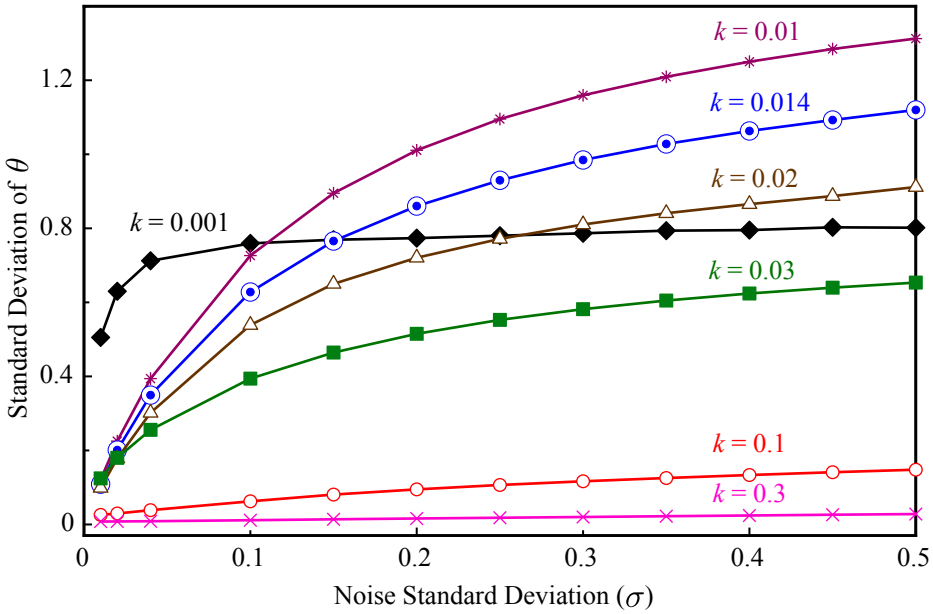

FIGURE 2.30: Standard deviation of the hinge angle for $N = 100$ and various κ versus noise standard deviation.

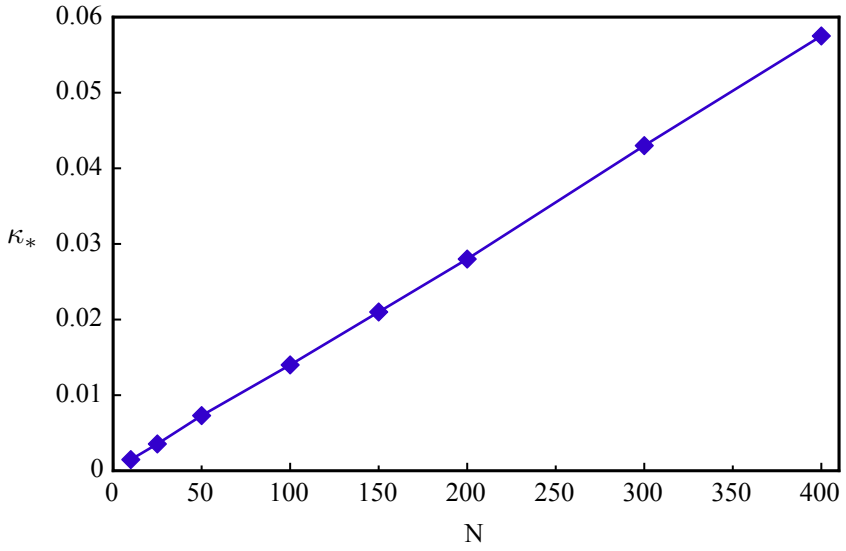

FIGURE 2.31: Evolution of κ_* with respect to N (T = 0.002 s).

As the desirable response of the tool for segmentation is considered as the one that provides the majority of the hinge angles around π, knowledge about κ_* for a given N, provides valuable information on the upper bound for selecting κ. This will be discussed in detail later on in sec. 2.6.

2.5.2 Noise Superimposed on Background Signal

With the noise being filtered with hinge angles close to π, the method relies on the sharpest peaks being identified as the smallest hinge angles (smaller than π). We consider again the three peaks described earlier in sec. 2.4.2 superimposed on white Gaussian noise. Each peak includes 200 data points equally spaced with $T = 0.002$ seconds. Note that the simulation for each peak and given tool specifications (legs length N and stiffness κ) and also noise standard deviation of σ is repeated for $30,000$ randomly created noise vector to draw statistical inferences.

The variable t_m is introduced as the position (time index) associated with the minimum hinge angle. The histogram of the computed t_m over $30,000$ runs (the time index of the minimum angle at each run is identified and stored in t_m) for $N = 100$, $\kappa = 0.01$ and various peak styles and noise standard deviation is shown in Fig. 2.32. As the noise intensity increases, the precision in the location of the identified break-point position drops. The pdf of the break-point position widens around the true position (peak apex) as the peak angle lessens and approaches π.

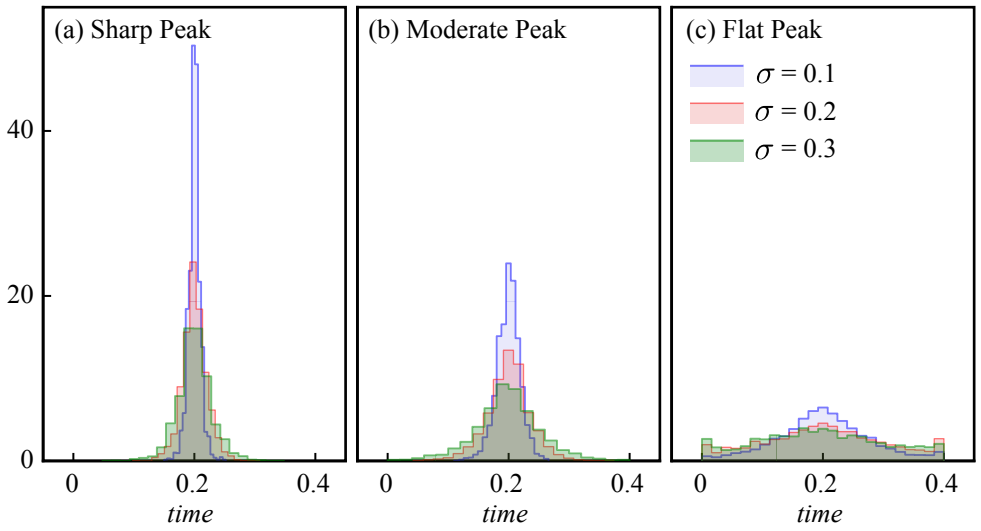

FIGURE 2.32: Histogram of the position of the minimum hinge angle for $N = 100$, $\kappa = 0.01$ and various noise intensities.

Again, the variable γ is defined as the ratio of the standard deviation of t_m to the width of the background peak (equal to 0.4 seconds in the examples). The evolutions of γ with respect to the noise standard deviation, σ, for $N = 100$ and various peak styles and tool stiffness values, κ, is illustrated in Fig. 2.33. Similar to the results obtained in

sec. 2.4.2, it can be inferred from the figure that increasing the noise standard deviation is followed by a rise in the standard deviation of t_m. However, the rate of increase in γ is reduced by considering the transition from "Flat" to "Sharp" peak style. Furthermore, Fig. 2.33 indicates that for a given σ, increasing the tool stiffness slightly decreases the dispersion of the identified break-point around the peak apex (true break-point) for sharp and moderate peak styles. However, it also implies that the selection of κ is not limited to a single value, and a valid stiffness interval exists such that, for any κ within this interval, similar results in terms of the dispersion of the position of the identified break-point around the true break-point are observed.

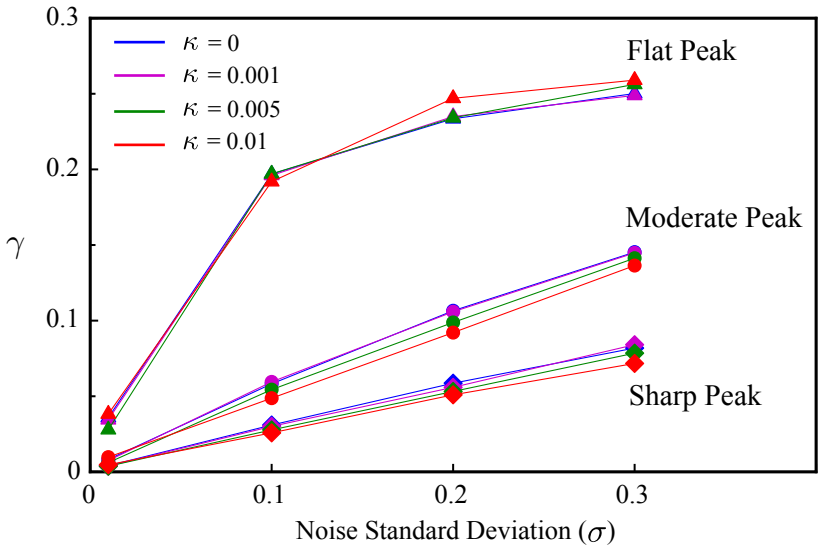

FIGURE 2.33: Standard deviation of t_m scaled by the peak width (γ), with respect to noise standard deviation (σ) for $N = 100$ and various peak style and κ.

The standard deviation of the position associated with minimum angle, t_m, normalised by the peak width (γ), with respect to the noise standard deviation, σ, for $\kappa = 0.01$ and various peak styles and legs length, N, is depicted in Fig. 2.34. Alike results obtained with zero stiffness, increasing N always reduces γ regardless of the peak style. However, increasing N, on the other hand, increases the computational efforts. Therefore, selecting N is a trade-off between the quality of the approximation and the computational time.

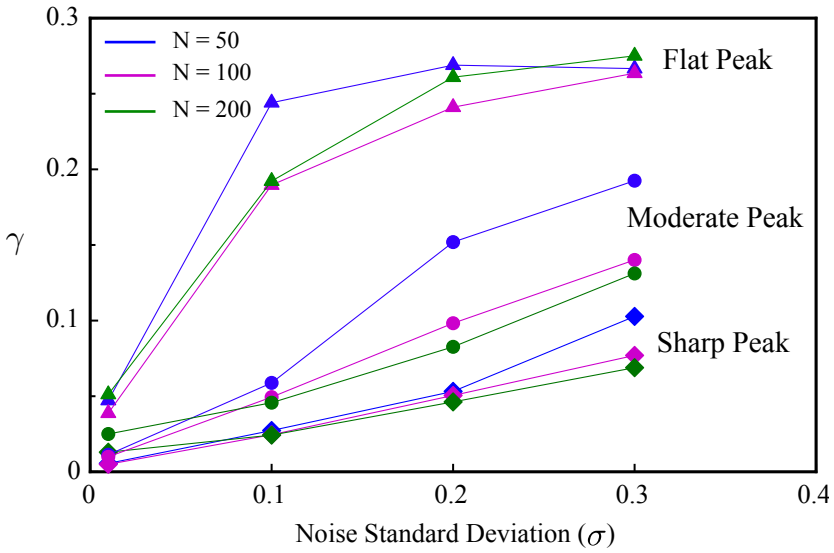

FIGURE 2.34: Standard deviation of t_m scaled by the peak width (γ), with respect to noise standard deviation (σ) for $\kappa = 0.01$ and various peak style and N.

2.6 Summary

The final objective of this chapter is to provide guidance on how to select the appropriate "BBQ Tong" properties to segment a given signal with known noise statistical properties.

The upper band for the tool length, N is related to the minimum segment length the user would like to observe no matter if a tool with or without stiffness is used. In fact, selecting N more than the minimum segment length may result in missing those segments shorter than N in the final approximation.

When a tool with zero stiffness is used, to reduce the number of redundant points being identified by the tool, it is recommended to choose N as large as possible. Although, increasing N results in more computational time, however, as there is no need to solve any equilibrium equation (hinge sits on the signal all the times), the additional computation effort is not detrimental. The value of N can be reduced if the method is supported by a merging algorithm.

When using a tool with non-zero stiffness, for any selected value of N, the upper band for stiffness is given by κ_*. It is recommended to choose κ smaller than κ_*. The response of the "BBQ Tong" with stiffness $\kappa*$ to a white Gaussian noise incorporates fifty percent of the angles below π. Selecting κ smaller than κ_* not only decreases the

number of hinge angles below π, but also results in increasing the value of the minimum angles and therefore, less interferences with the background peaks are observed.

The lower band for selecting N is a trade-off between the approximation quality and computational efficiency of the proposed algorithm. As discussed earlier, increasing N results in better approximation at the expense of the computational efforts.

Chapter 3

Numerical Experiments

3.1 Introduction

The objective of this Chapter is to apply the proposed method to various synthetic signals and field drilling data and to compare the performance (error and computation time) with two methods proposed in the literature: the dynamic programming (DP) algorithm introduced by Kehagias et. al. [72] and the span window method developed by Liu et al. [69]. The examples consist of synthetic piece-wise linear time series corrupted by a white noise with zero mean and a standard deviation of σ, we also consider non-stationary noise with varying standard deviation. The field data examples including surface hook position, downhole weight on bit and torque on bit recordings are also considered for segmentation.

The segmentation procedure presented by Kehagias et. al. is based on the minimization of Huberts segmentation cost [95] or various generalizations of this cost which is performed by way of a dynamic programming algorithm. As a result, a globally optimal approximation for any number of the break-points is achieved. It is also possible to speed up the basic dynamic programming algorithm by means of a recursive computation of segment errors and block segmentation.

The feasible span window (FSW) segmentation algorithm is an on-line technique which introduces a maximum vertical distance as a measure for adding a new segment. A point is labelled a Candidate Segmenting Point (CSP) if it may be selected to be the next eligible point included in the segment, i.e. the distances of all the points lying between the last segmenting point and the new chosen one to the new interpolating

line are all within the maximum error tolerance. The key idea of the FSW technique is to search for the farthest CSP to make the current segment as long as possible under the given maximum error tolerance.

The symbols used for illustrating the results of different segmentation methods are DP for "Dynamic Programming" [72], SW for "Feasible Sliding Window" [69] and BT for "BBQ Tong" algorithm.

All the three methods were implemented under Matlab R2008b (7.7.0.471) and run on MacBook Pro with an Intel Core i5 processor (2.4 GHz) and 4 Gb of memory. Results were compared in terms of the computation time and error defined as the sum of square residuals normalized by the number of the time series data points. For the examples of synthetic time series, the error is obtained with respect to either original piece-wise linear signal or noisy synthetic signal as follows

$$SSE_1 = \frac{1}{n}\sum_{k=1}^{n}(x[k] - \hat{x}[k])^2, \quad SSE_2 = \frac{1}{n}\sum_{k=1}^{n}(x_\epsilon[k] - \hat{x}[k])^2, \tag{3.1}$$

where n is the number of data points in the signal, x is the synthetic piece-wise linear signal, x_ϵ is the synthetic signal corrupted by white Gaussian noise and $\hat{x}$ is the approximation of the noisy synthetic signal obtained with any of the segmentation techniques discussed earlier in this chapter. For the examples of drilling data segmentation, only SSE_2 error is computed as the original underlying trend of the signal is unknown a priori.

Before the results are presented and discussed, a first section is devoted to the numerical implementation of the "BBQ Tong" method for piece-wise linear segmentation. The algorithm but also a method to detect and eliminate outliers (detrimental to the identification of break-points) are described.

In the first three examples, we compare the DP and SW methods with the iterative BT method ($k \neq 0$) considering the number of break-points as the stopping criteria (In the case of the sliding window method, the tolerance error was selected as to produce the requested number of break-points). The three examples are presented by increasing the order of complexity, starting with a 2 break-points signal with sharp peaks, followed by a 6 break-points signal with sharp, medium and flat peaks, and segments of identical lengths, while the last example includes 29 break-points with segments of various lengths.

Next, the "BBQ Tong"algorithm with zero stiffness ($k = 0$) is implemented on the three examples and the results are compared with the three other methods in terms of error but also numbers of segments as in this method, the number of segments is not set a priori.

Finally, a few examples including the piece-wise linear approximation of various field drilling data (surface and downhole), in particular, hook position (resulting the rate of penetration estimation), weight on bit and torque on bit measurements using the three segmentation techniques are provided and the performance of the proposed methods is evaluated in terms of the computational efforts.

3.2 Numerical Implementation

3.2.1 Management of Outliers

As it was well illustrated in the previous chapter, the noise superimposed on the signal affects the tool response that is in fact particularly sensitive to outliers. Not only outliers can be wrongly identified as break-points by the method, but their presence near a true break-point can cause the method to miss the break-point. It is therefore necessary to detect and remove detrimental outliers. The method used to remove outliers relies on the "BBQ Tong" with zero stiffness.

An example of a significant outlier which has a considerable effect on the hinge angle signal is provided in Fig. 3.1. Because of the presence of the outlier, the minimum hinge angle sits at a position quite different from the true break-point position, (see the plot labelled "Angle (Method 1)" in Fig. 3.1 (c)).

A simple algorithm based on the hinge left and right angles computed using "BBQ Tong" with zero stiffness at each iteration has been developed to detect such detrimental effect of outliers. As it was discussed in sec. 1.3, when $\kappa = 0$, the hinge is positioned on the residual signal and each leg covers N points on each side of the hinge. In the ideal case, we expect $\theta_i(\theta_j)$, the hinge left (right) angle (for each point on the signal covered by the left leg and $1 \leq i \leq N$) to be less than $\frac{\pi}{2}$ whenever the hinge ascends (descends) the peak. The points yielding hinge angles that do not satisfy this inequality are classified as outliers and will be excluded from the angle computation process.

Note that when the signal is corrupted by noise, the above criteria is not always valid, in particular when the hinge sits in a valley. The criteria is usually satisfied when

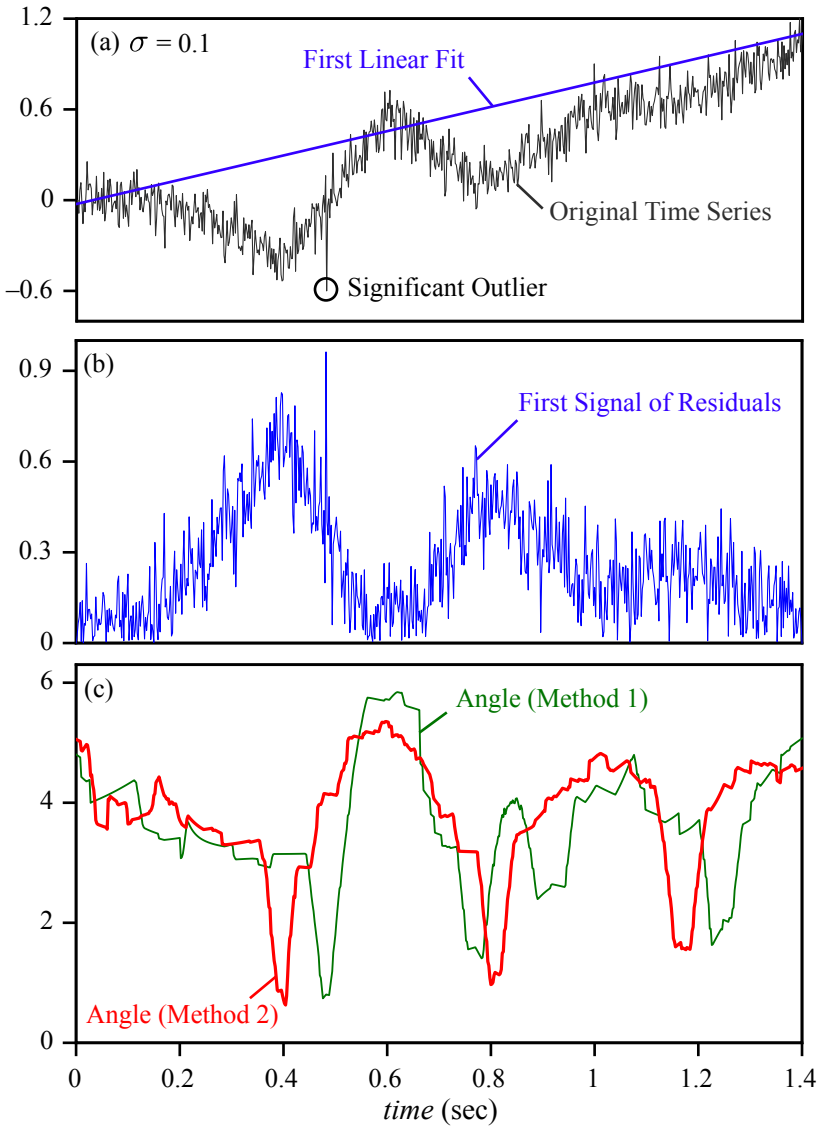

FIGURE 3.1: (a) Original time series and its first linear fit. (b) First signal of residuals. (c) Hinge angle obtained with and without activating outlier detection algorithm.

the hinge sits on the local peaks. Most often, those local peaks are enough to capture the outliers as long as the outliers are covered by either of the legs.

In practice, the average left (right) angles when the tool ascend (descend) a peak are computed as

$$\bar{\theta}_L = \frac{1}{N}\sum_{i=1}^{N}\theta_i, \qquad \bar{\theta}_R = \frac{1}{N}\sum_{j=1}^{N}\theta_j. \tag{3.2}$$

At any given position of the hinge over the signal, if $\bar{\theta}_L$ or $\bar{\theta}_R$ is found less than $\frac{\pi}{2}$, every point with θ_i or θ_j larger than $\frac{\pi}{2}$ is excluded from the computation.

The plot labelled "Angle (Method 2)" in Fig. 3.1 (c) shows the angle sequence

computed over the residual signal using the outlier detection algorithm described above. The decision about activating the outlier detection algorithm for the segmentation can be made by considering the intensity of the noise over the time series. It is usually not required when the noise intensity is not to high.

The histogram of the position of the break-point for the three peak example introduced in sec. 2.4.1.2 and corrupted with white Gaussian noise with standard deviation of 0.1 using "BBQ Tong" segmentation algorithm with and without outlier detection procedure is presented in Fig. 3.2. It can be inferred from the figure that using outlier detector prior to the segmentation process increases the chance of detecting the break-point closer to the true break-point position even for the flat peak example.

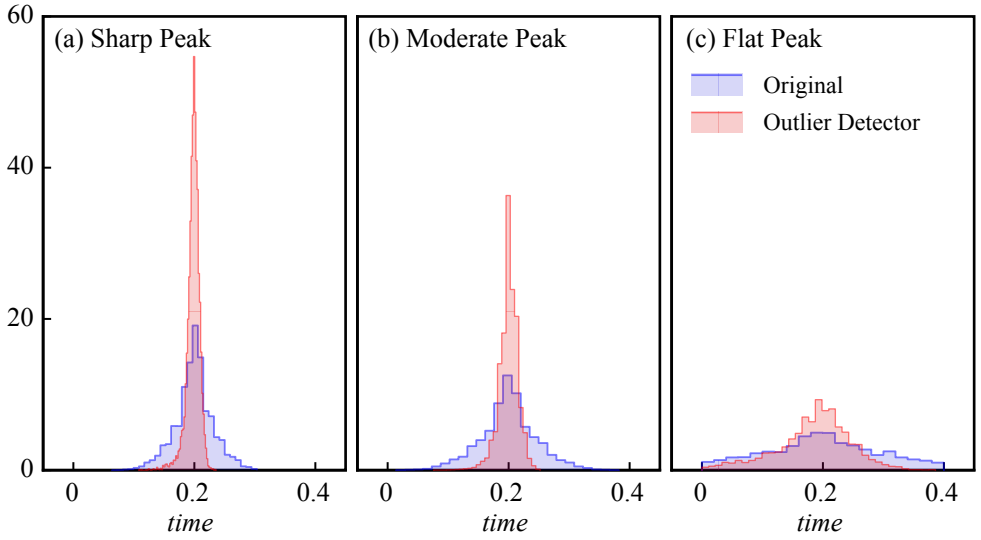

FIGURE 3.2: Histogram of the position of the hinge angles below π for $N = 100$ and $\sigma = 0.1$ with and without outlier removal algorithm.

3.2.2 Algorithm

As it was well described in sec. 1.3, the "BBQ Tong" algorithm can either be implemented with non-zero stiffness within an iterative procedure or with zero stiffness and only two iterations. The former method only provides one break-point at every iteration while the latter detects all the break-point at the first two iterations.

When the tool with non-zero stiffness is used for the segmentation, two distinct strategies can be followed to detect the new break-point at each iteration. The first strategy consists in selecting the point with minimum hinge angle all over the updated

angle sequence as the most triangular peak. If following the second strategy, the mean squared error (SSE_2) of each segment is computed at each iteration and the new break-point is recognized as the one with minimum angle over the segment with maximum error. The advantage of the second strategy is that the total segmentation error at each iteration decreases much faster compare to the first one. In the examples provided later, examples 1 and 2 follow the first strategy while example 3 and all the examples of the drilling data segmentation follow the second strategy.

3.3 Non-zero Stiffness

3.3.1 Example 1

The first example concerns a time series with three distinct linear sections separated by one valley and one peak both characterised by a sharp angle, see Fig. 3.3 (a)). The signal varies between 0 and 1, and consists of 500 data points with a time step $T = 0.002$ seconds. The coordinates of the two break-points and two end points are given in Table. 3.1.

Break-Point No	1	2	3	4
x coordinate	0	0.286	0.571	1
y coordinate	0.867	0.533	1	0

TABLE 3.1: x and y coordinates of the original piece-wise linear time series - Example 1.

A white Gaussian noises with different intensity (σ = 0.01, 0.02, 0.04, 0.1, 0.2 and 0.3) were superimposed on the original sawtooth time series. We also consider two examples with non-stationary noise with intensity varying linearly over the time window from $\sigma = 0.01$ to $\sigma = 0.2$ and $\sigma = 0.3$. The specifications of the "BBQ Tong" (κ and N) for each case are summarised in Table. 3.2. The piece-wise linear approximations resulting from the segmentation performed using DP, SW and BT techniques are illustrated in Figs. 3.3 and 3.4.

For stationary noise, the three segmentation methods provide very similar approximations for the lower noise intensities ((a), (b) and (c)), however, the results differ at higher noise intensities as each method relies on different signal characteristics to

	σ	κ	**N**
(a)	0.01	0.003	10
(b)	0.02	0.005	20
(c)	0.04	0.007	30
(d)	0.1	0.009	60
(e)	0.2	0.009	70
(f)	0.3	0.010	100
(g)	0.01-0.2	0.010	120
(h)	0.01-0.3	0.010	130

TABLE 3.2: "BBQ Tong" specifications, κ and N, for various noise standard deviations, σ - Example 1.

detect the break-points.

In the case on non-stationary noise, the DP algorithm provides a good estimate as the approximation with minimum error (SSE_2) is guaranteed by this method regardless of the noise properties [72]. For the SW method, the maximum vertical distance criteria (error criteria) is not well suited for the non-stationary noise. Increasing the error results in missing the break-points in the low noise intensity regions while decreasing the error creates over fragmentation in regions with higher noise intensity. The example also shows that the BT algorithm appears to be "adaptable" to the variation of the noise intensity due to its inherent filtering property.

The run-time and errors (SSE_1 and SSE_2 given by Eq. (3.1)) associated with each of the three segmentation techniques i.e. Dynamic Programming (DP), Sliding Window (SW) and BBQ Tong (BT) for the above examples are provided in Table. 3.3.

The results imply that there is no significant variation in the error (SSE_2) of each segmentation method when the noise is stationary (see also Fig. 3.5). The error computed by DP has usually the minimum value as the model selection is based on the minimum error for a given number of segments [72]. For the given examples, as shown in Table. 3.3, the error computed by the BT method lies within the error generated by the DP and SW algorithms. However, the segmentation results of the time series with non-stationary noise shows that unlike SW, the BT algorithm performs well while providing the approximation with quality similar to the DP method.

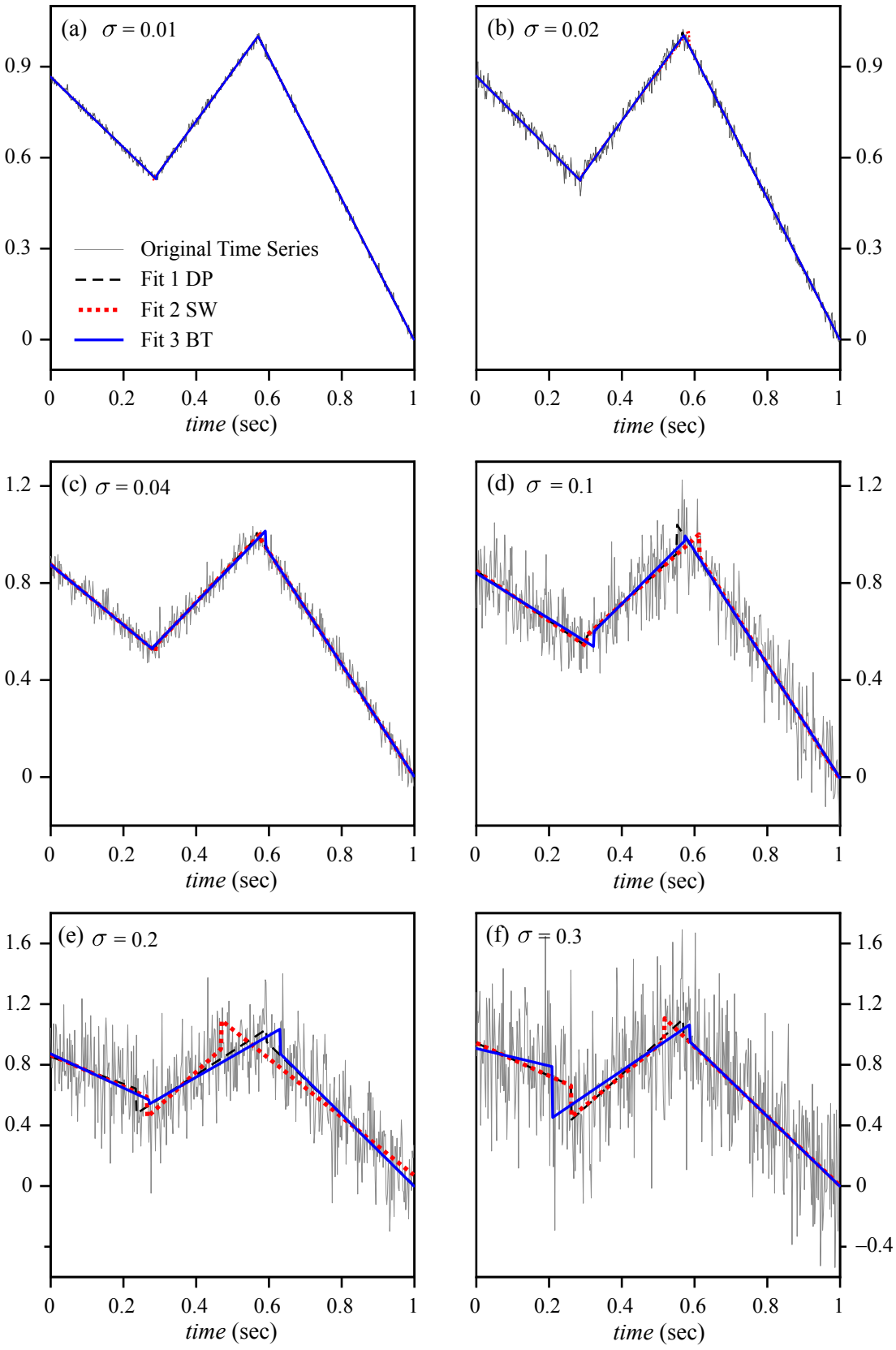

FIGURE 3.3: Time series corrupted by noise with various intensities and the piece-wise linear approximation using the three different segmentation techniques - Example 1.

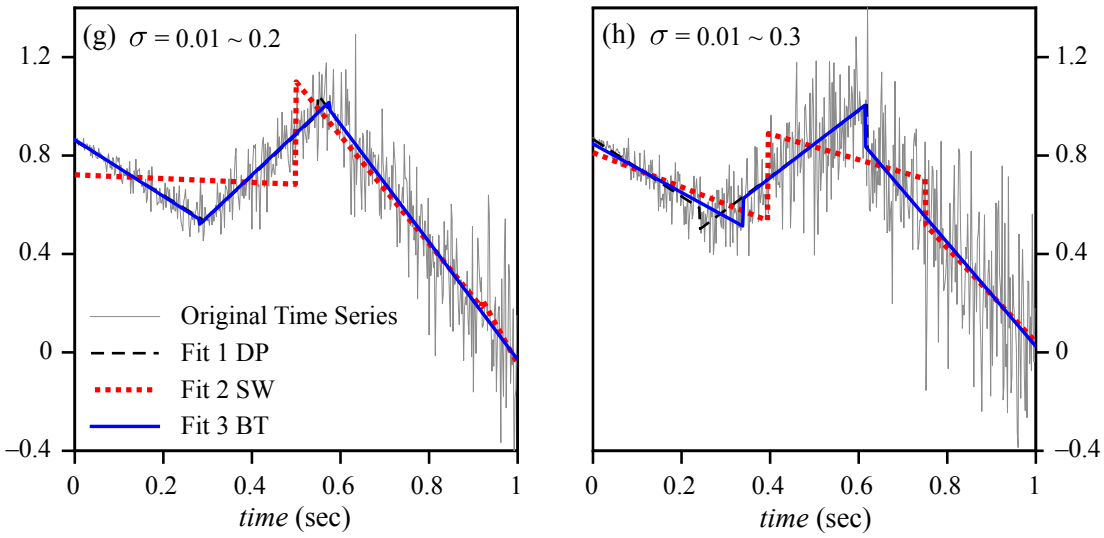

FIGURE 3.4: Artificial time series corrupted by time varying noise and the piece-wise linear approximation using different segmentation techniques - Example 1.

	DP			**SW**			**BT**		
	RT	**SSE$_1$**	**SSE$_2$**	**RT**	**SSE$_1$**	**SSE$_2$**	**RT**	**SSE$_1$**	**SSE$_2$**
(a)	4.14	8.23E-7	8.67E-5	2.17	4.02E-7	8.69E-5	0.96	7.34E-7	8.65E-5
(b)	4.04	9.26E-6	3.72E-4	2.20	2.22E-5	3.85E-4	1.15	7.93E-6	3.72E-4
(c)	3.78	2.00E-5	0.0015	2.22	2.07E-5	0.0015	1.26	5.57E-5	0.0015
(d)	3.87	2.26E-4	0.0099	2.67	3.80E-4	0.01	1.38	2.19E-4	0.0099
(e)	3.88	4.59E-4	0.0385	2.76	0.0033	0.0416	1.42	7.52E-4	0.0394
(f)	3.99	0.0030	0.0861	2.37	0.0030	0.0869	1.78	0.0037	0.0869
(g)*	4.07	1.60E-4	0.0129	2.86	0.0061	0.0184	2.43	1.09E-4	0.0129
(h)*	4.05	8.30E-4	0.0279	2.97	0.0056	0.0315	2.53	9.36e-4	0.0279

TABLE 3.3: Run-time (RT) in seconds and error (SSE_1 and SSE_2 given by Eq. (3.1)) associated with each segmentation method - Example 1 ((*) denotes outlier detector activation).

Table. 3.3 also shows the running time for each segmentation technique. The results are also displayed in Fig. 3.5 for comparison purposes. It can be inferred from the given example that the BT algorithm outperforms the other two techniques by reducing the computational effort remarkably.

Fig. 3.5 also denotes that the computational effort of the DP and SW methods

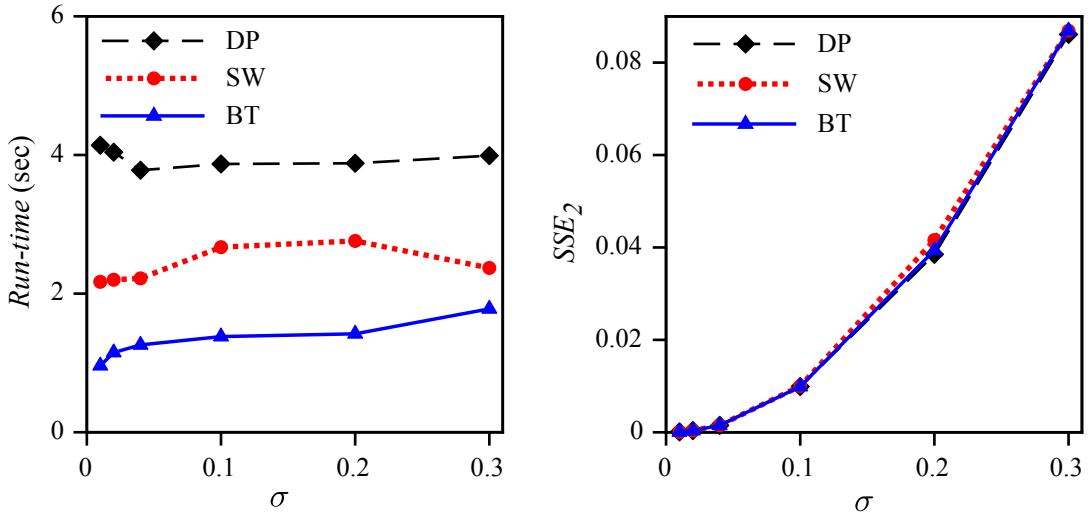

FIGURE 3.5: Run-time and error comparison - Example 1.

are nearly independent of the noise intensity. Nevertheless, the BT algorithm run-time grows as the noise intensity increases. This can be explained by the fact that for higher values of the noise standard deviation, σ, larger R (N) needs to be selected, which in turn results in an increase of the run-time. Furthermore, outlier detection algorithm, if activated (Table. 3.3 (g) and (h)), can increase the run-time as well. Yet, Table. 3.3 indicates that the overall performance of the BT algorithm is quite effective.

3.3.2 Example 2

The second example is a synthetic signal with 700 data points and the time step of $T = 0.002$ seconds (Fig. 3.6). The signal includes seven linear segments (six break-points) and incorporates sharp, moderate and flat peaks (valleys). Coordinates of the six break-points and two end points are given in Table. 3.4.

Break-Point No	1	2	3	4	5	6	7	8
x coordinate	0.0	0.2	0.4	0.6	0.8	1.0	1.2	1.4
y coordinate	0.005	-0.013	-0.389	0.534	0.123	0.598	0.706	1

TABLE 3.4: x and y coordinates of the original piece-wise linear time series - Example 2.

A white Gaussian noise with different standard deviations ($\sigma = 0.01$, 0.05, 0.1 and 0.2) was superimposed on the original time series. We also considered a non-stationary

noise with intensity increasing linearly over the length of the signal from $\sigma = 0.01$ to $\sigma = 01$. The "BBQ Tong" specifications (κ and N) for different σ is given by Table. 3.5. The results of the linear segmentation using DP, SW and BT segmentation techniques are displayed in Figs. 3.6 to 3.10.

	σ	κ	**N**
(a)	0.01	0.006	25
(b)	0.05	0.008	90
(c)	0.1	0.009	90
(d)	0.2	0.010	100
(e)	0.01-0.2	0.008	100

TABLE 3.5: "BBQ Tong" specifications, κ and N, for various noise standard deviations, σ - Example 2.

Like in the previous example, Figs. 3.6 and 3.7 indicate that the three methods come up with indistinguishable approximations for the lower noise intensities. But the approximations diverge as the noise standard deviation increases, see Figs. 3.8, 3.9 and 3.10.

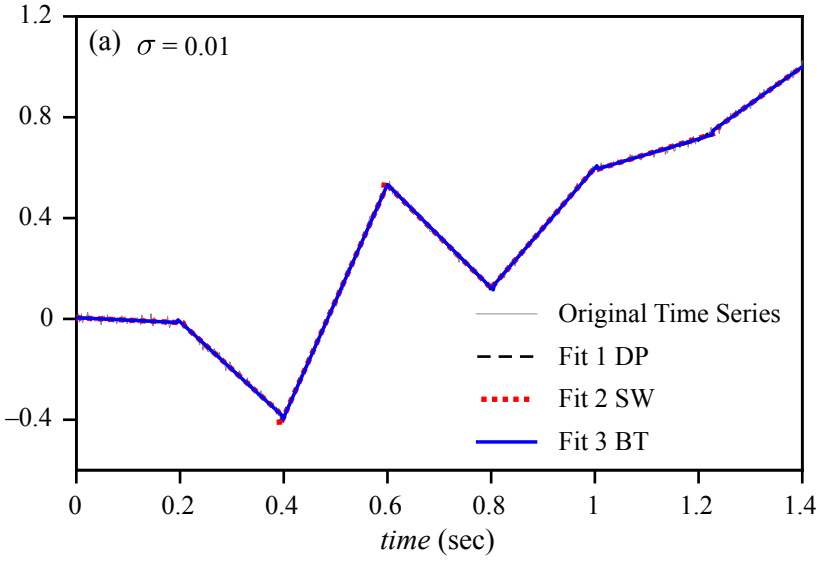

FIGURE 3.6: Synthetic time series with noise standard deviation of $\sigma = 0.01$ and its piece-wise linear approximations using DP, SW and BT algorithms - Example 2.

The results with non-stationary noise are depicted in Fig. 3.10.

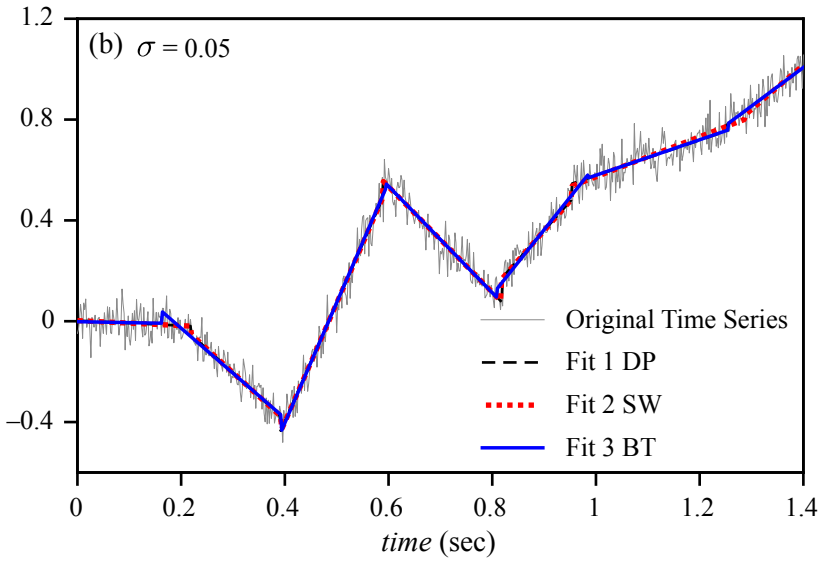

FIGURE 3.7: Synthetic time series with noise standard deviation of $\sigma = 0.05$ and its piece-wise linear approximations using DP, SW and BT algorithms - Example 2.

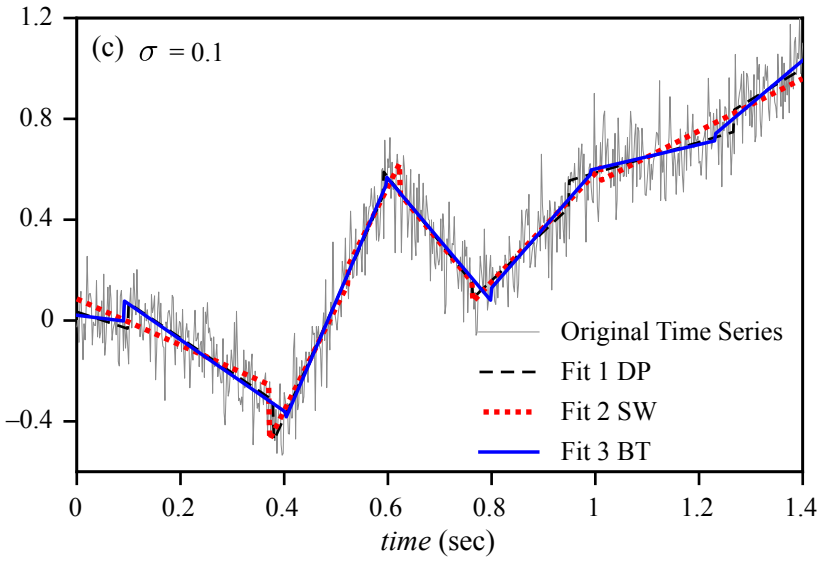

FIGURE 3.8: Synthetic time series with noise standard deviation of $\sigma = 0.1$ and its piece-wise linear approximations using DP, SW and BT algorithms - Example 2.

The run-time and error (SSE_1 and SSE_2 given by Eq. (3.1)) associated with each of the three segmentation techniques are summarised in Table. 3.6 and shown in Fig. 3.11. Once more, the error (SSE_2) from the BT algorithm stands between the error from the DP and the SW techniques but yields faster computation time.

Note that when the outlier detection algorithm is activated (Table. 3.6 (b), (c) and

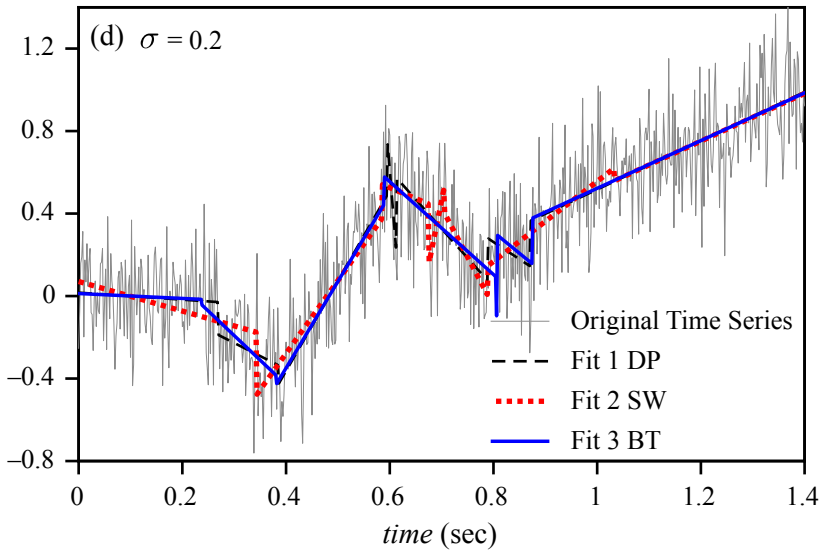

FIGURE 3.9: Synthetic time series with noise standard deviation of $\sigma = 0.2$ and its piece-wise linear approximations using DP, SW and BT algorithms - Example 2.

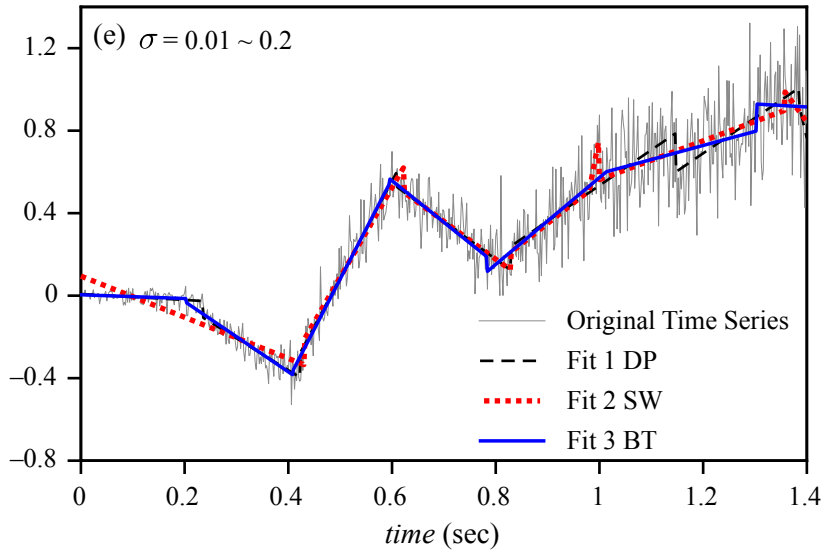

FIGURE 3.10: Synthetic time series with non-stationary noise and its piece-wise linear approximations using DP, SW and BT algorithms - Example 2.

(d)), run-time increases basically by a factor of two. However, the run-time comparison in Table. 3.6 indicates that the BT method still performs faster than the DP and SW algorithms.

	DP			SW			BT		
	RT	**SSE$_1$**	**SSE$_2$**	**RT**	**SSE$_1$**	**SSE$_2$**	**RT**	**SSE$_1$**	**SSE$_2$**
(a)	7.60	2.70E-6	9.45E-5	5.22	1.84E-5	1.08E-4	2.42	5.22E-6	9.78E-5
(b)*	7.71	1.31E-4	0.0025	5.91	1.42E-4	0.0025	4.63	9.43E-5	0.0025
(c)*	7.61	7.00E-4	0.0106	5.55	0.0013	0.0114	4.65	4.40E-4	0.0107
(d)*	7.61	0.0018	0.0389	5.84	0.0024	0.0400	4.44	0.0011	0.0392
(e)	7.64	0.0012	0.0142	6.47	0.0017	0.0153	3.76	4.30E-4	0.0145

TABLE 3.6: Run-time (RT) in seconds and error (SSE_1 and SSE_2 given by Eq. (3.1)) associated with each segmentation method - Example 2 ((*) denotes outlier detector activation).

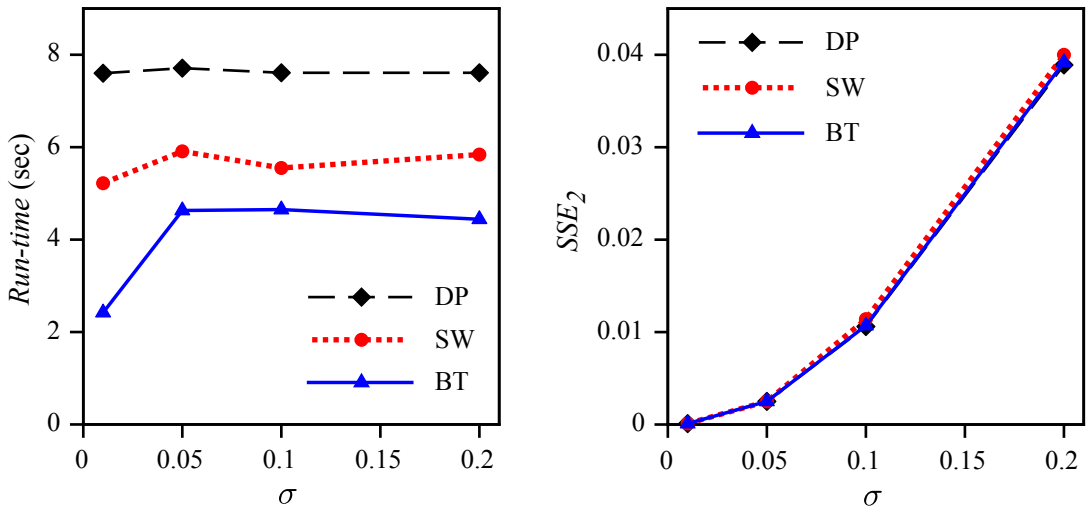

FIGURE 3.11: Run-time and error comparison - Example 2.

3.3.3 Example 3

The third example is a longer time series including 5000 data points with a time step of $T = 0.002$ seconds, but again normalised between 0 and 1 (Fig. 3.12). The signal includes 30 linear segments (29 break-points) with different lengths and incorporates several sharp, moderate and flat peaks (valleys). A white Gaussian noise with various standard deviations ($\sigma = 0.01$, 0.05, 0.1 and 0.2) was superimposed on the original time series. The "BBQ Tong" specifications (κ and N) for different σ is given by Table. 3.7. The results of the linear approximation using the three segmentation techniques are illustrated in Figs. 3.12 to 3.15.

	σ	κ	**N**
(a)	0.01	0.007	80
(b)	0.05	0.009	70
(c)	0.1	0.010	100
(d)	0.2	0.014	120

TABLE 3.7: "BBQ Tong" specifications, κ and N, for various noise standard deviations, σ - Example 3.

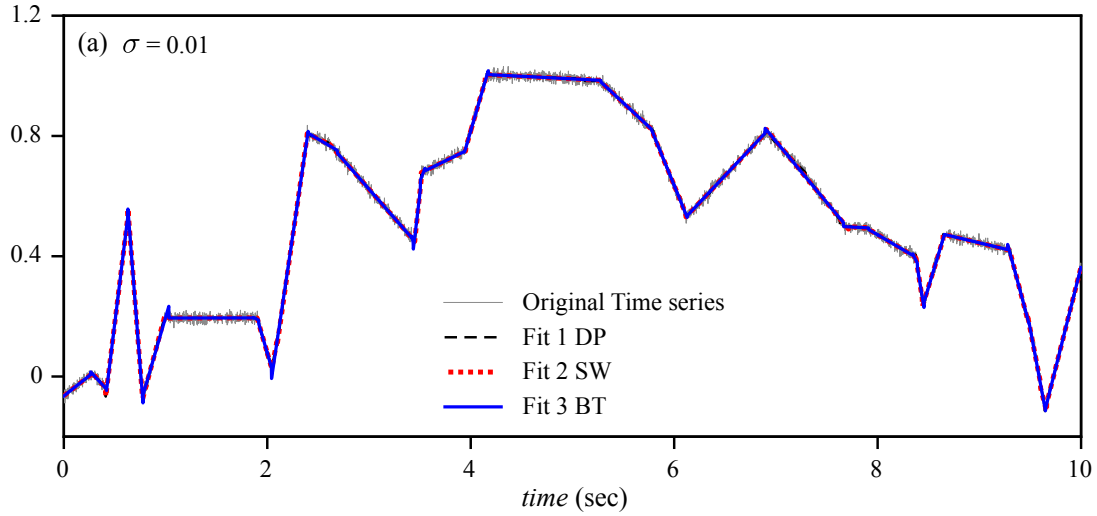

FIGURE 3.12: Synthetic time series with noise standard deviation of $\sigma = 0.01$ and its piece-wise linear approximations using DP, SW and BT algorithms - Example 3.

The run-time and error (SSE_1 and SSE_2 given by Eq. (3.1)) associated with each of the three segmentation techniques are provided in Table. 3.8 and shown in Fig. 3.16. Again, although the output errors (SSE_2) are quite comparable, the BT algorithm still outperforms the two others in terms of speed. It is interesting to see that the computational complexity of the DP algorithm is growing drastically with the increases of the signal length.

3.4 Zero Stiffness

The "BBQ Tong" method can also be implemented in a non-iterative fashion using the tool with zero stiffness as discussed in detail in sec. 1.3. Although referred as non-iterative, the method does actually require two iterations, the second being necessary

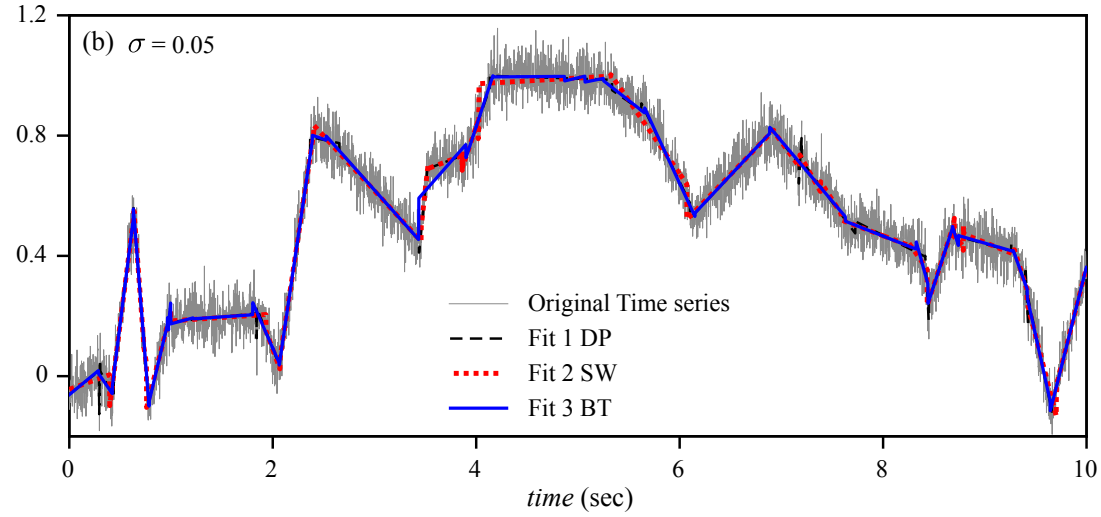

FIGURE 3.13: Synthetic time series with noise standard deviation of $\sigma = 0.05$ and its piece-wise linear approximations using DP, SW and BT algorithms - Example 2.

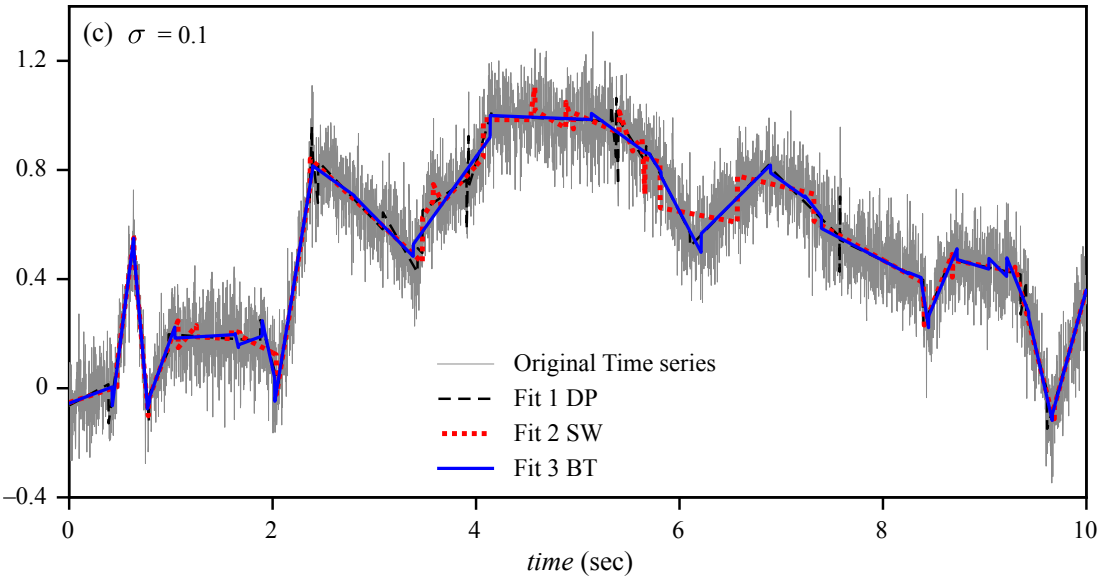

FIGURE 3.14: Synthetic time series with noise standard deviation of $\sigma = 0.1$ and its piece-wise linear approximations using DP, SW and BT algorithms - Example 3.

to capture break-points associated with valleys in the first iteration. In this method, the points with hinge angle below π are identified as break-points. In the case of zero stiffness, there is no need to solve the equilibrium equation as the hinge always sits on the residual signal and as a result, the method performs considerably faster. However, depending on the leg length N, the method might lead to over fragmentation as it will detect some points which are not necessarily break-points. To illustrate how the

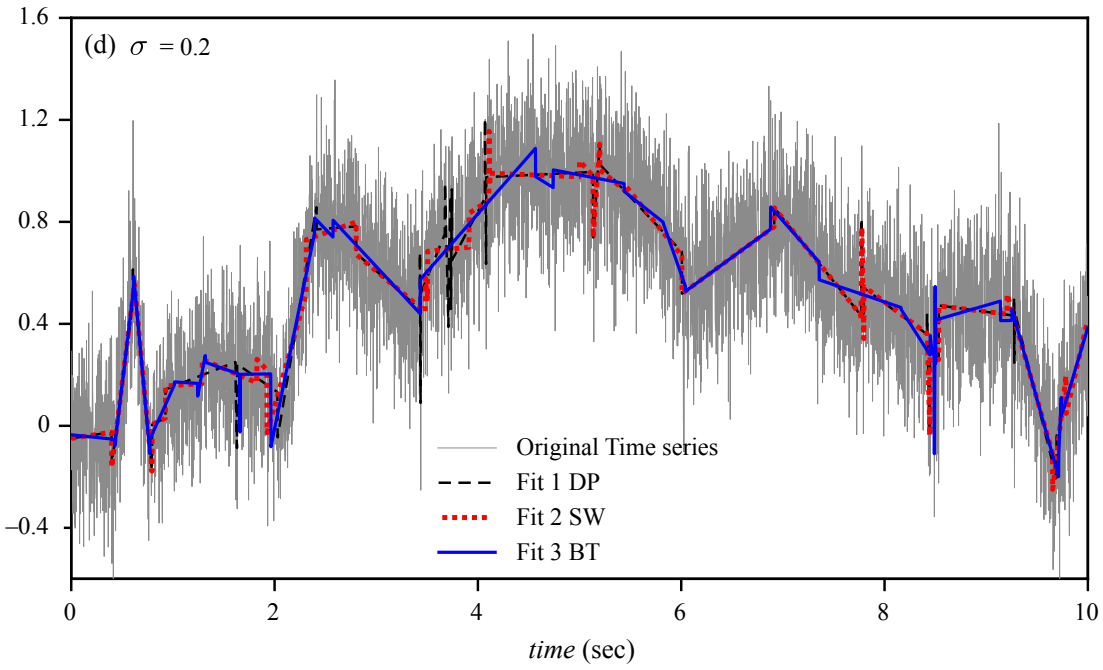

FIGURE 3.15: Synthetic time series with noise standard deviation of $\sigma = 0.2$ and its piece-wise linear approximations using DP, SW and BT algorithms - Example 3.

	DP			**SW**			**BT**		
	RT	**SSE$_1$**	**SSE$_2$**	**RT**	**SSE$_1$**	**SSE$_2$**	**RT**	**SSE$_1$**	**SSE$_2$**
(a)	430.31	3.45E-6	1.02E-4	41.32	6.22E-6	1.06E-4	26.1	8.97E-6	1.09E-4
(b)	421.76	9.84E-5	0.0025	41.29	2.47E-4	0.0026	24.76	1.54E-4	0.0026
(c)	424.12	3.70E-4	0.0097	47.08	7.70E-4	0.0102	22.63	4.86E-4	0.0101
(d)	410.02	0.0013	0.0395	48.22	0.0014	0.0398	21.85	0.0016	0.0404

TABLE 3.8: Run-time (RT) in seconds and error (SSE_1 and SSE_2 given by Eq. (3.1)) associated with each segmentation method - Example 3.

algorithm performs with this method, the three examples presented in the previous section are also segmented using "BBQ Tong" algorithm with zero stiffness .

The number of break-points (NoB), run-time and error (SSE_1 and SSE_2 given by Eq. (3.1)) associated with the "BBQ Tong" segmentation algorithm using zero stiffness and $N = 150$ for the first example (see sec. 3.3.1) are provided in Table. 3.9. The results indicate a significant improvement in run-time, with a decrease of the run-time by a factor as high as four for the signal with higher noise intensity. However, the

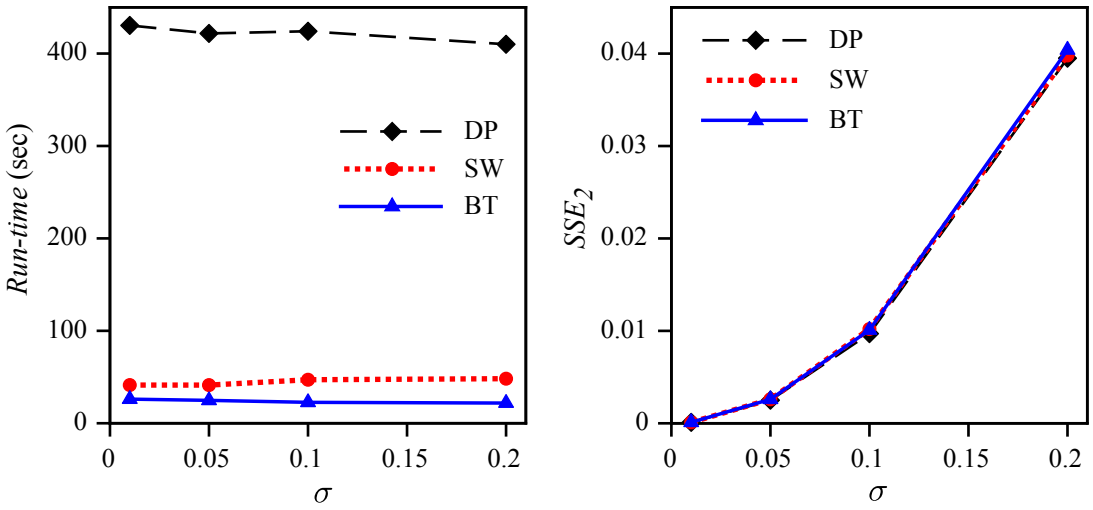

FIGURE 3.16: Run-time and error comparison - Example 3.

number of break-points has also increased.

σ	**NoB**	**Run-time**	**SSE$_1$**	**SSE$_2$**
0.01	7	0.50	1.38E-6	8.52E-5
0.02	5	0.50	1.12E-5	3.72E-5
0.04	5	0.50	3.97E-5	0.0015
0.1	5	0.50	2.92E-4	0.0098
0.2	4	0.50	0.0012	0.0390
0.3	6	0.50	0.0062	0.0860
0.01-0.2*	4	0.89	1.85E-4	0.0129
0.01-0.3*	5	0.88	0.0015	0.0268

TABLE 3.9: Number of break-points (NoB), run-time (in seconds) and error (SSE_1 and SSE_2 given by Eq. (3.1)) of the BT method with $\kappa = 0$ - Example 1 ((*) denotes outlier detector activation).

Note that the results for signals with non-stationary noise are obtained after activating the outlier detection algorithm. Fig. 3.17 shows the results of segmentation performed on the data relative to example 1 using the tool with non-zero stiffness.

Segmentation results for the second example considering $N = 100$ are summarised in Table. (3.10). Alike example 1, the run-time improves at the expense of creating more segments. A slight expected improvement in the computed error (SSE_2) is also

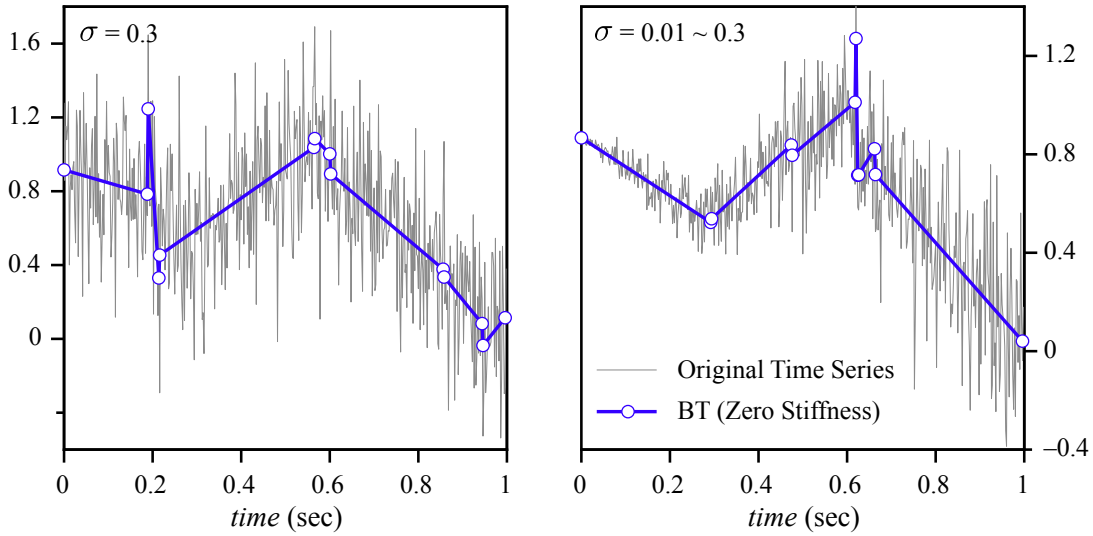

FIGURE 3.17: Synthetic time series with stationary (left) and non-stationary (right) noise and its piece-wise linear approximation using BT algorithm with $\kappa = 0$ - Example 1.

observable as the number of break-points increases.

σ	**NoB**	**Run-time**	**SSE**$_1$	**SSE**$_2$
0.01	14	0.56	4.24E-6	9.26E-5
0.05	9	0.57	1.38E-4	0.0025
0.1	13	0.57	6.45E-4	0.0103
0.2*	7	1.08	0.0019	0.0396
0.01-0.2*	9	1.09	8.30E-4	0.0143

TABLE 3.10: Number of break-points (NoB), run-time (in seconds) and error (SSE_1 and SSE_2 given by Eq. (3.1)) of the BT method with $\kappa = 0$ - Example 2 ((*) denotes outlier detector activation).

The time series of example 2 with additive noise with $\sigma = 0.1$ is shown in Fig. 3.18 along with its piece-wise linear approximation that includes the true break-points.

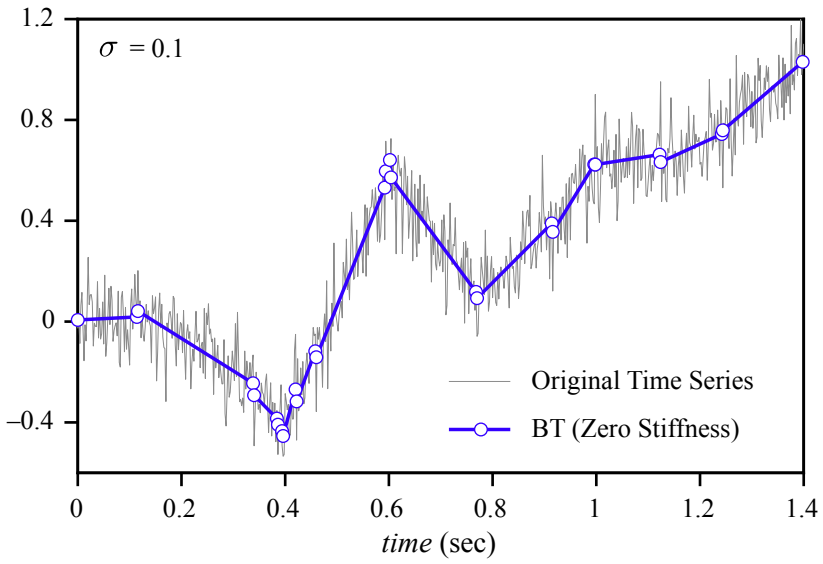

FIGURE 3.18: Synthetic time series with noise standard deviation of $\sigma = 0.1$ and its piece-wise linear approximation using BT algorithm with $\kappa = 0$ - Example 2.

Finally, the results of segmenting the signal introduced in example 3 using "BBQ Tong" with zero stiffness and $N = 80$ are shown in Table. (3.11). A significant improvement in run-time (up to 10 times faster) is observable while the number of break-points is increased up to four times. Again, slight improvement in the computed error (SSE_2) is observed due to signal over fragmentation.

σ	**NoB**	**Run-time**	**SSE$_1$**	**SSE$_2$**
0.01	111	2.53	6.88E-6	9.88E-5
0.05	96	2.34	1.54E-4	0.0024
0.1	94	2.49	6.00E-4	0.0096
0.2	96	2.45	0.0019	0.0388

TABLE 3.11: Number of break-points (NoB), run-time (in seconds) and error (SSE_1 and SSE_2 given by Eq. (3.1)) of the BT method with $\kappa = 0$ - Example 3.

Fig. 3.19 illustrates the linear approximation of the time series introduced in example 3 with white Gaussian noise ($\sigma = 0.05$). Although the approximation is over fragmented compare to the original linear background trend of the signal, the approximation incorporates all the true break-points.

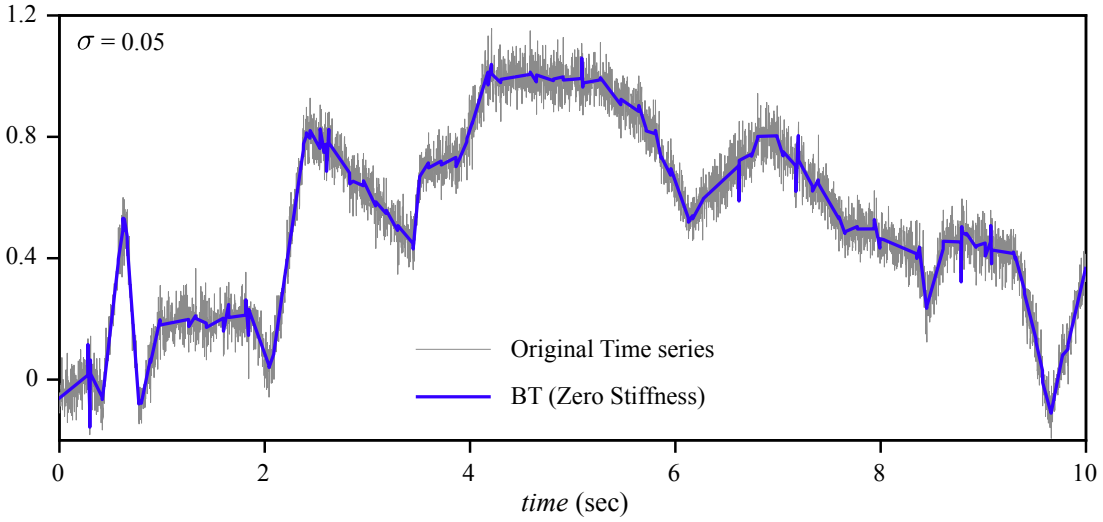

FIGURE 3.19: Synthetic time series with noise standard deviation of $\sigma = 0.05$ and its piece-wise linear approximation using BT algorithm with $\kappa = 0$ - Example 3.

3.5 Segmentation of Field Drilling Data

In this final section, we apply the segmentation method on drilling data recorded both on surface on the rig floor and downhole. In the following we consider three of the main mechanical measurements, namely the hook position, weight-on-bit and torque.

3.5.1 Hook Position

The hook position is the vertical position of the hook hoisting the drill string. It is an essential measure use to assess the borehole depth but also compute the rate of penetration. The rate of penetration is a critical parameter necessary to determine the drilling performance ([96], [40]). A record of the hook position over about five hours of drilling operation is illustrated in Fig. 3.20. The signal is recorded with a scanning period of about seven seconds and includes 2700 data points, covering two connections (addition of a new drill pipe of approximately 27 meters length).

Commonly the rate of penetration is simply estimated by taking the derivative of the hook position yielding an estimate of the rate of penetration that exhibits quite some dispersion, see Fig. 3.21. A piece-wise linear segmentation is in this situation an elegant alternative to estimate an average rate of penetration producing an estimate with less dispersion, see Fig. 3.21.

The ROP estimated from a piece-wise linear approximation of the hook position

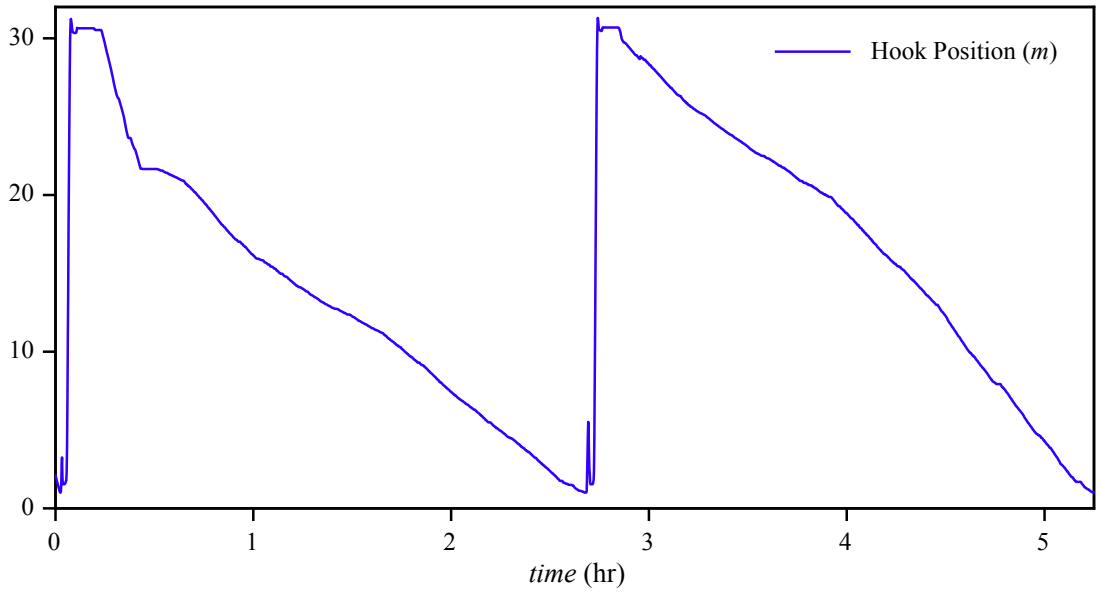

FIGURE 3.20: Hook position measured while five hours of drilling operation.

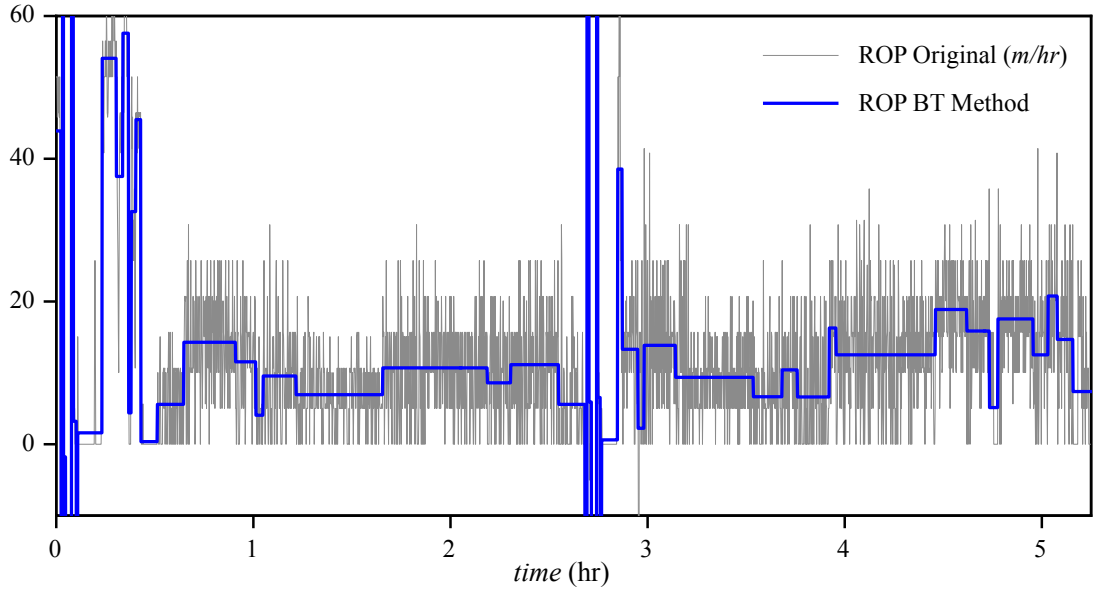

FIGURE 3.21: Original ROP and its approximation using "BBQ Tong" algorithm.

using DP, SW and BT methods is illustrated in Fig. 3.15. As shown in the figure, DP and SW approximation techniques provide disjoint segments which results in jumps in the ROP estimate.

The run-time and error associated with each of the three segmentation techniques i.e. Dynamic Programming (DP), Sliding Window (SW) and BBQ Tong (BT) for segmenting the hook position signal are provided in Table. 3.12. For comparison

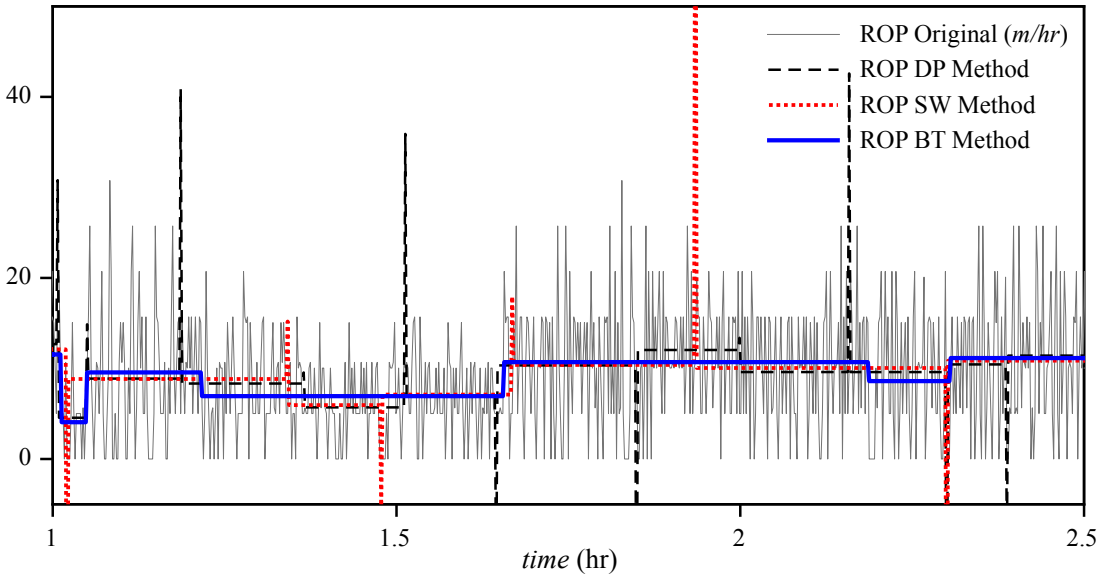

FIGURE 3.22: Original ROP and its approximation using DP, SW and BT algorithms.

purposes, the number of generated segments is taken equal to 80 for the three methods.

Method	**Run-time**	$\mathbf{SSE}_2$
DP	247.42	0.0013
SW	28.03	0.0013
BT	3.65	0.0014

TABLE 3.12: Run-time and error ($\mathbf{SSE}_2$) associated with each segmentation method - Hook Position Example.

As expected, the BT algorithm exhibits a remarkable improvement in terms of the computational effort compare to DP an SW methods while the error ($\mathbf{SSE}_2$) is slightly increased. The time required for the BT method to obtain the same number of break-points with approximately equivalent error is reduced by factor of 67 (8) compare to DP (SW) method.

3.5.2 Weight on Bit (WOB)

A section of 60 seconds of down-hole weight on bit (WOB) recorded by the Isub [31] along with the piece-wise linear approximations using, DP, SW and BT methods is shown in Fig. 3.23. The signal includes 3000 data points with $T = 0.02$, and the "BBQ Tong" with $N = 80$ and $\kappa = 0.008$ is used for segmentation. As shown in the figure, the

measurement carries considerable level of additive noise, and thus, "BBQ tong" with non-zero stiffness is found to be well-suited for the segmentation process.

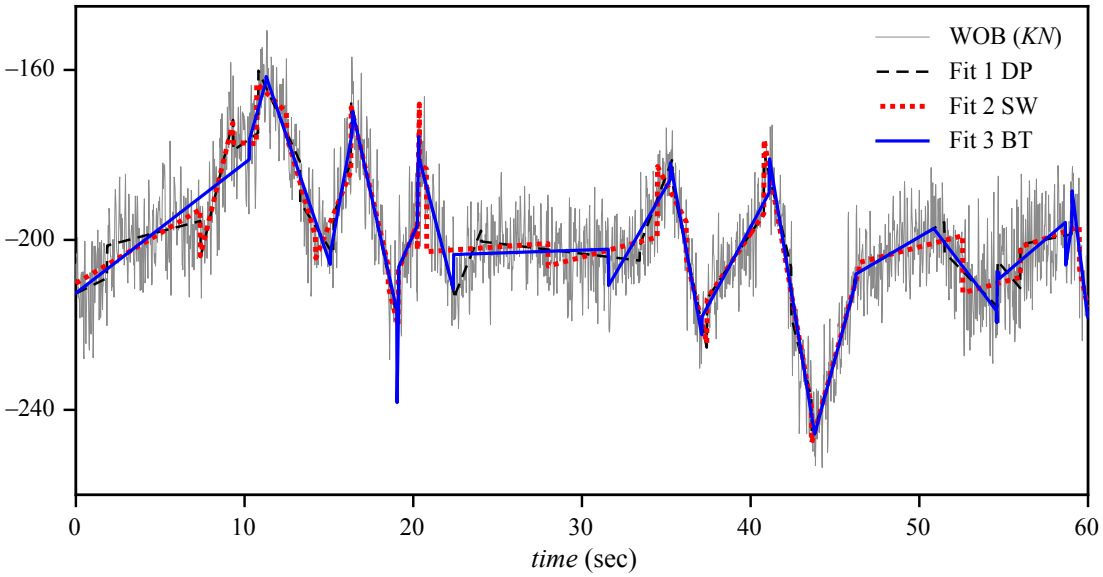

FIGURE 3.23: Weight on Bit (WOB) signal and its piece-wise linear approximations using DP, SW and BT algorithms.

The run-time and error associated with each of the three segmentation techniques for segmenting the WOB signal are provided in Table. 3.13. For comparison purposes, the number of generated segments is assumed to be 22 for the three methods.

Method	**Run-time**	**SSE_2**
DP	215.57	45.955
SW	39.93	50.565
BT	20.15	51.199

TABLE 3.13: Run-time and error associated with each segmentation method.

Similar to the previous example, the BT method still outperforms the other two techniques in terms of the computational time. However, the improvement factor is not as significant as the ROP example, since the stiffness is non-zero and the legs length is almost five times longer.

3.5.3 Torque on Bit (TOB)

A 24 seconds of downhole weight on bit (TOB) recorded by Isub [31] along with its piece-wise linear approximations using, DP, SW and BT methods is well illustrated in Fig. 3.24. The signal includes 1200 data points with $T = 0.02$, and the "BBQ Tong" with $N = 40$ and $\kappa = 0.004$ is used for the segmentation.

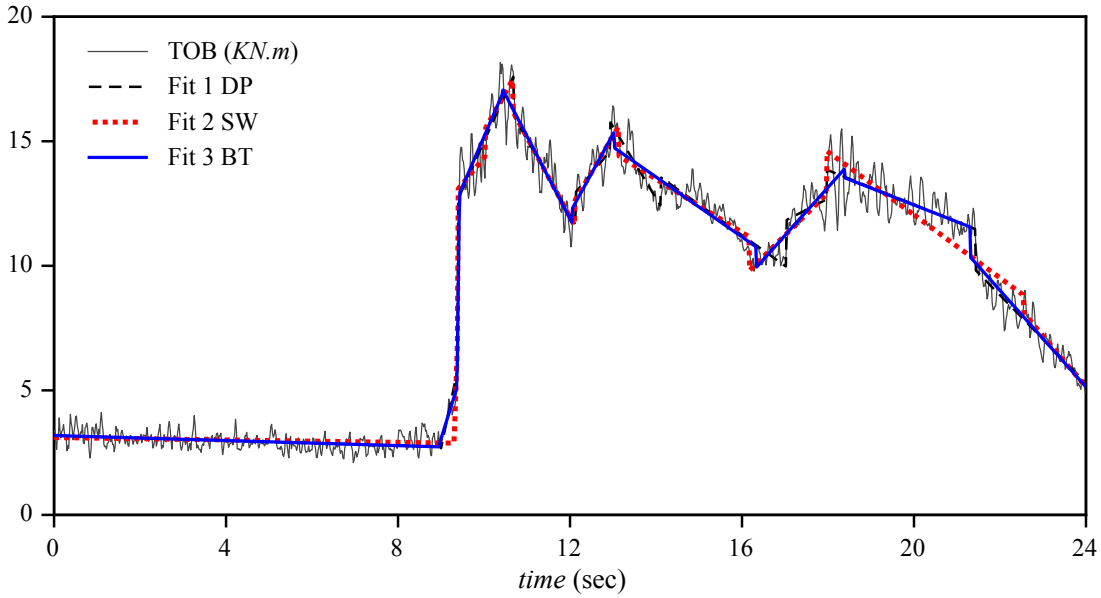

FIGURE 3.24: Torque on Bit (TOB) signal and its piece-wise linear approximations using DP, SW and BT algorithms.

The run-time and error associated with each of the three segmentation techniques for segmenting the TOB signal are provided in Table. 3.14. For comparison purposes, the number of generated segments is assumed to be 9 for the three methods.

Method	**Run-time**	**SSE_2**
DP	21.48	0.2767
SW	8.56	0.3922
BT	6.40	0.3091

TABLE 3.14: Run-time and error associated with each segmentation method.

Second example consists of 60 seconds of TOB measured downhole using instrumented sub. The TOB signal along with its piece-wise linear approximations using, DP, SW and BT methods is well illustrated in Fig. 3.25. The signal includes 3000 data

points with $T = 0.02$, and the "BBQ Tong" with $N = 80$ and $\kappa = 0.004$ is used for the segmentation.

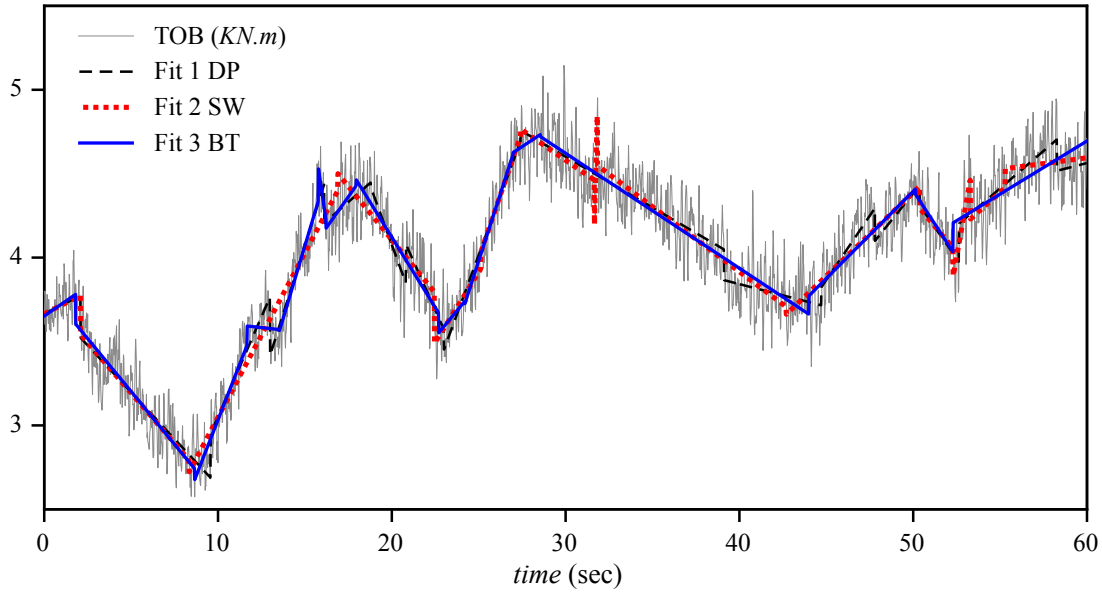

FIGURE 3.25: Torque on Bit (TOB) signal and its piece-wise linear approximations using DP, SW and BT algorithms.

The run-time and error associated with each of the three segmentation techniques for segmenting the TOB signal are provided in Table. 3.15. For comparison purposes, the number of generated segments is assumed to be 14 for the three methods.

Method	**Run-time**	**SSE_2**
DP	217.18	0.0186
SW	37.81	0.0210
BT	27.16	0.0209

TABLE 3.15: Run-time and error associated with each segmentation method.

Tables 3.15 and 3.15, draw similar conclusions in terms of the computational time to what was observed earlier for segmenting hook position and WOB signals.

3.6 Summary

Extensive numerical simulations were carried out in this chapter using synthetic time series corrupted by white Gaussian noise with various noise intensities. The performance

of the "BBQ Tong" method in terms of run-time and error was compared with two proposed linear approximation techniques in the literature: the dynamic programming algorithm introduced by Kehagias et. al. [72] and the span window method developed by Liu et al. [69]. An algorithm using the tool with zero stiffness was developed to manage detrimental outliers.

In addition, similar simulations were carried out on field drilling data, including hook position (surface measurement), weight on bit and torque on bit (downhole measurements) signal.

The "BBQ Tong" segmentation was concluded to outperform the other two methods in terms of the computational effort, and was proven to be very fast for the estimation of the rate of penetration as we could rely on the zero stiffness tool.

Chapter 4

Conclusions

4.1 Main Results

A novel algorithm for piece-wise linear segmentation of time series corrupted with noise dubbed "BBQ Tong" is proposed in this part of the research. The algorithm relies on the geometrical properties of the residual signal and can be implemented in either an iterative or a non-iterative ways. The "BBQ Tong" is a mechanical-mathematical tool aimed at identifying the so called *break-points* where the linear behaviour of the underlying trend of the time series undergoes a change. This was carried out by mapping the break-points in the time series to the *most triangular peaks* in the signal of residuals and capturing them using the "BBQ Tong" algorithm.

As the additive noise plays an important role in the response of the tool, an extensive study was carried out to determine the response of the tool with given specifications (N and κ) to a white Gaussian noise with zero mean and a standard deviation of σ. The probability density function of the hinge angle (tool response) for a given tool specifications and white Gaussian noise statistical properties was derived analytically despite the complexity associated with the derivation involving extreme order statistics and first passage time analysis of the continuous and a discrete stochastic processes. The solution as well as intermediate results (providing valuable insight on the tool behaviour) drove a thorough parametric analysis of the tool response to the noise.

A numerical analysis was then carried out to study the sensitivity of the tool response to the peakiness of the background peaks by considering an academic example with a background signal that consists of a simple isosceles triangle superimposed on

a white Gaussian noise. The simulations together with the noise response provided a guideline to select the appropriate stiffness and legs length for the "BBQ Tong".

A method to deal with detrimental outliers was presented before the numerical experiments were carried out. Three different synthetic piece-wise linear time series corrupted with white Gaussian noise were considered for numerical simulations. In addition to synthetic time series, a few examples including the piece-wise linear segmentation of the downhole drilling data were also provided.

The results were compared with results obtained from two methods proposed in the literature, the dynamic programming algorithm introduced by Kehagias et. al. [72] and also the span window method developed by Liu et al. [69]. The results showed that the "BBQ Tong" method is quite competitive yielding comparable errors and most often shorter computational time. Also the "BBQ Tong" algorithm displayed the ability to handle time series corrupted by non-stationary noise where SW method tends to fail. Also, due to its inherent adaptivity, the tool is found very efficient to detect abrupt (in term of slope) deviations, although short, from a linear trend.

4.2 Limitations and Future Works

Based on the results achieved in this part of the research, the following topics are suggested for future works:

- In this work, the analytical response was limited to the white Gaussian noise. Further study can be performed assuming other types of noise such as coloured noise or heavy tailed noise.
- As the computational efforts increase with the tool length N, improvements should be sought to speed up the algorithm.
- The outlier management although efficient, should be upgraded as to be conducted along with the break-point search.
- There is also some indication that the "BBQ Tong" can be used as a pattern recognition tool to detect and identify the events of similar shapes (triangles) within a given signal.

Appendix A

Kalman filters Model for Estimating the Bit Center Trajectory

A.1 State Space Model

The continuous-time state-space model of a Newtonian system of varying acceleration for motion in axis i can be written as

$$\dot{\mathbf{x}}(t) = A\mathbf{x}(t) + B\mathbf{w}(t) \tag{A.1}$$

$$\mathbf{y}(t) = C\mathbf{x}(t) + \mathbf{v}(t), \tag{A.2}$$

with the state vector $\mathbf{x}(t)$, in axis i defined by

$$\mathbf{x}(t) = \begin{bmatrix} R_i(t) & \dot{R}_i(t) & \ddot{R}_i(t) \end{bmatrix}^T, \tag{A.3}$$

where R_X, $\dot{R}_X$ and $\ddot{R}_X$ are the projection of the position, velocity and acceleration of the bit center on i axis in the fixed frame respectively. The system matrix A, process noise coefficient vector B and output matrix C are defined by

$$A = \begin{bmatrix} 0 & 1 & 0 \\ 0 & 0 & 0 \\ 0 & 0 & 0 \end{bmatrix}, \quad B = \begin{bmatrix} 0 \\ 0 \\ 1 \end{bmatrix}, \quad C = \begin{bmatrix} 0 & 0 & 0 \\ 0 & 0 & 0 \\ 0 & 0 & 1 \end{bmatrix}. \tag{A.4}$$

Note that the first two components of the state vector do not contain any process noise since they are obtained from kinematic of a particle [97]. The process noise $\mathbf{w}(t)$,

and measurement noise $\mathbf{v}(t)$, which is assumed to be modelled by a zero-mean Gaussian white-noise process with known covariance matrix.

$$\mathbf{w}(t) \sim \mathcal{N}(0, \mathbf{Q}_t), \quad \mathbf{v}(t) \sim \mathcal{N}(0, \mathbf{R}_t). \tag{A.5}$$

Discretization of the above continuous model results in

$$\mathbf{x}_k = \mathbf{F}_i \mathbf{x}_{k-1} + \mathbf{G}_i \mathbf{w}_{k-1} \tag{A.6}$$

$$\mathbf{y}_k = \mathbf{H}_i \mathbf{x}_k + \mathbf{v}_k, \tag{A.7}$$

where the state transition matrix is determined by [43]

$$\mathbf{F}_i = e^{A\tau} = \sum_{j=0}^{\infty} \frac{(A\tau)^j}{j!} = \begin{bmatrix} 1 & \tau & \frac{1}{2}\tau^2 \\ 0 & 1 & \tau \\ 0 & 0 & 1 \end{bmatrix}, \tag{A.8}$$

with τ the sampling period of the accelerometer measurement. The matrix $\mathbf{G}_i$ can be determined by [43]

$$\mathbf{G}_i = \mathbf{F}_i \int_0^{\tau} e^{-At} dt\, B = \begin{bmatrix} \frac{1}{6}\tau^3 \\ \frac{1}{2}\tau^2 \\ \tau \end{bmatrix}. \tag{A.9}$$

The covariance of the process noise is given by

$$\mathbf{Q}_i = \int_0^{\tau} e^{At} \mathbf{Q}_t \left(e^{At}\right)^T dt = \sigma_w^2 \begin{bmatrix} \frac{1}{20}\tau^5 & \frac{1}{8}\tau^4 & \frac{1}{6}\tau^3 \\ \frac{1}{8}\tau^4 & \frac{1}{3}\tau^3 & \frac{1}{2}\tau^2 \\ \frac{1}{6}\tau^3 & \frac{1}{2}\tau^2 & \tau \end{bmatrix}, \tag{A.10}$$

where $\mathbf{Q}_t$ is defined by

$$\mathbf{Q}_t = \begin{bmatrix} 0 & 0 & 0 \\ 0 & 0 & 0 \\ 0 & 0 & \sigma_{\mathbf{w}}^2 \end{bmatrix}, \tag{A.11}$$

with $\sigma_{\mathbf{w}}^2$ the variance of $\mathbf{w}(t)$. Finally the measurement sensitivity matrix is

$$\mathbf{H}_i = \begin{bmatrix} 0 & 0 & 1 \end{bmatrix} \tag{A.12}$$

since only the measurement of the planar acceleration in axes i direction in known. The measurement noise covariance matrix is given by

$$\mathbf{R}_i = \sigma_v^2 \tag{A.13}$$

where σ_v^2 is the variance of the acceleration measurement noise.

A.2 Kalman Filter Model

The discrete time state space model can be written as above

$$\mathbf{x}_k = \mathbf{F}\mathbf{x}_{k-1} + \mathbf{G}w_{k-1} \tag{A.14}$$

$$\mathbf{y}_k = \mathbf{H}\mathbf{x}_k + \mathbf{v}_k, \tag{A.15}$$

where the state vector is given by

$$\mathbf{x}_k = \begin{bmatrix} R_{X,k} & \dot{R}_{X,k} & \ddot{R}_{X,k} & R_{Y,k} & \dot{R}_{Y,k} & \ddot{R}_{Y,k} \end{bmatrix}^T, \tag{A.16}$$

and the state transition matrix is

$$\mathbf{F} = \begin{bmatrix} \mathbf{F}_X & \mathbf{0}_3 \\ \mathbf{0}_3 & \mathbf{F}_Y, \end{bmatrix} \tag{A.17}$$

where

$$\mathbf{0}_3 = \begin{bmatrix} 0 & 0 & 0 \\ 0 & 0 & 0 \\ 0 & 0 & 0 \end{bmatrix}. \tag{A.18}$$

The covariance matrix of the process noise is then given by

$$\mathbf{Q} = \begin{bmatrix} \mathbf{Q}_X & \mathbf{0}_3 \\ \mathbf{0}_3 & \mathbf{Q}_Y \end{bmatrix}. \tag{A.19}$$

The measurement vector is

$$\mathbf{y}_k = \begin{bmatrix} \hat{\ddot{R}}_{X,k} \\ \hat{\ddot{R}}_{Y,k} \end{bmatrix}. \tag{A.20}$$

The measurement sensitivity matrix

$$\mathbf{H} = \begin{bmatrix} \mathbf{H}_X & \mathbf{H}_Y \end{bmatrix}. \tag{A.21}$$

The covariance matrix of the measurement noise

$$\mathbf{R} = \begin{bmatrix} \mathbf{R}_X & 0 \\ 0 & \mathbf{R}_Y \end{bmatrix}. \tag{A.22}$$

The complete model of time update equation is

$$\begin{bmatrix} R_{X,k} \\ \dot{R}_{X,k} \\ \ddot{R}_{X,k} \\ R_{Y,k} \\ \dot{R}_{Y,k} \\ \ddot{R}_{Y,k} \end{bmatrix} = \begin{bmatrix} 1 & \tau & \frac{1}{2}\tau^2 & 0 & 0 & 0 \\ 0 & 1 & \tau & 0 & 0 & 0 \\ 0 & 0 & 1 & 0 & 0 & 0 \\ 0 & 0 & 0 & 1 & \tau & \frac{1}{2}\tau^2 \\ 0 & 0 & 0 & 0 & 1 & \tau \\ 0 & 0 & 0 & 0 & 0 & 1 \end{bmatrix} \begin{bmatrix} R_{X,k-1} \\ \dot{R}_{X,k-1} \\ \ddot{R}_{X,k-1} \\ R_{Y,k-1} \\ \dot{R}_{Y,k-1} \\ \ddot{R}_{Y,k-1} \end{bmatrix} + \begin{bmatrix} \frac{1}{6}\tau^3 \\ \frac{1}{2}\tau^2 \\ \tau \\ \frac{1}{6}\tau^3 \\ \frac{1}{2}\tau^2 \\ \tau \end{bmatrix} w_{k-1}, \tag{A.23}$$

and measurement update equation is

$$\begin{bmatrix} \hat{\ddot{R}}_{X,k} \\ \hat{\ddot{R}}_{Y,k} \end{bmatrix} = \begin{bmatrix} 0 & 0 & 1 & 0 & 0 & 0 \\ 0 & 0 & 0 & 0 & 0 & 1 \end{bmatrix} \begin{bmatrix} R_{X,k} \\ \dot{R}_{X,k} \\ \ddot{R}_{X,k} \\ R_{Y,k} \\ \dot{R}_{Y,k} \\ \ddot{R}_{Y,k} \end{bmatrix} \begin{bmatrix} v_{x,k} \\ v_{y,k} \end{bmatrix}, \tag{A.24}$$

where $\hat{\ddot{R}}_{k,X}$ and $\hat{\ddot{R}}_{k,Y}$ are the measured accleration of the bit center in X and Y directions respectively. $v_{k,x}$ and $v_{k,y}$ correspond to the noise correlated to the related measurement channels.

Note that only the measurement of the four centripetal and one tangential accelerometers are available and we need to work out the measurement vector of the Kalman filter out of the accelerometers records with corresponding noise statistics. Accounting for the bias error β_i and the measurement noise υ_i, the output of the i^{th} accelerometer reads

$$\hat{a}_i = \mathbf{n}_i^T(\ddot{\mathbf{R}}_i - \mathbf{a}_g) + \beta_i + \upsilon_i. \tag{A.25}$$

Expanding the above formula for the four centripetal accelerometers result in

$$\hat{a}_1 = \ddot{R}_{1,x} - (\mathbf{a}_g)_x + \beta_1 + \upsilon_1 \tag{A.26}$$

$$\hat{a}_2 = \ddot{R}_{2,y} - (\mathbf{a}_g)_y + \beta_2 + \upsilon_2 \tag{A.27}$$

$$\hat{a}_3 = -\ddot{R}_{3,x} + (\mathbf{a}_g)_x + \beta_3 + \upsilon_3 \tag{A.28}$$

$$\hat{a}_4 = -\ddot{R}_{4,y} + (\mathbf{a}_g)_y + \beta_4 + \upsilon_4, \tag{A.29}$$

where $\ddot{R}_{1,x}$ and $\ddot{R}_{3,x}$ are the acceleration of sensors 1 and 3 along x axis and $\ddot{R}_{2,y}$ and $\ddot{R}_{4,y}$ are the acceleration of sensors 2 and 4 along y axis respectively. It is assumed that sensors have no alignment error. As it was determined before, the acceleration of the bit center in x and y direction is determined by

$$\ddot{R}_x = \frac{1}{2}\left(\ddot{R}_{1,x} + \ddot{R}_{3,x}\right) \tag{A.30}$$

$$\ddot{R}_y = \frac{1}{2}\left(\ddot{R}_{2,y} + \ddot{R}_{4,y}\right). \tag{A.31}$$

Substituting Eqs. (A.26) and (A.28) in Eq. (A.30) and also Eqs. (A.27) and (A.29)

in Eq. (A.31) results in

$$\ddot{R}_x = \frac{1}{2}\left(\hat{a}_1 - \hat{a}_3\right) + (\mathbf{a}_g)_x - \frac{1}{2}\left[(\beta_1 - \beta_3) + (\upsilon_1 - \upsilon_3)\right] \tag{A.32}$$

$$\ddot{R}_y = \frac{1}{2}\left(\hat{a}_2 - \hat{a}_4\right) + (\mathbf{a}_g)_y - \frac{1}{2}\left[(\beta_2 - \beta_4) + (\upsilon_2 - \upsilon_4)\right]. \tag{A.33}$$

It can be inferred from Eqs. (A.32) and (A.33) that in order to use the accelerometers measurement, we need to know the values of bias for each sensor and also the part of the gravity which contributes in each sensor output. Also, $\mathbf{a}_g$ components in x and y directions are a function of the rotation and vary with time i.e.

$$(\mathbf{a}_g)_x = g\sin\gamma\cos\phi \tag{A.34}$$

$$(\mathbf{a}_g)_y = g\sin\gamma\sin\phi. \tag{A.35}$$

Therefore, in order to obtain $(\mathbf{a}_g)_x$ and $(\mathbf{a}_g)_y$, we not only need to know the borehole inclination, but also the orientation of each sensor with respect to $\mathbf{a}_g$. So, the information recorded at connections will be of no use.

Finally we need to apply a transformation to go from rotating frame xy to the fixed from XY as

$$\begin{bmatrix} \hat{\ddot{R}}_X \\ \hat{\ddot{R}}_Y \end{bmatrix} = \begin{bmatrix} \cos\theta & -\sin\theta \\ \sin\theta & \cos\theta \end{bmatrix} \begin{bmatrix} \hat{\ddot{R}}_x \\ \hat{\ddot{R}}_y \end{bmatrix}. \tag{A.36}$$

The final measurement update equation considering all the parameters is

$$\begin{bmatrix} \frac{1}{2}\left(\hat{a}_{1,k} - \hat{a}_{3,k}\right) \\ \frac{1}{2}\left(\hat{a}_{2,k} - \hat{a}_{4,k}\right) \end{bmatrix} = \begin{bmatrix} 0 & 0 & \cos\theta & 0 & 0 & \sin\theta \\ 0 & 0 & -\sin\theta & 0 & 0 & \cos\theta \end{bmatrix} \begin{bmatrix} R_{X,k} \\ \dot{R}_{X,k} \\ \ddot{R}_{X,k} \\ R_{Y,k} \\ \dot{R}_{Y,k} \\ \ddot{R}_{Y,k} \end{bmatrix} - \begin{bmatrix} (\mathbf{a}_g)_{x,k} \\ (\mathbf{a}_g)_{y,k} \end{bmatrix} + \begin{bmatrix} \beta_x \\ \beta_y \end{bmatrix} + \begin{bmatrix} v_{x,k} \\ v_{y,k} \end{bmatrix}. \tag{A.37}$$

It is assumed that the bias between two connection is constant and is updated at each connection

$$\beta_x = \frac{1}{2}\left(\beta_1 - \beta_3\right), \qquad \beta_y = \frac{1}{2}\left(\beta_2 - \beta_4\right). \tag{A.38}$$

Appendix B

Response of the "BBQ Tong" with Zero Stiffness to Correlated Gaussian Noise

The appendix deals with the determination of the analytic response of the "BBQ Tong" to a correlated Gaussian noise. Let $\mathbf{Y} = (Y_1, \ldots, Y_k)$ be a discrete-time correlated Gaussian noise uniformly spaced with zero mean and correlation matrix R. That is,

$$\mathbf{Y} \sim \mathcal{N}(0, R), \tag{B.1}$$

where the correlation matrix of the random vector Y with length k is defined as

$$R = \begin{bmatrix} 1 & \cdots & \rho_{1,k} \\ & \ddots \quad \rho_{p,q} & \\ \vdots & 1 & \vdots \\ & \ddots & \\ \rho_{k,1} & \cdots & 1 \end{bmatrix}_{k \times k}, \tag{B.2}$$

where $\rho_{p,q}$ corresponds to the correlation between the p^{th} and q^{th} components of the vector $\mathbf{Y}$ i.e. Y_p and Y_q, and is defined by

$$\rho_{p,q} = \frac{\mathrm{Cov}(Y_p, Y_q)}{\sqrt{\mathrm{Cov}(Y_p, Y_p)\,\mathrm{Cov}(Y_q, Y_q)}}, \tag{B.3}$$

where Cov in Eq.(B.3) stands for the covariance function. It can be inferred from this equation that the correlation matrix, R is symmetric. In the case of white Gaussian noise, all the non-diagonal arrays of the correlation matrix R are zero.

The probability density function of $\mathbf{Y}$ related to the joint probability distribution function of Y_1 to Y_k is [90]

$$f_{\mathbf{Y}}(\mathbf{y}) = \frac{1}{(2\pi)^{\frac{k}{2}}\,|R|^{\frac{k}{2}}} \exp\left(-\frac{1}{2}\mathbf{y}^{'} R^{-1}\mathbf{y}\right). \tag{B.4}$$

where $|R|$ is the determinant of the correlation matrix.

Similar to the procedure performed in sec. 2.4.1.1, to obtain the probability density function of Θ, the joint probability distribution function of the hinge left and right angles given y is required. The cumulative distribution function of Θ_L and Θ_R given y is defined as

$$F_{\Theta_L\Theta_R|y}(\theta_L, \theta_R) = \Pr\left(\Theta_L|y \le \theta_L,\, \Theta_R|y \le \theta_R\right), \tag{B.5}$$

where the left and right angles conditioned on y are obtained using

$$\Theta_L|y = \max\left(\Theta_i^L|y\right), \quad \Theta_R|y = \max\left(\Theta_j^R|y\right) \qquad \text{for all} \quad 1 \le i, j \le N. \tag{B.6}$$

Substituting Eq. (B.6) in Eq. (B.5) provides

$$F_{\Theta_L\Theta_R|y}(\theta_L, \theta_R) = \Pr\left(\left\{\Theta_1^L, \ldots, \Theta_N^L|y\right\} \le \theta_L,\, \left\{\Theta_1^R, \ldots, \Theta_N^R|y\right\} \le \theta_R\right). \tag{B.7}$$

A random vector $\mathbf{U}$ is defined as a set of all possible hinge left and right angles (Θ_i^L and Θ_j^R for all $1 \le i, j \le N$). Thus

$$\mathbf{U} = \left(\Theta_1^L, \ldots, \Theta_N^L, \Theta_1^R, \ldots, \Theta_N^R\right)_{1\times 2N}. \tag{B.8}$$

The joint probability distribution function of Θ_L and Θ_R given y can be written using vector $\mathbf{U}$ as follows

$$F_{\Theta_L\Theta_R|y}(\theta_L, \theta_R) = \underbrace{\int_{-\infty}^{\theta_L} \cdots \int_{-\infty}^{\theta_L}}_{N\,\text{times}} \underbrace{\int_{-\infty}^{\theta_R} \cdots \int_{-\infty}^{\theta_R}}_{N\,\text{times}} f_{\mathbf{U}|y}(\mathbf{u})\, d\mathbf{u}, \tag{B.9}$$

where

$$d\mathbf{u} = \prod_{i=1}^{N} d\theta_i^L . \prod_{j=1}^{N} d\theta_j^R. \tag{B.10}$$

To determine the probability density function of $\mathbf{U}$, functions g_i and h_i are defined using Eq. (2.16) as follows

$$\Theta_i^L = \frac{\pi}{2} - \arctan\left(\frac{Y - Y_i^L}{i\,T}\right) = g_i\left(Y_i^L\right), \qquad 1 \le i \le N \tag{B.11}$$

$$\Theta_j^R = \frac{\pi}{2} - \arctan\left(\frac{Y - Y_j^R}{j\,T}\right) = h_j\left(Y_j^R\right), \qquad 1 \le j \le N. \tag{B.12}$$

A random vector $\mathbf{V}$ is introduced as the set of correlated random variables of $\mathbf{Y}$ covered by the left and right legs of the "BBQ Tong". Thus

$$\mathbf{V} = \left(Y_1^L, \ldots, Y_N^L, Y_1^R, \ldots, Y_N^R\right)_{1\times 2N}. \tag{B.13}$$

To determine the probability density function of $\mathbf{U}$ for given value of y for a specific set of $\theta_1^L, \ldots, \theta_N^L, \theta_1^R, \ldots, \theta_N^R$, we need to first solve the system of equations given by

$$\theta_i^L = g_i\left(\mathbf{V}\right), \quad \theta_j^R = h_j\left(\mathbf{V}\right) \qquad 1 \le i, j \le N. \tag{B.14}$$

The above system of equations has a single solution, therefore, the probability density function of $\mathbf{U}$ is obtained using the transformation between $\mathbf{U}$ and $\mathbf{V}$ given by Eqs. (B.11) and (B.12) [90]. Hence

$$f_{\mathbf{U}|y}(\mathbf{u}) = \frac{f_{\mathbf{V}|y}(\mathbf{v})}{|J(\mathbf{v})|}, \tag{B.15}$$

where

$$J\left(\mathbf{v}\right) = \begin{bmatrix} \frac{\partial g_1}{\partial y_1^L} & \cdots & \frac{\partial g_1}{\partial y_N^L} & \frac{\partial g_1}{\partial y_1^R} & \cdots & \frac{\partial g_1}{\partial y_N^R} \\ \vdots & \ddots & \vdots & \vdots & \ddots & \vdots \\ \frac{\partial g_N}{\partial y_1^L} & \cdots & \frac{\partial g_N}{\partial y_N^L} & \frac{\partial g_N}{\partial y_1^R} & \cdots & \frac{\partial g_N}{\partial y_N^R} \\ & & & & & \\ \frac{\partial h_1}{\partial y_1^L} & \cdots & \frac{\partial h_1}{\partial y_N^L} & \frac{\partial h_1}{\partial y_1^R} & \cdots & \frac{\partial h_1}{\partial y_N^R} \\ \vdots & \ddots & \vdots & \vdots & \ddots & \vdots \\ \frac{\partial h_N}{\partial y_1^L} & \cdots & \frac{\partial h_N}{\partial y_N^L} & \frac{\partial h_N}{\partial y_1^R} & \cdots & \frac{\partial h_N}{\partial y_N^R} \end{bmatrix} \tag{B.16}$$

is the Jacobian matrix of the transformation. Since $\mathbf{V}$ is a set of correlated random variables followed by Gaussian distribution and known correlation matrix, its density function can be expressed by

$$f_{\mathbf{V}|y}(\mathbf{v}) = \frac{1}{(2\pi)^N \left|\mathbf{\Sigma}\right|^N} \exp\left[-\frac{1}{2}\mathbf{v}'\mathbf{\Sigma}^{-1}\mathbf{v}\right], \tag{B.17}$$

where Σ is the correlation matrix and $|\Sigma|$ indicates its determinant. Since each θ_i^L and θ_j^R are just a function of the corresponding y_i^L and y_j^R respectively (see Eqs. (B.11) and (B.12)), then

$$\frac{\partial \theta_i^L}{\partial y_p^L} = \frac{\partial \theta_i^L}{\partial y_q^R} = 0 \qquad \text{for} \quad i \ne p, q \tag{B.18}$$

$$\frac{\partial \theta_j^R}{\partial y_q^R} = \frac{\partial \theta_j^R}{\partial y_p^R} = 0 \qquad \text{for} \quad j \ne p, q. \tag{B.19}$$

Substituting Eqs. (B.18) and (B.19) in the Jacobian matrix (Eq. (B.16)) results in a diagonal matrix where its determinant is given by

$$|J(\mathbf{v})| = \begin{vmatrix} \frac{\partial g_1}{\partial y_{1L}} & & & & 0 & 0 \\ & \ddots & & & & 0 \\ & & \frac{\partial g_N}{\partial y_{NL}} & & & \\ & & & \frac{\partial h_1}{\partial y_{1R}} & & \\ 0 & & & & \ddots & \\ 0 & 0 & & & & \frac{\partial h_N}{\partial y_{NR}} \end{vmatrix} = \prod_{i=1}^{N} \frac{\partial g_i}{\partial y_i^L} . \prod_{j=1}^{N} \frac{\partial h_j}{\partial y_j^R}. \tag{B.20}$$

The partial derivatives of the functions g_i and h_j with respect to the random vector $\mathbf{v}$ for the Jacobian matrix can be obtained using Eqs. (B.11) and (B.12). Hence

$$\frac{\partial \theta_i^L}{\partial y_i^L} = \frac{1}{i\,T\left[1+\tan^2\left(\frac{\pi}{2}-\theta_i^L\right)\right]}, \qquad \frac{\partial \theta_j^R}{\partial y_j^R} = \frac{1}{j\,T\left[1+\tan^2\left(\frac{\pi}{2}-\theta_j^R\right)\right]}. \tag{B.21}$$

Substituting Eq. (B.21) in Eq. (B.20) provides the determinant of the Jacobian matrix as

$$J(\mathbf{v}) = \prod_{i=1}^{N}\left[\frac{1}{i\,T\left[1+\tan^2\left(\frac{\pi}{2}-\theta_i^L\right)\right]}\right] . \prod_{j=1}^{N}\left[\frac{1}{j\,T\left[1+\tan^2\left(\frac{\pi}{2}-\theta_j^R\right)\right]}\right]. \tag{B.22}$$

The joint probability distribution function of Θ_L and Θ_R conditioned on y is determined by

$$f_{\Theta_L\Theta_R|y}(\theta_L,\theta_R) = \frac{\partial^2}{\partial\theta_L\,\partial\theta_R} F_{\Theta_L\Theta_R|y}(\theta_L,\theta_R)\,. \tag{B.23}$$

The unconditional joint probability distribution function of Θ_L and Θ_R is obtained using the Bayesian rule as

$$f_{\Theta_L\Theta_R}(\theta_L,\theta_R) \;=\; \int_{-\infty}^{+\infty} f_Y(y)\,.f_{\Theta_L\Theta_R|y}(\theta_L,\theta_R)\;dy. \tag{B.24}$$

Recalling Eq. (2.10), the hinge angle ,Θ, can be thought as a function of two dependant random variables, Θ_L and Θ_R. Knowing the joint information of the hinge left and right angles, the probability density function of Θ is determined by

$$f_\Theta(\theta) = \int_{-\infty}^{+\infty} f_{\Theta_L\Theta_R}(\theta_L,\theta-\theta_L)\;d\theta_L. \tag{B.25}$$

In practice, it is very difficult to implement Eq. (B.25) numerically. Galambos [98] provides recommendation on how to compute the asymptotic behaviour of extreme order statistics considering the correlation.

Appendix C

Joint Probability Distribution of X_1 and X_2

As it was well illustrated in Fig. 2.7, it is assumed that the hinge located at a distance δ from the signal and the left leg touches the residual signal at the i^{th} point on the left side of the hinge where i is the index of any arbitrary point on the signal covered by the left leg ($1 \leq i \leq N$). Note that i is an integer counted from the hinge towards the tip of the "BBQ Tong" left leg. The value of the residual signal at contact is Y_i, while the signal value at the hinge location is Y and the hinge height is denoted by Y_h ($y_h = y + \delta$).

The hinge left angle Θ_i (the subscript L is kept for the solution) is then related to the residual signal as follows

$$\tan\left(\frac{\pi}{2} - \Theta_i\right) = \frac{Y + \delta - Y_i}{i\,T}, \qquad 1 \leq i \leq N. \tag{C.1}$$

Alike sec. 2.4.1.1, Eq. (C.1) allows us to express Θ_i as a function of Y_i explicitly. Thus, for given values of δ and y, the probability density function of Θ_i can be written as [90]

$$f_{\Theta_i|y,\delta}\left(\theta_i\right) = f_{Y_i|y,\delta}\left(g^{-1}(\theta_i)\right)\,\left|-\left(i\,T\right)\left[1 + \tan^2\left(\frac{\pi}{2} - \theta_i\right)\right]\right|, \tag{C.2}$$

where

$$f_{Y_i|y,\delta}\left(g^{-1}(\theta_i)\right) = \frac{1}{\sqrt{2\pi\sigma^2}}\,\exp\left[-\frac{1}{2\sigma^2}\left[y + \delta - \left(i\,T\right)\tan\left(\frac{\pi}{2} - \theta_i\right)\right]^2\right]. \tag{C.3}$$

The corresponding cumulative distribution function (cdf) of Θ_i for given values of

y and δ is then determined by

$$F_{\Theta_i|y,\delta}\left(\theta_i\right) = \int_{-\infty}^{\theta_i} f_{\Theta_i|y,\delta}\left(\theta_i\right)\, d\theta_i. \tag{C.4}$$

The random variable L is introduced as the index of the left leg contact point after enforcing the non penetration condition. As L can only take integer values, for given values of δ and y, its probability mass function can be written as

$$f_{\mathtt{L}|y,\delta}(\ell) = \Pr(\mathtt{L} = \ell | Y = y, \Delta = \delta). \tag{C.5}$$

In fact, $f_{\mathtt{L}|y,\delta}(\ell)$ indicates the probability of θ_L being larger than all other angles created by connecting the hinge to the crest of the points on the signal covered by the left leg for a given y and δ. Thus, it can also be expressed by

$$f_{\mathtt{L}|y,\delta}(\ell) = \Pr(\Theta_1 \leq \theta_\ell, \Theta_2 \leq \theta_\ell, \ldots, \Theta_N \leq \theta_\ell | Y = y, \Delta = \delta). \tag{C.6}$$

The value of $f_{\mathtt{L}|y,\delta}(i)$ given by Eq. (C.6) can be computed using the joint probability distribution function of all possible left angles i.e. Θ_1, ..., Θ_N for given values of y and δ. Thus

$$f_{\mathtt{L}|y,\delta}(\ell) = \underbrace{\int_{-\infty}^{+\infty} \int_{-\infty}^{\theta_\ell} \cdots \int_{-\infty}^{\theta_\ell}}_{N\,\text{times}} f_{(\Theta_1,\ldots,\Theta_N)|y,\delta}(\theta_1, \ldots, \theta_N)\, \mathrm{d}\theta_1 \ \ldots\ \mathrm{d}\theta_N. \tag{C.7}$$

As for given values of δ and y, Θ_1, Θ_2, ... , Θ_N are independent and non identically distributed random variables, their joint probability distribution function can be expressed as the product of their individual probability density functions. Hence

$$f_{\mathtt{L}|y,\delta}(\ell) = \int_{-\infty}^{+\infty} \left\{ \left[\underbrace{\left(\int_{-\infty}^{\theta_\ell} f_{\Theta_1|y,\delta}\left(\theta_1\right) \mathrm{d}\theta_1 \right) \ldots \left(\int_{-\infty}^{\theta_\ell} f_{\Theta_N|y,\delta}\left(\theta_N\right) \mathrm{d}\theta_N \right)}_{(N-1)\,\text{integrals}} \right] f_{\Theta_\ell|y,\delta}\left(\theta_\ell\right) \right\} \mathrm{d}\theta_\ell. \tag{C.8}$$

Eventually, simplifying Eq. (C.8) provides

$$f_{\mathtt{L}|y,\delta}(\ell) = \int_{-\infty}^{+\infty} \left[\prod_{i=1}^{N} F_{\Theta_i|y,\delta}\left(\theta_\ell\right) \left[\frac{f_{\Theta_\ell|y,\delta}\left(\theta_\ell\right)}{F_{\Theta_\ell|y,\delta}\left(\theta_\ell\right)} \right] \right] \mathrm{d}\theta_\ell. \tag{C.9}$$

The analytical and numerical representation of the probability mass function of L for $\delta = 0$, $y = 0$, $N = 10$ and $\sigma = 1$ is illustrated in Fig. (C.1).

The same procedure has been followed to calculate the probability mass function of the random variable R (not to be mistaken with R, the horizontal leg length of the

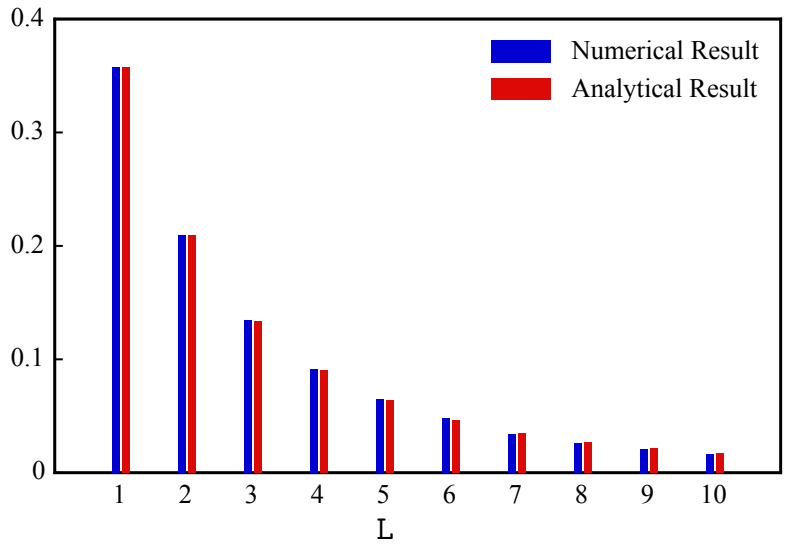

FIGURE C.1: Numerical and analytical representation of $f_{\mathtt{L}|y,\delta}(\ell)$ for $\delta = 0$, $y = 0$, $N = 10$ and $\sigma = 1$.

"BBQ Tong"), the index of the right leg contact point after applying non penetration condition

$$f_{\mathtt{R}|y,\delta}(r) = \int_{-\infty}^{+\infty} \left[\prod_{j=1}^{N} F_{\Theta_j|y,\delta}\left(\theta_r\right) \left[\frac{f_{\Theta_r|y,\delta}\left(\theta_r\right)}{F_{\Theta_r|y,\delta}\left(\theta_r\right)} \right] \right] \mathrm{d}\theta_r. \tag{C.10}$$

The joint probability distribution function of L and R for given values of δ and y can be written as

$$f_{\mathtt{LR}|y,\delta}(\ell, r) = \Pr(\mathtt{L} = \ell, \mathtt{R} = r | Y = y, \Delta = \delta). \tag{C.11}$$

As it was discussed earlier in sec. 2.4.1.1, for given values of δ and y, the hinge left and right angles i.e. Θ_L and Θ_R are independent. Thus, under the same condition, their associated contact point indexes, L and R, are independent as well. This means that their joint probability distribution function can be expressed as the product of their individual probability mass functions as follows

$$f_{\mathtt{LR}|y,\delta}(\ell, r) = f_{\mathtt{L}|y,\delta}(\ell) \,.\, f_{\mathtt{R}|y,\delta}(r). \tag{C.12}$$

The analytical and numerical representation of the joint probability distribution function of RVs L and R for $\delta = -1$, $y = 1$, $N = 10$ and $\sigma = 1$ is well illustrated in Fig. (C.2) using 3D bar plots.

The joint probability distribution function of L and R helps to find the probability mass function of X_2 ("opening moment") for given values of δ and y. Hence

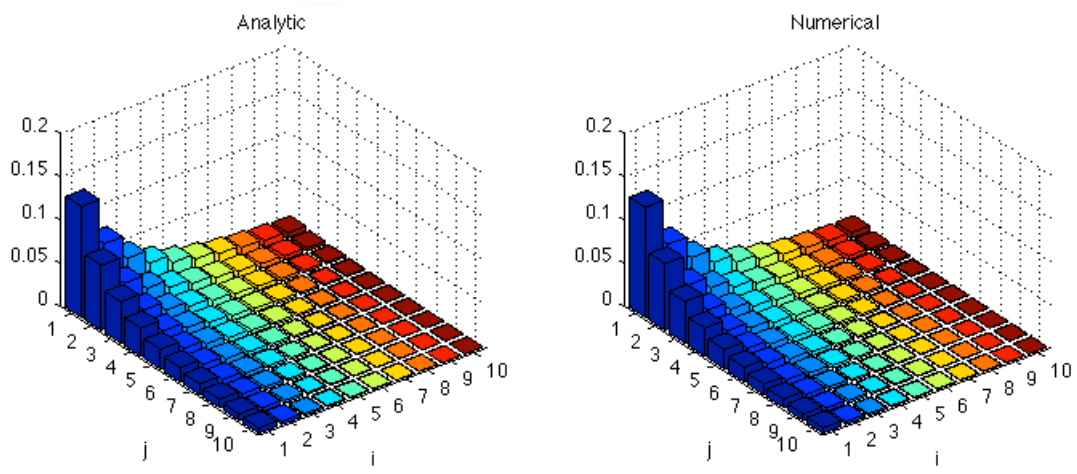

FIGURE C.2: Numerical and analytical representation of $f_{\mathrm{LR}|y,\delta}(\ell, r)$ for $\delta = -1$, $y = 1$, $N = 10$ and $\sigma = 1$.

$$f_{X_2|y,\delta}(x_2) = \Pr\left(X_2 = \frac{\ell\, r}{\ell + r}|y, \delta\right). \tag{C.13}$$

Fig. (C.3) depicts the analytical and numerical representation of the probability mass function of X_2, for given values of $y = 2$,$\delta = 1$, $N = 10$ and $\sigma = 1$. As shown in the figure, X_2 is a discrete random variable.

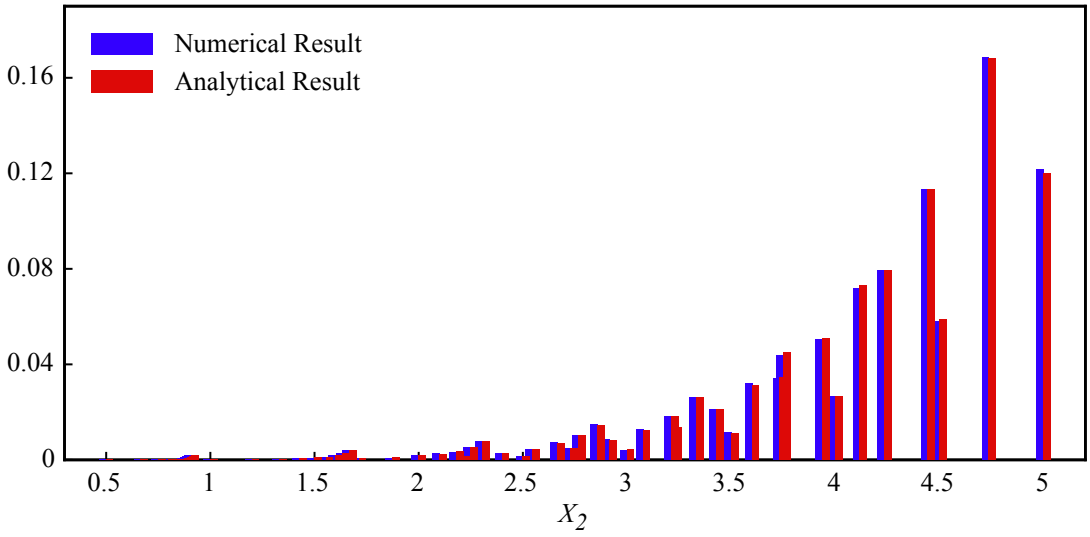

FIGURE C.3: Numerical and analytical representation of $f_{X_2|y,\delta}(x_2)$ for $\delta = 1$, $y = 2$, $N = 10$ and $\sigma = 1$.

Next, we will determine the probability density function of the hinge left angle, Θ_L, for given values of ℓ, y and δ. The function $f_{\Theta_L|\ell,y,\delta}(\theta_L)$ is in fact the probability density

function of the left angles whose contact point index is ℓ. To be able to calculate this pdf, we should first determine the joint probability distribution of Θ_L and $\mathtt{L}$ for given values of y and δ. This is given by

$$f_{\Theta_L\,\mathtt{L}|y,\delta}(\theta_L,\ell)=\Pr\left(\theta_L\leq\Theta_L\leq\theta_L+d\theta_L\,\&\,\mathtt{L}=\ell|Y=y,\Delta=\delta\right). \tag{C.14}$$

Similar to Eq. (C.6), Eq. (C.14) can also be written as

$$f_{\Theta_L\,\mathtt{L}|y,\delta}(\theta_L,\ell)=\Pr\left(\theta_L\leq\Theta_L\leq\theta_L+d\theta_L\,\&\,\Theta_1\leq\theta_\ell,\Theta_2\leq\theta_\ell,\ldots,\Theta_N\leq\theta_\ell|y,\delta\right). \tag{C.15}$$

Eq. (C.15) can be expressed as the integral of the joint probability distribution function of Θ_1, Θ_2, ... , Θ_N over the appropriate domain as follows

$$f_{\Theta_L\,\mathtt{L}|y,\delta}(\theta_L,\ell)=\frac{1}{d\theta_L}\underbrace{\int_{\theta_L}^{\theta_L+d\theta_L}\int_{-\infty}^{\theta_\ell}\cdots\int_{-\infty}^{\theta_\ell}}_{N\,\text{times}}f_{(\Theta_1,\ldots,\Theta_N)|y,\delta}(\theta_1,\ldots,\theta_N)\,\mathrm{d}\theta_1\,\ldots\,\mathrm{d}\theta_N. \tag{C.16}$$

Note that Θ_1, Θ_2, ... , Θ_N are independent and non-identically distributed random variables whose probability density function can be obtained using Eq. (C.2). Therefore, as it mentioned earlier, their joint probability distribution function can be expressed as the product of their individual probability density functions. Hence

$$f_{\Theta_L\,\mathtt{L}|y,\delta}(\theta_L,\ell)=\frac{1}{d\theta_L}\int_{\theta_L}^{\theta_L+d\theta_L}\left\{\Phi(\theta_\ell)\,f_{\Theta_\ell|y,\delta}\left(\theta_\ell\right)\right\}\mathrm{d}\theta_\ell, \tag{C.17}$$

where $\Phi(\theta_\ell)$ is defined by

$$\Phi(\theta_\ell)=\left[\underbrace{\left(\int_{-\infty}^{\theta_\ell}f_{\Theta_1|y,\delta}\left(\theta_1\right)\mathrm{d}\theta_1\right)\ldots\left(\int_{-\infty}^{\theta_\ell}f_{\Theta_N|y,\delta}\left(\theta_N\right)\mathrm{d}\theta_N\right)}_{(N-1)\,\text{integrals}}\right]. \tag{C.18}$$

Simplifying Eq. (C.17) provides

$$f_{\Theta_L\,\mathtt{L}|y,\delta}(\theta_L,\ell)=\frac{1}{d\theta_L}\int_{\theta_L}^{\theta_L+d\theta_L}\left[\prod_{i=1}^{N}F_{\Theta_i|y,\delta}\left(\theta_\ell\right)\left[\frac{f_{\Theta_\ell|y,\delta}\left(\theta_\ell\right)}{F_{\Theta_\ell|y,\delta}\left(\theta_\ell\right)}\right]\right]\mathrm{d}\theta_i. \tag{C.19}$$

Finally, the joint probability distribution function of Θ_L and $\mathtt{L}$ for given values of y and δ can be obtained by

$$f_{\Theta_L\,\mathtt{L}|y,\delta}(\theta_L,\ell)=\prod_{i=1}^{N}F_{\Theta_i|y,\delta}\left(\theta_\ell\right)\left[\frac{f_{\Theta_\ell|y,\delta}\left(\theta_\ell\right)}{F_{\Theta_\ell|y,\delta}\left(\theta_\ell\right)}\right]. \tag{C.20}$$

Note that the sum of $f_{\Theta_L \mathtt{L}|y,\delta}(\theta_L, \ell)$ over all possible values of ℓ should result in Eq. (2.22). In other words

$$f_{\Theta_L|y,\delta}(\theta_L) = \sum_{\ell=1}^{N} f_{\Theta_L \mathtt{L}|y,\delta}(\theta_L, \ell). \tag{C.21}$$

The same procedure is applied to determine the joint probability distribution function of Θ_R and $\mathtt{R}$ for given values of y and δ. Therefore

$$f_{\Theta_R \mathtt{R}|y,\delta}(\theta_R, r) = \prod_{j=1}^{N} F_{\Theta_j|y,\delta}(\theta_r) \left[\frac{f_{\Theta_r|y,\delta}(\theta_r)}{F_{\Theta_r|y,\delta}(\theta_r)} \right]. \tag{C.22}$$

Eventually, the Bayesian rule is used to calculate the probability density function of Θ_L for given values of ℓ, y and δ as follows

$$f_{\Theta_L|\ell,y,\delta}(\theta_L) = \frac{f_{\Theta_L \mathtt{L}|y,\delta}(\theta_L, \ell)}{f_{\mathtt{L}|y,\delta}(\ell)}. \tag{C.23}$$

Fig. (C.4) shows the analytical and numerical representation of the probability density function of Θ_L for given values of $\ell = 8$, $y = 3$, $\delta = 1$, $N = 10$ and $\sigma = 1$.

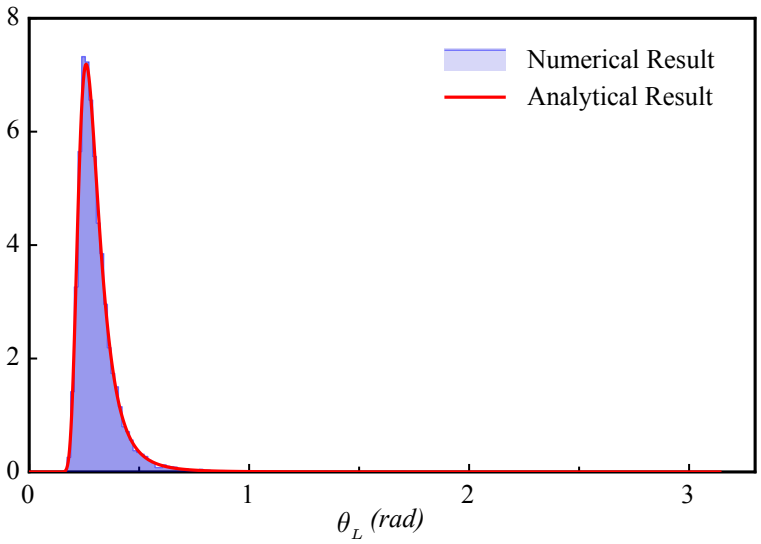

FIGURE C.4: Numerical and analytical representation of $f_{\Theta_L|\ell,y,\delta}(\theta_L)$ for $\ell = 8$, $y = 3$, $\delta = 1$, $N = 10$ and $\sigma = 1$.

The probability density function of Θ_R for given values of r, y and δ can be computed in the same fashion by

$$f_{\Theta_R|r,y,\delta}(\theta_R) = \frac{f_{\Theta_R \mathtt{R}|y,\delta}(\theta_R, r)}{f_{\mathtt{R}|y,\delta}(r)}. \tag{C.24}$$

Fig. (C.5) shows the analytical and numerical representation of the probability density function of Θ_R for given values of $r = 1$, $y = -1$, $\delta = 1.5$, $N = 10$ and $\sigma = 1$.

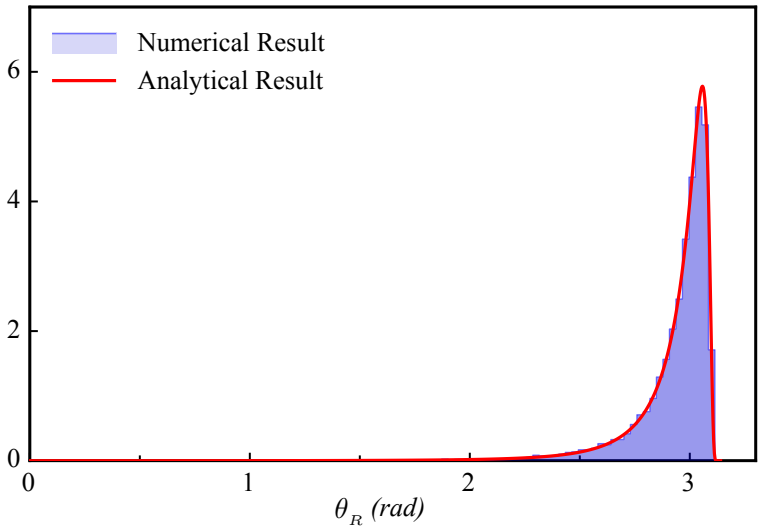

FIGURE C.5: Numerical and analytical representation of $f_{\Theta_R|r,y,\delta}(\theta_R)$ for $r = 1$, $y = -1$, $\delta = 1.5$, $N = 10$ and $\sigma = 1$.

Note that $f_{\mathrm{L}|y,\delta}(\ell)$ and $f_{\mathrm{R}|y,\delta}(r)$ are determined using Eqs. (C.9) and (C.10) respectively. Considering the fact that Θ_L and Θ_R for given values of ℓ, r, y and δ are independent random variables, their joint probability distribution function can thus be written as

$$f_{\Theta_L\Theta_R|\ell,r,y,\delta}\left(\theta_L,\theta_R\right) = f_{\Theta_L|\ell,y,\delta}\left(\theta_L\right).f_{\Theta_R|r,y,\delta}\left(\theta_R\right). \tag{C.25}$$

The analytical and numerical representation of the joint probability distribution function of Θ_L and Θ_R for $\ell = 2$, $r = 3$, $\delta = 1$, $y = 0$, $N = 10$ and $\sigma = 1$ are displayed in Fig. (C.6).

According to Eq. (2.10), the hinge angle, Θ, is the sum of two random variables Θ_L and Θ_R. Thus, its cumulative distribution function can be determined by integrating the joint probability density function of Θ_L and Θ_R given ℓ, r, y and δ in the plane $\theta_L\theta_R$ over a region defined by $\Theta_L + \Theta_R \leq \theta$. Hence

$$F_{\Theta|\ell,r,y,\delta}\left(\theta\right) = \int_{-\infty}^{+\infty}\int_{-\infty}^{\theta-\theta_R} f_{\Theta_L\Theta_R|\ell,r,y,\delta}\left(\theta_L,\theta_R\right)\, d\theta_L\, d\theta_R. \tag{C.26}$$

Substituting Eq. (C.25) in Eq. (C.26) provides

$$F_{\Theta|\ell,r,y,\delta}\left(\theta\right) = \int_{-\infty}^{+\infty}\int_{-\infty}^{\theta-\theta_R} f_{\Theta_L|\ell,y,\delta}\left(\theta_L\right)\, f_{\Theta_R|r,y,\delta}\left(\theta_R\right)\, d\theta_L\, d\theta_R. \tag{C.27}$$

Then, the probability density function of Θ given ℓ, r, y and δ is determined by differentiating its cumulative distribution function, $F_{\Theta|\ell,r,y,\delta}\left(\theta\right)$, with respect to θ. As

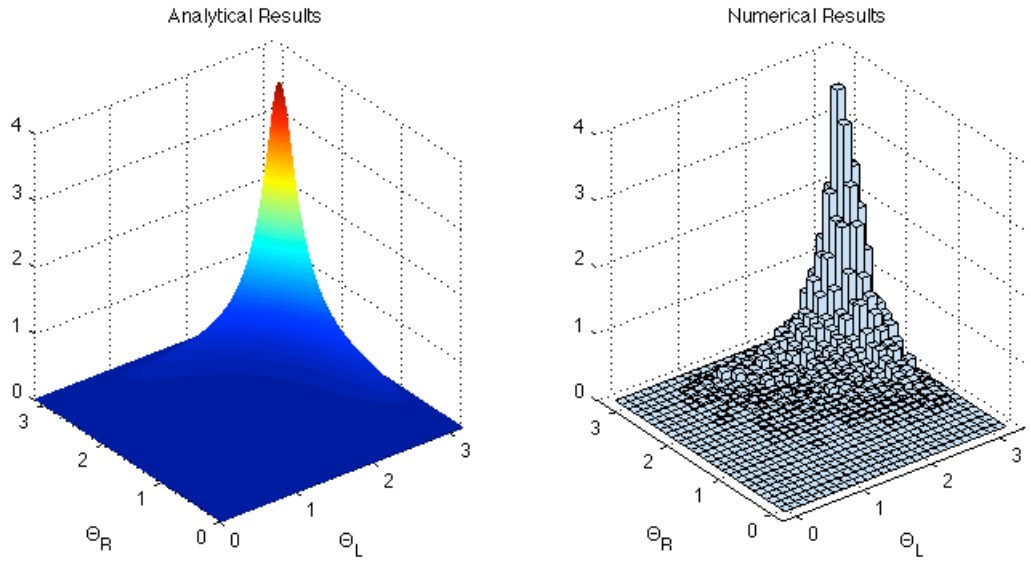

FIGURE C.6: Numerical and analytical representation of $f_{\Theta_L\Theta_R|\ell,r,y,\delta}(\theta_L,\theta_R)$ for $\ell=2$, $r=3$, $y=0$, $\delta=1$, $N=10$ and $\sigma=1$.

a result

$$f_{\Theta|\ell,r,y,\delta}(\theta)=\frac{\partial}{\partial\theta}F_{\Theta|\ell,r,y,\delta}(\theta)=\int_{-\infty}^{+\infty}f_{\Theta_L|\ell,y,\delta}(\theta_L)\ f_{\Theta_R|r,y,\delta}(\theta-\theta_L)\ d\theta_L. \qquad \text{(C.28)}$$

Fig. (C.7) shows the analytical and numerical representation of the probability density function of Θ for given values of $\ell=8$, $r=10$, $y=2$, $\delta=1$, $N=10$ and $\sigma=1$.

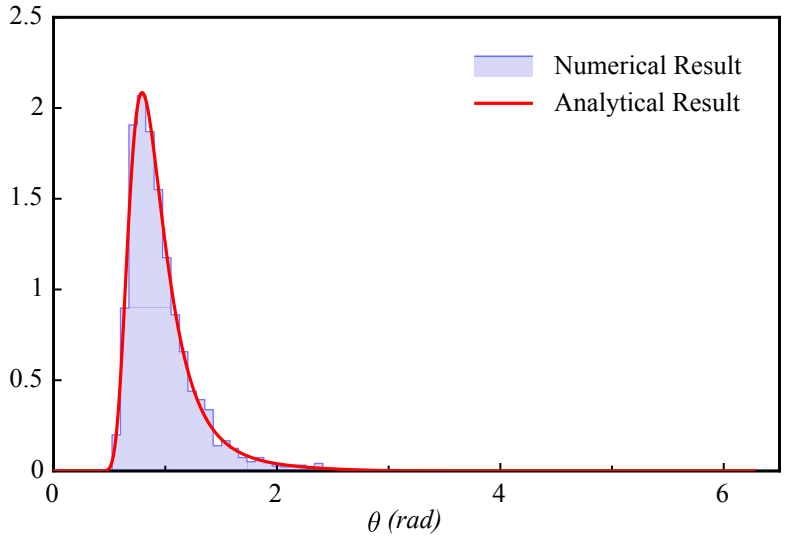

FIGURE C.7: Numerical and analytical representation of $f_{\Theta|\ell,r,y,\delta}(\theta)$ for $\ell=8$, $r=10$, $y=2$, $\delta=1$, $N=10$ and $\sigma=1$.

For different values of ℓ, r, y and δ, $f_{\Theta|\ell,r,y,\delta}(\theta)$ forms a four dimensional matrix in

which, two of the the four dimensions take only discrete values (ℓ and r). The function $f_{\Theta|\frac{\ell r}{\ell+r},y,\delta}(\theta)$ is then determined by reducing one of the dimensions of the aforementioned matrix by adding up the probability of the pairs of ℓ and r characterised by the same $(\frac{\ell r}{\ell+r})$. As a result, the following expression is obtained

$$f_{\Theta|x_2,y,\delta}(\theta) = f_{\Theta|\frac{\ell r}{\ell+r},y,\delta}(\theta)\,. \tag{C.29}$$

Fig. (C.8) shows the analytical and numerical representation of the probability density function of Θ for given values of $x_2 = 4.444$ ($\ell = 8$, $r = 10$ and $\ell = 10$, $r = 8$), $y = 2$, $\delta = 0$, $N = 10$ and $\sigma = 1$.

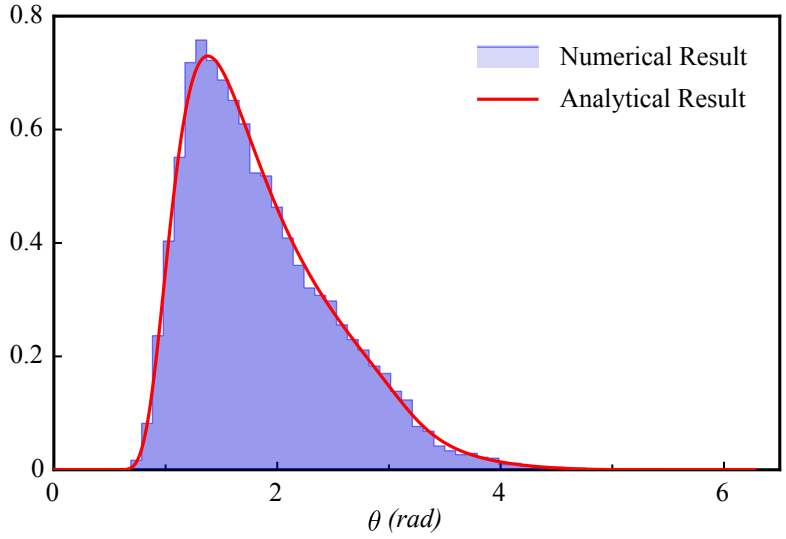

FIGURE C.8: Numerical and analytical representation of $f_{\Theta|x_2,y,\delta}(\theta_R)$ for $x_2 = 4.444$, $y = 2$, $\delta = 0$, $N = 10$ and $\sigma = 1$.

As it was shown earlier in Eq. (2.34), the "closing moment", X_1, is a function of the hinge angle, Θ. Therefore, its probability density function given x_2 and δ can be expressed by

$$f_{X_1|x_2,y,\delta}(x_1) = \frac{1}{\kappa} f_{\Theta|x_2,y,\delta}\left(\frac{x_1}{\kappa}\right). \tag{C.30}$$

Fig. (C.9) shows the analytical and numerical representation of the probability density function of X_1 for given values of $y = 2$ and $\delta = 0$, $N = 10$, $\sigma = 1$ and all the possible values of x_2.

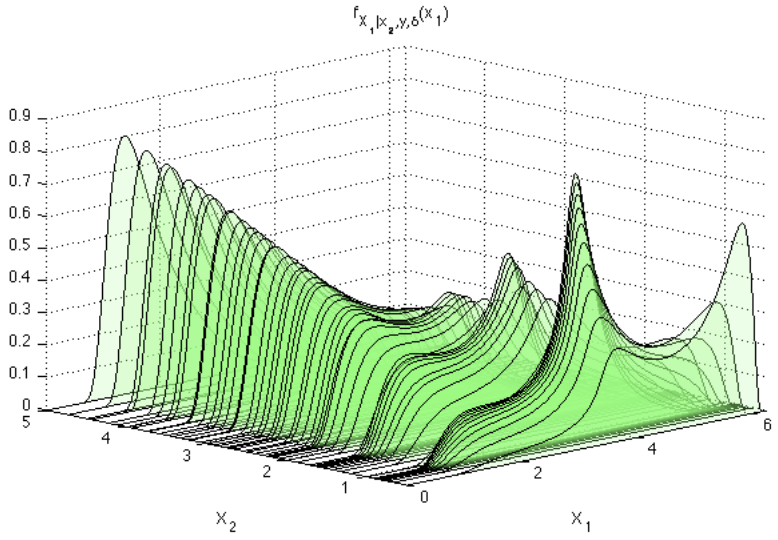

FIGURE C.9: Numerical and analytical representation of $f_{X_1|x_2,y,\delta}(x_1)$ for $y = 2$, $\delta = 0$, $N = 10$, $\sigma = 1$ and all the possible outcomes of x_2.

The joint probability distribution of the "opening " and "closing " moments is then determined using the Bayesian rule as follows

$$f_{X_1X_2|y,\delta}(x_1, x_2) = f_{X_1|x_2,y,\delta}(x_1) \, . f_{X_2|y,\delta}(x_2) \, . \tag{C.31}$$

Appendix D

Probability Density Function of $\delta^{\diamond}$

Random variables X_p and X_n are introduced as the states of the random process $\mathbf{x}(\delta)$ just before (at the fixed distance δ and given y) and just after (at the fixed distance $\delta + d\delta$ and given y) the zero passage occurs. As the random process $\mathbf{x}(\delta)$ is strictly decreasing, thus, the probability density function of the first passage distance, $\delta^{\diamond}$, can be written as the double integral of the joint probability distribution of X_p and X_n over the region in $x_p x_n$ plane where x_p is positive and x_n is negative. As a result

$$\begin{aligned} f_{\Delta^{\diamond}|y}(\delta^{\diamond})\, d\delta^{\diamond} &= \Pr\left(X_p > 0 \,\&\, X_n < 0\right) \\ &= \int_{-\infty}^{0} \left(\int_{0}^{+\infty} f_{X_p X_n}(x_p, x_n)\, dx_p \right) dx_n, \end{aligned} \tag{D.1}$$

where $f_{X_p X_n}(x_p, x_n)$ is the joint probability distribution function of X_p and X_n. Note that $\delta < \delta^{\diamond} < \delta + d\delta$. The inner integral of Eq. (D.1) can be written as

$$\begin{aligned} \int_{0}^{+\infty} f_{X_p X_n}(x_p, x_n)\, dx_p &= \int_{-\infty}^{+\infty} f_{X_p X_n}(x_p, x_n)\, dx_p - \int_{-\infty}^{0} f_{X_p X_n}(x_p, x_n)\, dx_p \\ &= f_{X_n}(x_n) - \int_{-\infty}^{0} f_{X_p X_n}(x_p, x_n)\, dx_p, \end{aligned} \tag{D.2}$$

which is obtained by changing the integration domain of the joint probability distribution function. Note that the first integral on the right hand side of Eq. (D.2) denotes the marginal density function of X_n. Substituting Eq. (D.2) in Eq. (D.1) provides

$$\begin{aligned} f_{\Delta^{\diamond}|y}(\delta^{\diamond})\, d\delta^{\diamond} &= \int_{-\infty}^{0} \left(f_{X_n}(x_n) - \int_{-\infty}^{0} f_{X_p X_n}(x_p, x_n)\, dx_p \right) dx_n \\ &= \int_{-\infty}^{0} f_{X_n}(x_n)\, dx_n - \int_{-\infty}^{0} \left(\int_{-\infty}^{0} f_{X_p X_n}(x_p, x_n)\, dx_n \right) dx_p. \end{aligned} \tag{D.3}$$

The inner integral on the right hand side of Eq. (D.3) can again be replaced by changing the integration domain as

$$\begin{aligned}\int_{-\infty}^{0} f_{X_pX_n}(x_p, x_n)\, dx_n &= \int_{-\infty}^{+\infty} f_{X_pX_n}(x_p, x_n)\, dx_n - \int_{0}^{+\infty} f_{X_pX_n}(x_p, x_n)\, dx_n \\ &= f_{X_p}(x_p) - \int_{-\infty}^{0} f_{X_pX_n}(x_p, x_n)\, dx_n, \end{aligned} \tag{D.4}$$

where alike Eq. (D.2), the first integral on the right hand side of Eq. (D.4) indicates the marginal density function of X_p. Substituting Eq. (D.4) in Eq. (D.3) results in

$$\begin{aligned} f_{\Delta^\diamond|y}(\delta^\diamond)\, d\delta^\diamond &= \int_{-\infty}^{0} f_{X_n}(x_n)\, dx_n - \int_{-\infty}^{0} f_{X_p}(x_p)\, dx_p + \\ &\quad \int_{0}^{+\infty} \left(\int_{-\infty}^{0} f_{X_pX_n}(x_p, x_n)\, dx_p \right) dx_n. \end{aligned} \tag{D.5}$$

As any realisation of the random process $\mathbf{x}(\delta)$ is strictly decreasing, thus, the probability of X_p being negative while X_n is positive for any $n > p$ is zero. Hence

$$\int_{0}^{+\infty} \left(\int_{-\infty}^{0} f_{X_pX_n}(x_p, x_n)\, dx_p \right) dx_n = \Pr\left(X_p < 0 \,\&\, X_n > 0\right) = 0. \tag{D.6}$$

Therefore, the probability density function of $\delta^\diamond$ can be obtained by simplifying Eq. (D.5) as

$$f_{\Delta^\diamond|y}(\delta^\diamond) = \frac{1}{d\delta^\diamond} \int_{-\infty}^{0} \left(f_{X_n}(x_n)\, dx_n - f_{X_p}(x_p)\, dx_p \right). \tag{D.7}$$

Note that the integration in Eq. (D.7) can be replaced by the cumulative distribution function of X_p and X_n at $x = 0$ as follows

$$F_{X_p}(0) = \int_{-\infty}^{0} f_{X_p}(x_p)\, dx_p, \qquad F_{X_n}(0) = \int_{-\infty}^{0} f_{X_n}(x_n)\, dx_n. \tag{D.8}$$

Therefore, another representation of the probability density function of $\delta^\diamond$ is given by

$$f_{\Delta^\diamond|y}(\delta^\diamond) = \frac{1}{d\delta^\diamond} \left(F_{X_n}(0) - F_{X_p}(0) \right). \tag{D.9}$$

As it was mentioned earlier, the random variables X_p and X_n are the states of the stochastic process $\mathbf{x}(\delta)$ for a given y and at fixed distances δ and $\delta + d\delta$, respectively. Thus, the final representation of the probability density function of $\delta^\diamond$ conditioned on y is given by

$$\begin{aligned} f_{\Delta^\diamond|y}(\delta^\diamond) &= \frac{1}{d\delta^\diamond} \int_{-\infty}^{0} \left(f_{X|y,\delta+d\delta}(x) - f_{X|y,\delta}(x) \right) dx \\ &= \frac{1}{d\delta^\diamond} \left(F_{X|y,\delta+d\delta}(0) - F_{X|y,\delta}(0) \right), \end{aligned} \tag{D.10}$$

where $f_{X|y,\delta}(x)$ and $f_{X|y,\delta+d\delta}(x)$ are obtained using Eq. (2.39).

Bibliography

[1] R. Leine and D. Campen, "Stick-slip whirl interaction in drillstring dynamics," in *IUTAM Symposium on Chaotic Dynamics and Control of Systems and Processes in Mechanics*, vol. 112. Rome, Italy: Springer Netherlands, June 2005, pp. 287–296.

[2] S. F. Wolf, M. Zacksenhouse, and A. Arian, "Field measurements of downhole drillstring vibrations," in *SPE Annual Technical Conference and Exhibition*, no. SPE 14330. Las Vegas, Nevada, U.S.A.: Society of Petroleum Engineers, September 1985, pp. 1–12.

[3] T. V. Aarrestad, H. A. Tonnesen, and A. Kyllingstad, "Drillstring vibrations: Comparison between theory and experiments on a full-scale research drilling rig," in *IADC/SPE Drilling Conference*, no. IADC/SPE 14760. Dallas, Texas, U.S.A.: Society of Petroleum Engineers, February 1986, pp. 311–321.

[4] T. V. Aarrestad and A. Kyllingstad, "An experimental and theoretical study of a coupling mechanism between longitudinal and torsional drillstring vibrations at the bit," *SPE Drilling Engineering*, vol. 3, pp. 12–18, 1988.

[5] J. D. Jansen, "Non-linear rotor dynamics as applied to oilwell drillstring vibrations," *Journal of Sound and Vibration*, vol. 147, pp. 115–135, 1991.

[6] J. F. Brett, "The genesis of torsional drillstring vibrations," *SPE Drilling Engineering*, vol. 7, pp. 168–174, 1992.

[7] W. D. Aldred and M. C. Sheppard, "Drillstring vibrations: A new generation mechanism and control strategies," in *67th Annual Technical Conference and Exhibition of the Society of Petroleum Engineers*, no. SPE 24582. Washington, D.C., U.S.A.: Society of Petroleum Engineers, October 1992, pp. 353–363.

[8] S. L. Chen and M. Geradin, "Dynamic modelling of transverse drillstring vibrations due to bit/formation interaction," University of Liege, Tech. Rep., August 1993.

[9] G. H. M. van der Heijden, "Bifurcation and chaos in drillstring dynamics," *Chaos, Solitons and Fractals*, vol. 3, pp. 219–247, 1993.

[10] J. D. Jansen and L. van den Steen, "Active damping of self-excited torsional vibrations in oil-well drillstrings," *Journal of Sound and Vibration*, vol. 179, pp. 647–668, 1995.

[11] J. D. Jansen, L. van den Steen, and E. Zachariasen, "Active damping of torsional drillstring vibrations with a hydraulic top drive," *SPE Drilling and Completion*, vol. 10, pp. 250–254, 1995.

[12] R. I. Leine, D. H. van Campen, A. de Kraker, and L. van den Steen, "Stick-slip vibrations induced by alternate friction models," *Nonlinear Dynamics*, vol. 16, pp. 41–54, 1998.

[13] R. I. Leine, D. H. van Campen, and W. J. G. Keultjes, "Stick-slip whirl interaction in drillstring dynamics," *ASME Journal of Vibration and Acoustics*, vol. 124, pp. 209–220, 2002.

[14] P. C. Kriesels, W. J. G. Keultjes, P. Dumont, I. Huneidi, O. O. Owoeye, and R. A. Hartmann, "Cost savings through an integrated approach to drillstring vibration control," in *SPE/IADC Middle East Drilling Technology Conference*, no. SPE/IADC 57555. Abu Dhabi, United Arab Emirates: Society of Petroleum Engineers, November 1999, pp. 1–12.

[15] H. Santos, J. C. R. Placido, and C. Wolter, "Consequences and relevance of drillstring vibration on wellbore stability," in *SPE/IADC Drilling Conference*, no. SPE/IADC 52820. Amsterdam, Netherlands: Society of Petroleum Engineers, March 1999, pp. 1–7.

[16] P. D. Spanos, A. M. Chevallier, and N. P. Politis, "Nonlinear stochastic drill-string vibrations," *ASME Journal of Vibration and Acoustics*, vol. 124, pp. 512–518, 2002.

[17] M. A. Elsayed and D. W. Raymond, "Analysis of coupling between axial and torsional vibration in a compliant model of a drillstring equipped with a PDC bit,"

in *ASME Engineering Technology Conference on Energy*, no. ETCE2002/STRUC-29002, Houston, Texas, U.S.A., February 2002, pp. 1–8.

[18] A. S. Bakenov, T. Gabler, E. Detournay, and C. Germay, "Enhanced drilling performance through controlled drillstring vibrations," in *AADE National Technology Conference "Practical Solutions for Drilling Challenges"*, no. AADE-03-NTCE-21, Houston, Texas, U.S.A., April 2003, pp. 1–8.

[19] Y. A. Khulief and H. Al-Naser, "Finite element dynamic analysis of drillstrings," *Finite Elements in Analysis and Design*, vol. 41, pp. 1270–1288, 2005.

[20] Y. A. Khulief, F. A. Al-Sulaiman, and S. Bashmal, "Vibration analysis of drillstrings with self-excited stick-slip oscillations," *Journal of Sound and Vibration*, vol. 299, pp. 540–558, 2007.

[21] O. J.-M. Hoffmann, "Drilling induced vibration apparatus," Ph. D. Thesis, University of Minnesota, Minneapolis, Minnesota, U.S.A., June 2006.

[22] E. W. Robnett, J. A. Hood, G. Heisig, and J. D. Macpherson, "Analysis of the stick-slip phenomenon using downhole drillstring rotation data," in *SPE/IADC Drilling Conference*, no. SPE/IADC 52821. Amsterdam, Netherlands: Society of Petroleum Engineers, March 1999, pp. 1–12.

[23] T. Richard, C. Germay, and E. Detournay, "A simplified model to explore the root cause of stick-slip vibrations in drilling systems with drag bits," Tech. Rep., November 2006.

[24] S. L. Chen and M. Geradin, "An improved transfer-matrix technique as applied to BHA lateral vibration analysis," *Journal of Sound and Vibration*, vol. 185, pp. 93–106, 1995.

[25] S. L. Chen, K. Blackwood, and E. Lamine, "Field investigation of the effects of stick-slip, lateral, and whirl vibrations on roller cone bit performance," in *SPE Annual Technical Conference and Exhibition*, no. SPE 56439. Houston, Texas, U.S.A.: Society of Petroleum Engineers, October 1999, pp. 1–10.

[26] ——, "Field investigation of the effects of stick-slip, lateral, and whirl vibrations on roller-cone bit performance," *SPE Drilling and Completion*, vol. 17, pp. 15–20, 2002.

[27] J. F. Brett, T. M. Warren, and S. M. Behr, "Bit whirl - a new theory of PDC bit failure," in *64th Annual Technical Conference and Exhibition of the Society of Petroleum Engineers*, no. SPE 19571. San Antonio, Texas, U.S.A.: Society of Petroleum Engineers, 1989, pp. 521–536.

[28] S. X. Wu, L. Paez, U. Partin, and M. Agnihotri, "Decoupling stick-slip and whirl to achieve breakthrough in drilling performance," in *IADC/SPE Drillng Conference and Exhibition*, no. IADC/SPE 128767. New Orleans, Louisiana, U.S.A.: Society of Petroleum Engineers, February 2010, pp. 1–13.

[29] D. R. H. Stroud, L. A. Lines, and D. J. Minett-Smith, "Analytical and experimental backward whirl simulations for rotary steerable bottom hole assemblies," in *SPE/IADC Drilling Conference and Exhibition*, no. SPE/IADC 140011. Amsterdam, Netherlands: Society of Petroleum Engineers, March 2011, pp. 1–19.

[30] T. Richard, C. Germay, and E. Detournay, "Self-excited stick-slip oscillations of drill bits," *Comptes Rendus Mecanique*, vol. 332, pp. 619–626, 2004.

[31] S. Desmette, J. Will, C. Coudyzer, T. Richard, and P. Le, "Isubs: A new generation of autonomous instrumented downhole tool," in *SPE/IADC Drilling Conference*, no. SPE/IADC 92424. Amsterdam, Netherlands: Society of Petroleum Engineers, February 2005, pp. 1–7.

[32] M. Neubert, G. Heisig, I. Forstner, and F. Mounzer, "Verification of an advanced analysis model with downhole bending moment measurements," in *Asia Pacific Oil and Gas Conference and Exhibition*, no. SPE 93864. Jakarta, Indonesia: Society of Petroleum Engineers, April 2005, pp. 1–10.

[33] L. W. Ledgerwood III, O. J. Hoffmann, J. R. Jain, C. E. Hakam, C. Herbig, and R. W. Spencer, "Downhole vibration measurement, monitoring and modeling reveal stick-slip as a primary cause of PDC bit damage in today's applications," in *SPE Annual Technical Conference and Exhibition*, no. SPE 134488. Florence, Italy: Society of Petroleum Engineers, September 2010, pp. 1–10.

[34] A. D. Craig, R. Goodship, and D. R. Shearer, "High frequency downhole dynamic measurements provide greater understanding of drilling vibration in performance motor assemblies," in *IADC/SPE Drillng Conference and Exhibition*,

no. IADC/SPE 128211. New Orleans, Louisiana, U.S.A.: Society of Petroleum Engineers, February 2010, pp. 1–10.

[35] P. R. Belanger, P. Dobrovolny, A. Helmy, and X. Zhang, "Estimation of angular velocity and acceleration from shaft-encoder measurements," *International Journal of Robotics Research*, vol. 17, pp. 1225–1233, 1998.

[36] R. Negenborn, "Robot localization and Kalman filters on finding your position in a noisy world," Master of Science Thesis, Utrecht University, Utrecht, Netherlands, September 2003.

[37] J. D. Han, Y. Q. He, and W. L. Xu, "Angular acceleration estimation and feedback control: An experimental investigation," *Mechatronics*, vol. 17, pp. 524–532, 2007.

[38] P. Cardou and J. Angeles, "Estimating the angular velocity of a rigid body moving in the plane from tangential and centripetal acceleration measurements," *Multibody System Dynamics*, vol. 19, pp. 383–406, 2008.

[39] ——, "Linear estimation of the rigid-body acceleration field from point-acceleration measurements," *ASME Journal of Dynamic Systems Measurement and Control*, vol. 131, 2009.

[40] A. K. Booer, "Determination of drill bit rate of penetration from surface measurements," Patent, September, 1996.

[41] M. ElGizawy, A. Noureldin, J. Georgy, U. Iqbal, and N. El-Sheimy, "Wellbore surveying while drilling based on Kalman filtering," *American Journal of Engineering and Applied Sciences*, vol. 3, pp. 240–259, 2010.

[42] R. C. Hibbeler, *Engineering Mechanics: Dynamics*, ser. Mastering Engineering Series. Prentice Hall, 2009.

[43] D. Simon, *Optimal State Estimation: Kalman, H Infinity and Nonlinear Approaches*. John Wiley and Sons, 2006.

[44] B. P. Gibbs, *Advanced Kalman Filtering, Least-Squares and Modeling: A Practical Handbook*. John Wiley and Sons, 2011.

[45] M. Grewal, L. Weill, L. Weill, and A. Andrews, *Global positioning systems, inertial navigation, and integration*. Wiley-Interscience, 2007.

[46] T. Richard, C. Germay, and E. Detournay, "A simplified model to explore the root cause of stick-slip vibrations in drilling systems with drag bits," *Journal of Sound and Vibration*, vol. 305, pp. 432–456, 2007.

[47] "Applications of Magnetic Position Sensors, Honeywell Sensor Products, Solid State Electronics Center www.magneticsensors.com," Application Note.

[48] R. A. Estes, R. Cruz, D. Hope, and N. Foekema, "Magnetometers for measurement-while-drilling applications," Patent, 2007.

[49] M. Feldman, *Hilbert Transform Applications in Mechanical Vibration.* John Wiley and Sons, 2011.

[50] "ADXL150/ADXL250 Datasheet: Analog devices One Technology Way, P.O. Box 9106, Norwood, MA 02062-9106, U.S.A. http://www.analog.com."

[51] S. Chen, "Linear and nonlinear dynamics of drillstrings," Ph. D. Thesis, University of Liege, Liege, Belgium, 1994.

[52] M. J. Fear, "How to improve rate of penetration in field operations," in *SPE/IADC Drilling Conference*, no. IADC/SPE 35107. New Orleans, Louisiana, U.S.A.: Society of Petroleum Engineers, March 1996, pp. 1–17.

[53] F. E. Dupriest and W. L. Koederitz, "Maximizing drill rates with real-time surveillance of mechanical specific energy," in *SPE/IADC Drilling Conference*, no. SPE/IADC 92194. Amsterdam, Netherlands: Society of Petroleum Engineers, February 2005, pp. 1–10.

[54] F. E. Dupriest, "Comprehensive drill-rate management process to maximize rate of penetration," in *SPE Annual Technical Conference and Exhibition*, no. SPE 102210. San Antonio, Texas, U.S.A.: Society of Petroleum Engineers, September 2006, pp. 1–9.

[55] E. Cayeux, E. W. Dvergsnes, and F. Iversen, "Real-time optimization of the drilling process - challenges in industrialization," in *SPE/IADC Drilling Conference and Exhibition*, no. SPE/IADC 119650. Amsterdam, Netherlands: Society of Petroleum Engineers, March 2009, pp. 1–12.

[56] T. Eren and M. E. Ozbayoglu, "Real time optimization of drilling parameters during drilling operations," in *SPE Oil and Gas India Conference and Exhibition*, no. SPE 129126, Mumbai, India, January 2010, pp. 1–14.

[57] D. Barry and J. A. Hartigan, "A Bayesian analysis for change point problems," *Journal of the American Statistical Association*, vol. 88, pp. 309–319, 1993.

[58] P. Fearnhead and Z. Liu, "Efficient online inference for multiple changepoint problems," in *Nonlinear Statistical Signal Processing Workshop*, Cambridge, UK, September 2006, pp. 5–8.

[59] P. Fearnhead, "Exact and efficient Bayesian inference for multiple changepoint problems," *Statistics and Computing*, vol. 16, pp. 203–213, 2006.

[60] E. K. Szusz and A. R. Willms, "A linear time algorithm for near minimax continuous piecewise linear representations of discrete data," *SIAM Journal On Scientific Computing*, vol. 32, pp. 2584–2602, 2010.

[61] M. Lavielle and E. Lebarbier, "An application of MCMC methods for the multiple change-points problem," *Signal Processing*, vol. 81, pp. 39–53, 2001.

[62] S. Mahmoodi and B. S. Sharif, "Noise reduction, smoothing and time interval segmentation of noisy signals using an energy optimisation method," *IEE Proceedings-Vision Image and Signal Processing*, vol. 153, pp. 101–108, 2006.

[63] E. J. Keogh and M. J. Pazzani, "A simple dimensionality reduction technique for fast similarity search in large time series databases," *Knowledge Discovery and Data Mining, Proceedings*, vol. 1805, pp. 122–133, 2000.

[64] E. Keogh, H. Hochheiser, and B. Shneiderman, "An augmented visual query mechanism for finding patterns in time series data," *Flexible Query Answering Systems, Proceedings*, vol. 2522, pp. 240–250, 2002.

[65] E. Keogh, S. Chu, D. Hart, and M. Pazzani, "Segmenting time series: A survey and novel approach," in *Data Mining in Time Series Databases*. World Scientific, 2003, ch. 1, pp. 1–21.

[66] ——, "An online algorithm for segmenting time series," in *Proceedings IEEE International Conference on Data Mining*, San Jose, CA, U.S.A., November-December 2001, pp. 289–296.

[67] E. Keogh, K. Chakrabarti, M. Pazzani, and S. Mehrotra, "Dimensionality reduction for fast similarity search in large time series databases," *Knowledge and Information Systems*, vol. 3, pp. 263–286, 2001.

[68] E. Keogh, K. Chakrabarti, S. Mehrotra, and M. Pazzani, "Locally adaptive dimensionality reduction for indexing large time series databases," *Sigmod Record*, vol. 30, pp. 151–162, 2001.

[69] X. Liu, Z. Lin, and H. Wang, "Novel online methods for time series segmentation," *IEEE Transactions On Knowledge and Data Engineering*, vol. 20, pp. 1616–1626, 2008.

[70] A. Kaplan, J. Roschke, B. Darkhovsky, and J. Fell, "Macrostructural eeg characterization based on nonparametric change point segmentation: application to sleep analysis," *Journal of Neuroscience Methods*, vol. 106, pp. 81–90, 2001.

[71] D. M. Hawkins, "Fitting multiple change-point models to data," *Computational Statistics & Data Analysis*, vol. 37, pp. 323–341, 2001.

[72] A. Kehagias, E. Nidelkou, and V. Petridis, "A dynamic programming segmentation procedure for hydrological and environmental time series," *Stochastic Environmental Research and Risk Assessment*, vol. 20, pp. 77–94, 2006.

[73] D. H. Douglas and T. K. Peucker, "Algorithms for the reduction of the number of points required to represent a digitized line or its caricature," *Cartographica: The International Journal for Geographic Information and Geovisualization*, vol. 10, pp. 112–122, 1973.

[74] U. Appel and A. V. Brandt, "Adaptive sequential segmentation of piecewise stationary time series," *Information Sciences*, vol. 29, pp. 27–56, 1983.

[75] ——, "A comparative study of three sequential time series segmentation algorithms," *Signal Processing*, vol. 6, pp. 45–60, 1984.

[76] M. Basseville and I. V. Nikiforov, *Detection of abrupt changes: theory and application*, ser. Prentice Hall information and system sciences series. Prentice Hall, 1993.

[77] D. Siegmund and E. S. Venkatraman, "Using the generalized likelihood ratio statistic for sequential detection of a change-point," *Annals of Statistics*, vol. 23, pp. 255–271, 1995.

[78] F. Gustafsson, "The marginalized likelihood ratio test for detecting abrupt changes," *IEEE Transactions On Automatic Control*, vol. 41, pp. 66–78, 1996.

[79] C. S. J. Chu, "Time series segmentation: A sliding window approach," *Information Sciences*, vol. 85, pp. 147–173, 1995.

[80] D. Lemire, "A better alternative to piecewise linear time series segmentation," in *SIAM Data Mining 2007*, 2007.

[81] E. Fuchs, T. Gruber, J. Nitschke, and B. Sick, "Online segmentation of time series based on polynomial least-squares approximations," *IEEE Transactions On Pattern Analysis and Machine Intelligence*, vol. 32, pp. 2232–2245, 2010.

[82] F. K. P. Chan, A. W. C. Fu, and C. Yu, "Haar wavelets for efficient similarity search of time-series: With and without time warping," *IEEE Transactions On Knowledge and Data Engineering*, vol. 15, pp. 686–705, 2003.

[83] V. S. Tseng, C.-H. Chen, P.-C. Huang, and T.-P. Hong, "Cluster-based genetic segmentation of time series with DWT," *Pattern Recognition Letters*, vol. 30, pp. 1190–1197, 2009.

[84] S. L. Sclove, "Time-series segmentation: A model and a method," *Information Sciences*, vol. 29, pp. 7–25, 1983.

[85] E. Punskaya, C. Andrieu, A. Doucet, and W. J. Fitzgerald, "Bayesian curve fitting using MCMC with applications to signal segmentation," *IEEE Transactions On Signal Processing*, vol. 50, pp. 747–758, 2002.

[86] P. Fearnhead, "Exact Bayesian curve fitting and signal segmentation," *IEEE Transactions On Signal Processing*, vol. 53, pp. 2160–2166, 2005.

[87] V. Denoel, T. Richard, and C. Tilman, "Segmentation of drilling data," Epslog, Liege, Belgium, Confidential Report, July 2009.

[88] H. Shatkay and S. B. Zdonik, "Approximate queries and representations for large data sequences," in *Proceedings of the Twelfth International Conference on Data Engineering*, New Orleans, Louisiana, U.S.A., February-March 1996, pp. 536–545.

[89] O. A. Bauchau and J. I. Craig, *Structural analysis: with applications to aerospace structures*, ser. Solid mechanics and its applications. Springer, 2009.

[90] A. Papoulis and S. U. Pillai, *Probability, random variables, and stochastic processes*, ser. McGraw-Hill electrical and electronic engineering series. McGraw-Hill, 2002.

[91] H. A. David and H. N. Nagaraja, *Order statistics*, ser. Probability and mathematical statistics. John Wiley, 2003.

[92] R. L. Stratonovich, *Topics in the Theory of Random Noise*, ser. Mathematics and Its Applications Series. Gordon and Breach, 1963, vol. 1.

[93] S. Redner, *A guide to first-passage processes.* Cambridge University Press, 2001.

[94] R. L. Stratonovich, *Topics in the Theory of Random Noise*, ser. Mathematics and its applications. Gordon and Breach, 1967, vol. 2.

[95] P. Hubert, "The segmentation procedure as a tool for discrete modeling of hydrometeorological regimes," *Stochastic Environmental Research and Risk Assessment*, vol. 14, pp. 297–304, 2000.

[96] E. Detournay and P. Defourny, "A phenomenological model for the drilling action of drag bits," *International Journal of Rock Mechanics and Mining Sciences and Geomechanics Abstracts*, vol. 29, pp. 13–23, 1992.

[97] Y. Bar-Shalom, X. R. Li, and T. Kirubarajan, *Estimation with applications to tracking and navigation*, ser. A Wiley-Interscience publication. Wiley, 2001.

[98] J. Galambos, *The asymptotic theory of extreme order statistics.* R. E. Krieger Pub. Co., 1987.

Every reasonable effort has been made to acknowledge the owners of copyright material. I would be pleased to hear from any copyright owner who has been omitted or incorrectly acknowledged.